

Experimental Study of Droplet Vaporization and Combustion of Diesel,  
Biodiesel and their blends in a Turbulent Environment at Elevated Pressure  
and Temperature Conditions

By

Stephen L. Toth

A Thesis submitted to the Faculty of Graduate Studies of

The University of Manitoba

in partial fulfillment of the requirements of the degree of

MASTER OF SCIENCE

Department of Mechanical Engineering

University of Manitoba

Winnipeg

Copyright © 2014 by Stephen L. Toth

## Abstract

Droplet vaporization and combustion of biodiesel, diesel and their blends was examined experimentally in a turbulent flow at elevated ambient temperature and pressure conditions. A high pressure vessel capable of generating high levels of turbulence was employed in this study. The linear relationship between turbulence intensity and fans rotational speed, which was developed at room temperature, was found to be unaffected by the gas ambient temperature.

Droplet vaporization experiments were performed by varying turbulence intensity (i.e., the fans rotational speed) from 0 up to 3.1 m/s, ambient temperature and pressure up to 473 K and 16 bar, respectively. The results revealed that diesel droplet vaporization did not follow the  $d^2$ -law under the aforementioned test conditions. However, biodiesel droplet vaporization obeyed the  $d^2$ -law. Droplet vaporization of the blends, i.e. B20 and B50, displayed a mixed behaviour of both parent fuels with the biodiesel behaviour predominating where biodiesel content slows down the droplet vaporization of the blends. Turbulence was found to reduce the droplet lifetime of all fuels (i.e., increases droplet vaporization rate), and its effect becomes more effective with increasing ambient pressure.

Droplet combustion experiments were performed by varying turbulence intensity from 0 up to 1.20 m/s, and ambient temperature up to 423K at ambient pressure of 1 atm. Diesel droplet combustion rate showed negligible change with turbulence intensity up to 0.40 m/s beyond which the burning rate decreased slightly with turbulence intensity. Similarly, biodiesel droplet combustion rate did not show an increase with the presence of a turbulent flow around the droplet. However, in contrast to diesel, biodiesel burning

rate remained nearly constant until the flame extinction limit. The combustion rate of B20 and B50 displayed a mixed behaviour of both parent fuels. Nevertheless, both blends showed that diesel had predominance over the burning rate. Finally, the droplet flame extinction of all fuel droplets occurred at turbulent velocity slightly greater than the laminar flame speed.

## **Acknowledgements**

I would like to thank my supervisor Dr. Birouk for giving me the opportunity and also providing guidance throughout the course of this thesis. To my colleagues in the lab, I would like to thank them for their technical assistance and helpful insights. I extend special thanks to S. Fabbro (former MSc student of Prof. Brouk) for providing consultation as well as technical assistance. From the technical staff, I would like to thank I. Penner, D. Rossong, D. Tataryn, J. Finken, K. Majury, M. Boskwick and A. Mckay for providing technical assistance and expertise whenever I sought their help. Also, special thanks to Drs. I. J. Ferguson, G. Thomas and D. K. Stoyko for providing their expertise with image and signal processing. I would like to acknowledge the financial support provided through research assistantships by Rolls-Royce Canada, CRIAQ and the Natural Sciences and Engineering Research Council (NSERC) of Canada. I would also like to thank the Department of Mechanical and Manufacturing Engineering of the University of Manitoba for providing me with financial support through a number of teaching assistantships. Last but not the least; I would like to thank my parents for providing encouragement as well as support in all facets of life during this program.

## Table of Contents

Abstract .....	ii
Acknowledgements .....	iv
Table of Contents .....	v
List of Tables .....	viii
List of Figures .....	ix
Chapter 1 - Introduction .....	1
Chapter 2 - Literature Review .....	3
2.1. Droplet Vaporization .....	3
2.1.1. Diesel Droplet Vaporization .....	3
2.1.1.1. Effect of Ambient Temperature .....	3
2.1.1.2. Effect of Ambient Pressure .....	9
2.1.1.3. Effect of Forced Convection Flow .....	12
2.1.2. Biodiesel Droplet Vaporization .....	13
2.1.2.1. Effect of Ambient Temperature .....	14
2.1.2.2. Effect of Ambient Pressure .....	17
2.1.2.3. Effect of Forced Convective Flow .....	19
2.1.3. Droplet Vaporization Biodiesel-Diesel Blends .....	22
2.1.3.1. Effect of Ambient Temperature .....	22
2.1.3.2. Effect of Ambient Pressure .....	24
2.1.3.3. Effect of Forced Convection .....	25
2.1.4. Conclusions .....	26
2.2. Droplet Combustion .....	29
2.2.1. Diesel Droplet Combustion .....	29
2.2.1.1. Effect of Ambient Temperature .....	29
2.2.1.2. Effect of Ambient Pressure .....	30
2.2.1.3. Effect of Forced Convection .....	31
2.2.2. Biodiesel Droplet Combustion .....	32
2.2.2.1. Effect of Ambient Temperature .....	32
2.2.2.2. Effect of Ambient Pressure .....	34
2.2.2.3. Effect of Forced Convection .....	34
2.2.3. Biodiesel-Diesel Blended Fuel Droplet Combustion .....	36
2.2.3.1. Effect of Ambient Temperature .....	36
2.2.3.2. Effect of Ambient Pressure .....	37

2.2.3.3. Effect of Forced Convection .....	37
2.2.4. Conclusions.....	38
Chapter 3 - Experimental Apparatus and Test Conditions .....	41
3.1. Experimental Apparatus.....	41
3.1.1. Introduction.....	41
3.1.2. Spherical Turbulence Chamber.....	41
3.1.3. Sealing Surfaces.....	43
3.1.4. Turbulence Generation and Fan Design .....	47
3.1.4.1. Fan Transmission Assembly .....	47
3.1.5. Heating System .....	48
3.1.5.1. Heating Plate Design.....	48
3.1.5.2. Heating Control System.....	51
3.1.5.3. Heating System Tests.....	53
3.1.5.4. Chamber Insulation.....	55
3.1.6. Droplet Suspension .....	57
3.1.7. Droplet Injection/Ignition System.....	58
3.1.7.1. Ignition Wire.....	58
3.1.7.2. Ignition Power Source.....	59
3.1.8. Image Capture Setup and Procedure.....	60
3.1.9. Image Processing .....	61
3.2. Test Conditions .....	61
Chapter 4 - Results and Discussion: Droplet Vaporization .....	63
4.1. Turbulence Characterization.....	63
4.2. Droplet Vaporization .....	64
4.2.1. Diesel Droplet .....	65
4.2.2. Biodiesel Droplet .....	72
4.2.3. Biodiesel-Diesel Blends.....	77
4.2.4. Comparison of Droplet Blends .....	84
4.2.5. Error Analysis .....	86
Chapter 5 - Results and Discussion: Droplet combustion .....	87
5.1. Diesel Droplet Combustion.....	87
5.2. Biodiesel Droplet Combustion.....	91
5.3. Biodiesel-Diesel Blends.....	94
5.4. Comparison of Droplet Blends .....	96

5.5. Discussion.....	97
Chapter 6 - . Conclusions and Recommendations .....	99
6.1. Conclusions.....	99
6.2. Recommendations for Future Work.....	100
References.....	104
Appendix A - Instrumentation .....	A-1
Appendix B - Chamber Seals.....	B-1
B.1. Introduction.....	B-1
B.2. Gasket Seals:.....	B-1
B.3. O-ring Seals: .....	B-2
B.4. Fan Shaft Seals.....	B-3
Appendix C - Fan Transmission Assembly .....	C-1
C.1. Bearings .....	C-1
C.2. Lubricants .....	C-1
C.3. Fan Transmission Assembly Drawings .....	C-3
Appendix D - Heating System .....	D-1
D.1. Introduction.....	D-1
D.2. Heating System Control Box .....	D-1
D.3. Heating Plates .....	D-2
D.4. Heating Plate Drawings .....	D-5
Appendix E - Ignition System.....	E-1
E.1. Ignition System Components.....	E-1
E.2. Ignition System Drawings.....	E-2
Appendix F - Matlab Code .....	F-1
F.1. Introduction.....	F-1
F.2. Matlab Code.....	F-2
Appendix G - Error Analysis .....	G-1
G.1. Diesel Example .....	G-3
G.2. Biodiesel Example .....	G-4

## List of Tables

<b>Table 2.1.</b> Summary of literature on droplet vaporization of diesel, biodiesel and their blends.....	28
<b>Table 2.2.</b> Summary of literature on droplet combustion of diesel, biodiesel and their blends.....	40
<b>Table 4.1.</b> Diesel droplet lifetime at 6 bar and 473 K.....	67
<b>Table 4.2.</b> Droplet lifetime % difference from weighted average of parent fuels.....	86
<b>Table B.1.</b> Gasket size specifications.....	B-1
<b>Table B.2.</b> Gasket material properties.....	B-1
<b>Table B.3.</b> O-ring size specifications.....	B-2
<b>Table B.4.</b> O-ring material properties.....	B-2
<b>Table B.5.</b> Material properties of poly-amide filled Teflon.....	B-3
<b>Table C.1.</b> Radial ball bearing specifications.....	C-1
<b>Table C.2.</b> Properties of Jet Lube AP-5.....	C-2
<b>Table D.1.</b> Components from Omega Engineering Inc. used for heating system control box.....	D-1
<b>Table D.2.</b> Properties of each heating element used for each respective heating plate.....	D-4

## List of Figures

<b>Figure 3.1.</b> Schematic diagram of the spherical chamber with flanges arrangement [48]. .....	43
<b>Figure 3.2.</b> Fan shaft seal with key features labeled [48]. .....	45
<b>Figure 3.3.</b> Seal deformation prior to installation. ....	46
<b>Figure 3.4.</b> Fan shaft seal before and after deformation. ....	46
<b>Figure 3.5.</b> Fan transmission shaft assembly [48]......	48
<b>Figure 3.6.</b> First heating plate. ....	50
<b>Figure 3.7.</b> Second heating plate. ....	50
<b>Figure 3.8.</b> Electrical box covering the heating element electrical terminals. ....	51
<b>Figure 3.9.</b> Heating system controller. ....	52
<b>Figure 3.10.</b> Chamber heating test with first plate and no insulation. ....	53
<b>Figure 3.11.</b> Chamber heating test with first plate and internal insulation. ....	54
<b>Figure 3.12.</b> Heat test with both heating plates and insulation of the inside of the chamber. ....	55
<b>Figure 3.13.</b> Insulation of the inner chamber wall. ....	56
<b>Figure 3.14.</b> Outside view of chamber with external insulation. ....	57
<b>Figure 3.15.</b> Wire element ignition head [48]......	58
<b>Figure 3.16.</b> Droplet injector with electrical wires for ignition system [48]. ....	60
<b>Figure 4.1.</b> Variation of turbulence intensity with rotational speed of fans.....	63
<b>Figure 4.2.</b> Variation of $u'/v'$ along the radial distance from the center of the vessel for various fans speed at different ambient pressures and temperatures. ....	64

<b>Figure 4.3.</b> Time history of the squared normalized diameter for different fans speeds at $T_{amb} = 473K$ and $P_{amb} = 6$ bar for diesel droplet comparing evaporation at (a) free convection and forced convection and (b) forced convection. ....	65
<b>Figure 4.4.</b> Diesel droplet lifetime as a function of ambient pressure for given fans speed at $T_{amb} = 473$ K. ....	67
<b>Figure 4.5.</b> Normalized diesel droplet lifetime for different ambient pressures at a given fans speed at $T_{amb} = 473$ K. ....	68
<b>Figure 4.6.</b> Diesel droplet lifetime as a function of fans rotational speed for different ambient pressures at $T_{amb} = 473$ K. ....	69
<b>Figure 4.7.</b> Normalized diesel droplet lifetime as a function of fans speed for different ambient pressures at $T_{amb} = 473$ K. ....	70
<b>Figure 4.8.</b> Normalized droplet lifetime of diesel fuel as a function of ambient pressure at $T_{amb} = 473$ K. ....	71
<b>Figure 4.9.</b> Time history for squared normalized diameter of biodiesel droplet for various fan speeds at $P_{amb} = 6$ bar and $T_{amb} = 473$ K for (a) free and forced convection cases and (b) forced convection cases. ....	72
<b>Figure 4.10.</b> Biodiesel droplet lifetime as a function of ambient pressure for various fan speeds at $T_{amb} = 473$ K. ....	73
<b>Figure 4.11.</b> Normalized droplet lifetime of B100 as a function of ambient pressure for various fan speeds at $T_{amb} = 473$ K. ....	74
<b>Figure 4.12.</b> Biodiesel droplet lifetime as a function of ambient pressure for different fan's speed. ....	75

<b>Figure 4.13.</b> Time history of the squared normalized diameter for different fans speeds at $T_{amb} = 473K$ and $P_{amb} = 6$ bar for (a) B20 droplet and (b) B50 droplet.....	77
<b>Figure 4.14.</b> Droplet lifetime as a function of ambient pressure at a given fans speed at $T_{amb} = 473$ K for (a) B20 droplet and (b) B50 droplet.....	79
<b>Figure 4.15.</b> Normalized droplet lifetime as a function of ambient pressure at given fan speeds for (a) B20 droplet and (b) B50 droplet. ....	81
<b>Figure 4.16.</b> Variation of droplet lifetime with ambient pressure at different fan speeds for (a) B20 droplet and (b) B50 droplet. ....	82
<b>Figure 4.17.</b> Comparison of droplet lifetimes for B0, B20, B50 and B100 as a function of ambient pressure at $T_{amb} = 473$ K for (a) 0 RPM and (b) 1000 RPM.....	84
<b>Figure 5.1.</b> Time histories of the normalized droplet projected surface area of diesel droplet burning in turbulent atmosphere at $T_{amb} = 423$ K and $P_{amb} = 1$ bar.....	87
<b>Figure 5.2.</b> B0 droplet burning rate as a function of fan speed for different ambient temperatures at $P_{amb} = 1$ bar.....	89
<b>Figure 5.3.</b> Time histories of the normalized droplet projected surface area of B100 droplet burning with different fan speeds at $T_{amb} = 423$ K and $P_{amb} = 1$ bar. ....	91
<b>Figure 5.4.</b> Snapshots of microexplosion phenomenon occurring during biodiesel droplet combustion for 0 RPM fan speed at $T_{amb} = 423$ K and $P_{amb} = 1$ bar.....	92
<b>Figure 5.5.</b> B100 droplet burning rate as a function of fans speed for various ambient temperatures at $P_{amb} = 1$ bar.....	93
<b>Figure 5.6.</b> Time histories of the normalized droplet projected surface area of B20 droplet burning with different fan speeds at $T_{amb} = 423$ K and $P_{amb} = 1$ bar. ....	94

<b>Figure 5.7.</b> Time histories of the normalized droplet projected surface area of B50 droplet burning with different fan speeds at $T_{amb} = 423$ K and $P_{amb} = 1$ bar. ....	95
<b>Figure 5.8.</b> Comparison of droplet burning rates for B0, B20, B50 and B100 as a function of fan speed at $T_{amb} = 423$ K and $P_{amb} = 1$ bar. ....	96
<b>Figure B.1.</b> Dimensioned drawing of fan shaft seal. ....	B-4
<b>Figure C.1.</b> Dimensioned drawing of fan shaft. ....	C-4
<b>Figure C.2.</b> Dimensioned drawing of shaft press-fit. ....	C-5
<b>Figure C.3.</b> Dimensioned drawing of shaft connection between fan shaft and hardened middle shaft section. ....	C-6
<b>Figure C.4.</b> Dimensioned drawing of hardened middle shaft section. ....	C-7
<b>Figure C.5.</b> Dimensioned drawing of aluminum press fit shaft section. ....	C-8
<b>Figure D.1.</b> Individual heating elements bent according to position. ....	D-3
<b>Figure D.2.</b> Heating plate view from above. ....	D-5
<b>Figure D.3.</b> Drawing of heating element arrangement. ....	D-6
<b>Figure D.4.</b> Dimensions of angled elements (two outside elements). ....	D-7
<b>Figure D.5.</b> Dimensions of straight heating element. ....	D-8
<b>Figure D.6.</b> Dimensioned drawing of heating plate. ....	D-9
<b>Figure E.1.</b> Dimensioned drawing of ignition head [48]. ....	E-2
<b>Figure E.2.</b> Dimensioned drawing of wire igniter. ....	E-3
<b>Figure G.1.</b> Maximum error for diesel droplet vaporization as a function of time. ....	G-3
<b>Figure G.2.</b> Maximum relative error for diesel droplet vaporization as a function of time. ....	G-4
<b>Figure G.3.</b> Maximum error for biodiesel droplet vaporization as a function of time. .	G-5

**Figure G.4.** Maximum relative error for biodiesel droplet vaporization as a function of  
time. .... G-5

## **Chapter 1 - Introduction**

Diesel fuel has been used in internal combustion engines to generate power for many decades; however, petroleum derived fossil fuel reserves are gradually approaching depletion [1] and consequently novel fuel sources must be found. Biodiesel is one of the new fuels that have potential to be used either as a replacement or a supplement to extend the lifespan of petroleum derived diesel fuel [2, 3]. Biodiesel can be produced from vegetable oils as well as animal fats, where these renewable fuel sources are combined with an alcohol (e.g., methanol) to produce fatty acid methyl (and ethyl) esters in a chemical process known as transesterification [1]. Biodiesel fuel is renewable (can be grown from edible and inedible crops [1]) and when burned it emits (in comparison with diesel fuel) less carbon monoxide (CO), particulate matter and unburned hydrocarbon emissions [1, 2, 4].

Droplet vaporization of biodiesel has been studied experimentally over a wide range of ambient temperatures and pressures [5 &6] in free convection environment, whereas diesel [7, 8] and biodiesel-diesel blends [9] have only been experimentally studied at elevated ambient temperature. Numerically diesel, biodiesel and their blends have been studied in free convection atmosphere over a wide range of ambient pressures [10, 11] but only at a few ambient temperatures above the critical temperature of each respective fuel. Most studies on the effect of forced convection on biodiesel, diesel and their blends were done at super critical ambient temperature under atmospheric pressure [12, 13].

Similarly droplet combustion for biodiesel, diesel and their blends has not been experimentally studied with respect to elevated ambient pressure. However, the effect of

elevated ambient temperature has been studied at normal [14, 15] and microgravity [15] conditions. Droplet combustion in the presence of forced convection has been primarily studied experimentally either using the porous sphere technique [16, 17] or with free falling droplets in a furnace [18, 19] with both studies were conducted under atmospheric pressure for a laminar flow. Droplet combustion of biodiesel, diesel and their blends has been studied numerically as part of experimental studies [15, 20, 21] for direct comparison.

Therefore the main goal of the experimental work presented in this thesis was to investigate droplet vaporization and combustion of biodiesel, diesel and their blends under the effect of turbulent flow under elevated ambient pressure and temperature conditions.

The thesis contains 6 chapters with 7 appendices. The literature review is presented in Chapter 2. The experimental setup and test conditions are reported in Chapter 3. The results and discussion for droplet vaporization is presented in Chapter 4, and the droplet combustion is in Chapter 5. Conclusions and recommendations for future work are summarized and reported in Chapter 6. Appendix A contains the technical information regarding all the measurement instrumentation. Appendix B contains technical data regarding the sealing materials and dimensions. Appendix C contains the technical details and drawings of the fan transmission assembly. Appendix D contains the technical details and drawings of the heating system. Appendix E contains the technical details and drawings of the ignition system. Appendix F contains the image processing Matlab code. Lastly, the error analysis for the experimental results can be found in Appendix G.

## **Chapter 2 - Literature Review**

### **2.1. Droplet Vaporization**

In this chapter, published literature concerning the vaporization process of diesel, biodiesel and their blends is reviewed.

#### **2.1.1. Diesel Droplet Vaporization**

Diesel droplet evaporation has been sparsely studied in comparison to diesel spray due to the relatively higher significance of spray in the combustion process. Diesel fuel physically varies from one region to another depending on the refining process [22]. Published work on diesel droplet evaporation will be reviewed with respect to two conditions; free convection and forced convection, where the former can be broken down into two categories; ambient temperature and pressure.

##### **2.1.1.1. Effect of Ambient Temperature**

###### ***Experimental Studies***

Experimental studies focusing on diesel droplet evaporation are limited primarily due to the compositional variety that exists between diesel fuels from different regions of the world. The experimental studies that do exist have shown diesel fuel droplet evaporation only under atmospheric pressure and normal gravity [8, 9, 23]. The reported results of [8] have shown diesel fuel to follow the  $d^2$ -law (e.g., [24]) after an initial heating period at ambient temperatures that ranged from subcritical (684 K) to supercritical (917 K), where the critical temperature of diesel fuel is commonly taken to be approximately 450 Celsius or 723 K. A heating period was observed for all of these ambient temperatures; however, the significance of this unsteady portion of the droplet

lifetime was small while approaching an asymptotic value with respect to ambient temperature. The evaporation rate in contrast to the heating period showed a strong dependence on ambient temperature where it increased monotonically with ambient temperature. High ambient temperature helps diesel droplet evaporation by providing greater heat transfer to the droplet surface while allowing for a more rapid evolution of diesel fuel components from liquid to gaseous phase (i.e., gasification).

Diesel fuel requires elevated ambient temperature to produce vapour [25]. Experimentally, 200 degrees Celsius or 473 K, represents a relatively low ambient temperature in comparison to the boiling point range of diesel fuel, 150-330°C, which can fully evaporate a diesel droplet. Yupo et al. [23] explored diesel droplet evaporation at ambient temperatures of 448 K and 473 K under atmospheric pressure. The diesel fuel was purposely preheated to the approximate ambient temperature before the droplet was formed; this in turn guarantees no heating period will exist allowing for the experiment to solely focus on the evaporation rate. Diesel droplet evaporation was found to follow a linear decrease in the projected surface area of the droplet, indicative of the  $d^2$ -law. This latter allowed for the determination of the evaporation rate, which was found to be 0.19  $\text{mm}^2/\text{s}$  and 0.33  $\text{mm}^2/\text{s}$  for ambient temperatures of 448 K and 473 K, respectively. One comment that must be made about their experimental results is in regard to the reported evolution of the droplet squared diameter with respect to time, particularly for the case of 175°C (448 K), where the final squared diameter used in the calculation of the evaporation rate did not coincide with value used for 200°C (473 K). The final value in question was greater than the final value used for 200°C, which implies that diesel fuel was still present at that point in time. Whether or not the diesel droplet continues to

follow the  $d^2$ -law beyond that diameter is unknown. The overall shape (i.e., linear, etc.) of the surface regression profile comes into question because of the work done by Promvongsa et al.[9] where diesel droplet evaporation was also conducted at 200°C under atmospheric pressure, where the only difference between the two experiments was the diesel fuel preheating done by [23]. Diesel droplet evaporation experiments by [9] produced a non-linear decrease in the projected surface area of the droplet. This non-linear behaviour does not conform to the  $d^2$ -law; this in turn prevents the determination of the evaporation rate, even though Promvongsa attempted to plot a best fit through the data. The main reason behind this non-linear behaviour was attributed to the multicomponent nature of diesel fuel and the wide range of volatilities present within diesel fuel. The authors fail to mention that the wide range of components present within diesel fuel, which is evident given the boiling point range of diesel fuel. This shows that there are some very heavy components (i.e., high molecular weight) as well as some relatively light components (i.e., low molecular weight). Diesel droplet evaporation had no observable heating period for this relatively low ambient temperature due to the evaporation of the lighter components allowing time for the droplet surface temperature to enable evaporation of the relatively heavier components. Unfortunately, the ambient temperature in this case was insufficient to enable a progressive transition from one component to another to facilitate evaporation that would follow the  $d^2$ -law.

Kobayasi [7] experimentally studied the evaporation of light diesel oil under atmospheric pressure for ambient temperatures ranging from 475 K to nearly 1000 K. Surface regression profiles were only presented for ambient temperatures of 198, 300 and 305 °C. The evolution of the surface regression profile shows an initial heating period

followed by a steady decline, where the surface area decreases non-linearly, particularly for 198 °C. The author chose to quantify droplet evaporation using a mean evaporation rate for all of the tested ambient temperatures where this value was derived from the slope of a straight line that connected the initial and final points of the droplet lifetime. The mean evaporation rate was found to increase steadily with ambient temperature. This method of computing the evaporation rate does not agree with the  $d^2$ -law, however, this work was conducted around the time that the  $d^2$ -law was first being proposed by Godsave [26].

From the previously mentioned works it is obvious that there some ambiguities still exist regarding the diesel fuel droplet evaporation, particularly in regards to the evaporation behaviour at relatively low ambient temperatures, where it remains uncertain whether or not diesel follows the  $d^2$ -law, as well as the existence or non-existence of a heating period.

### *Numerical studies*

Diesel droplet evaporation has been primarily studied numerically under the presence of relatively high ambient temperatures (i.e., temperatures above the critical temperature) [27-29]. Zhang and Kong [27] simulated diesel droplet evaporation for ambient temperatures of 858, 912 and 1019 K under atmospheric pressure, they reported that the associated lifetimes for a droplet with a 1 mm diameter were 5.53, 4.51 and 3.86 seconds, respectively. Interestingly, the authors chose to report droplet lifetime rather than evaporation rate despite having the droplet surface regression profiles that follow the  $d^2$ -law after an initial heating period. Unlike other authors, Zhang and Kong validate their

model with experimental droplet data for n-heptane, n-decane and biodiesel from [6]. Using biodiesel to validate their numerical work shows that the model can produce reliable results regarding multicomponent droplet evaporation, however, although biodiesel may be a multicomponent droplet; it has a significantly narrower range of component in comparison to diesel fuel.

Lippert and Reitz [28] simulated diesel droplet evaporation under relatively high ambient temperature (973 K) at atmospheric pressure. They found that while an initial heating period was present, it was quickly followed by a linear decrease in the squared diameter of the droplet indicative of the  $d^2$ -law. Their simulation predicted an evaporation rate of  $0.32 \text{ mm}^2/\text{s}$ , this value showed close agreement to previous numerical works, however, comparison of the droplet lifetime to previous numerical work of Tamim and Hallett [29] showed a noticeable difference of around 30 percent.

Zhang and Kong [30] simulated diesel droplet evaporation under the same conditions as Lippert and Reitz [28], and they found a similar behaviour with respect to the evolution of the droplet's surface regression profile. However, Zhang and Kong [30] conducted this simulation on droplet evaporation without comparing the results to previous work of Lippert and Reitz. These mentioned numerical works only focused on diesel droplet evaporation for one ambient temperature whereas the work of others has focused on a wider range of ambient temperatures.

Hallett [31] simulated diesel droplet evaporation and compared the predicted evaporation rates with the experimental data of Kobayasi [7] over the entire ambient temperature range explored in [7]. The range of ambient temperatures spanned from

subcritical to supercritical, where the evaporation rate was presented using a logarithmic scale. This scale shows the temperature dependence of diesel droplet evaporation for both sub- and supercritical temperatures. The numerical results showed good agreement with the experimental data regarding the evaporation rate despite the uncertainties associated with the fuel specifications used by [7]. The numerical models showed that, over the entire range of ambient temperatures, the diesel droplet evaporation followed the  $d^2$ -law after an initial heating period; however, the relative size of the heating period could not be compared to [7] because this information was not available. Comparatively, the numerical work done by Daho et al. [8] compared not only the evaporation rate, but also compared the temporal length of the heating period to their own experimental data for ambient temperatures ranging from 684 K to 917 K. Numerical models used by [8] consistently overestimated the length of the heating period as well as the droplet lifetime of diesel fuel in comparison to experimental data. On the other hand, the evaporation rate was consistently underestimated by the numerical models, with the exception of one numerical model that only included the effects of natural convection. The authors concluded that the heating period has little influence over the evaporation rate in comparison to the presence of natural convection over the range of ambient temperatures studied.

The effect of ambient temperature on diesel droplet evaporation was briefly studied by Ra and Reitz [11] for an ambient pressure of 4 MPa, where the ambient temperature was varied from 500 K to 1000 K. The authors found that for ambient temperatures greater than the critical temperature of the fuel, the surface temperature of the droplet reached the critical value and proceeded to vaporize immediately.

Comparatively, subcritical ambient temperatures produced longer droplet lifetimes, where the droplet lifetime increased significantly with decreasing ambient temperature.

From the above discussion, it appears that diesel droplet evaporation has been studied numerically over a range of ambient temperatures, with some of the models making direct comparisons with available experimental data, while others have only been compared with previous numerical works due to a lack of compositional knowledge regarding the fuel. The evaporation rate has been simulated for ambient temperatures ranging from sub- to supercritical, where fair agreement was found with experimental data, however, there are still problems in obtaining an accurate estimation of the heating period and consequently the droplet lifetime. The limited works examining the effect of ambient temperature at elevated ambient pressure is also noteworthy as discussed below.

#### **2.1.1.2. Effect of Ambient Pressure**

##### *Numerical Studies*

Numerical studies have been so far the only method for studying diesel droplet evaporation at elevated ambient pressure. Chin and Lefebvre [32] studied diesel droplet evaporation where the simulation focused only on the quasi-steady portion of evaporation rather than its entire lifetime. The diesel droplet evaporation rate results were compared with experimental data at ambient temperature and pressure of 2000 K and 1 atm, respectively. The calculated evaporation rate was less than 2 percent off of the experimental value; unfortunately further validation of diesel droplet evaporation at conditions involving elevated ambient pressure were not available due to the lack of experimental data. The authors examined five ambient temperatures, 500, 800, 1200,

1600 and 2000 K and varied ambient pressure from 0.1 MPa to 2 MPa in a quiescent environment. It should be noted that the critical temperature and pressure of diesel were taken to be 725.9 K and 2.089 MPa, respectively. The evaporation rate was found to increase with ambient pressure for supercritical ambient temperatures, whereas this behaviour reverses at subcritical ambient temperatures. Further examination regarding the pressure dependence of the evaporation rate of diesel fuel shows a relationship where the evaporation is directly proportional to pressure to the power of  $n$ , where the value of  $n$  varies as  $\pm 0.25$ . Interestingly, the value of  $n$  equals zero at 750 K for all ambient pressures, while the  $n$  values for subcritical and supercritical temperatures follow a similar behaviour with respect to ambient pressure to what was observed for the evaporation rate. Diesel droplet evaporation undergoing this subcritical-supercritical behaviour has also been studied more recently by Ra and Reitz [11].

Ra and Reitz [11] studied diesel droplet evaporation for a variety of ambient temperature and pressure conditions, as well as the initial droplet temperature. One of the test conditions presented was for ambient temperature and pressure of 500 K and 0.1 MPa, respectively, in conjunction with an initial droplet temperature of 360 K. Diesel droplet evaporation under these ambient conditions reveals a non-linear decrease in the surface area of the droplet, where the simulation showed the lightest components vaporizes initially, allowing for the heaviest components of the droplet to control the final stages of evaporation. They showed that a reduction in the ambient pressure below 0.1 MPa combined with the above mentioned ambient temperature and initial droplet temperature causes a reduction in the droplet lifetime. There was no heating period found for ambient pressures below 0.1 MPa, whereas for higher ambient pressures a heating

period was not only present, but also becomes important with respect to ambient pressure. Using an ambient temperature of 800 K, the ambient pressure was increased from 0.1 MPa to 4 MPa, where the droplet surface area was found to decrease non-linearly. The droplet lifetime increased with pressure until 2 MPa, beyond which the droplet surface temperature was able to reach the critical temperature and immediately vaporized.

Zhu and Reitz [33] studied diesel droplet evaporation for various pressures spanning from 0.186 MPa to 13.02 MPa at an ambient temperature of 950 K. The model was used to simulate the entire droplet lifetime. A heating period was found to exist for all of the ambient pressures; this was attributed to the initial surface vapour fraction and evaporation rate having small values due to the low volatility of diesel fuel. The effect of increasing ambient pressure had minimal effect on the heating period; however, it reduced the droplet lifetime by increasing the rate of vaporization. Ambient pressure was found to reduce both the enthalpy of vaporization and the liquid density due to increased gas absorption; these two effects were believed to be responsible for the reduction of the droplet lifetime at elevated ambient pressures.

The reviewed literature revealed that the effect of ambient pressure on diesel droplet evaporation has been primarily studied using supercritical ambient temperatures, where the one study that examines subcritical temperatures was only concerned with the quasi-steady portion associated with the evaporation rate, while ignoring the potential effects of the heating period on the droplet lifetime. The heating period becomes more significant as ambient pressure increases, while the general non-linearity associated with the temporal progression of the droplet surface area shows a general trend of non-

conformism to the classical  $d^2$ -law. The developed numerical models were not validated using (or compared with) experimental data. This is due to the lack of experimental data/studies.

### **2.1.1.3. Effect of Forced Convection Flow**

#### *Numerical Studies*

The effect of forced convection on diesel droplet evaporation has been studied sparsely with the primary focus of these studies involving supercritical ambient temperatures under atmospheric pressure [34, 35]. Barata [34] simulated injecting a diesel droplet into a hot convective cross flow, where the cross flow velocity was taken to be 10 m/s and the ambient temperature was 800 K. The evaporation of the diesel droplet undergoes a noticeable heating period before evaporating. Neither the evaporation rate nor the droplet lifetime was mentioned. On the other hand, Saha et al. [35] also simulated diesel droplet evaporation under the same ambient conditions as Barata [34], where the evolution of the droplet size was presented for two initial droplet sizes, 20  $\mu\text{m}$  and 400  $\mu\text{m}$ , respectively. The normalized droplet diameter was shown to decrease linearly over time for the 400  $\mu\text{m}$  droplet, whereas the 20  $\mu\text{m}$  droplet was shown to have a non-linear decrease in the normalized diameter. Similarly to [34], there was no quantification regarding the evaporation rate or the droplet lifetime for both droplet diameters and there was no indication either if the droplet followed the  $d^2$ -law. In contrast to the previously mentioned authors, Saha et al. [36] simulated diesel droplet evaporation for a 100  $\mu\text{m}$  droplet injected into a hot stagnant environment with an initial velocity of 5 m/s. Diesel droplet evaporation began with a relatively short heating period followed by an approximately linear decrease in the droplet surface area with respect to time. The linear

regression of the droplet surface area was associated to maintaining a constant wet bulb temperature, where the authors claim that the wet bulb temperature represents thermal equilibrium for a droplet whose boiling point is less than the ambient temperature.

Chin and Lefebvre [12] simulated diesel droplet evaporation in the presence of forced convection. The focus of their simulation was on the ratio of heating period to droplet lifetime. They observed that the heating period did not change with flow velocity; however, the evaporation rate was described as increasing with flow velocity which in turn increased the ratio of heating period time to droplet lifetime. Interestingly, the surface temperature of the droplet was found to remain constant while varying the flow velocity. Simulations were carried out for ambient temperatures of 500 K and 2000 K as well as ambient pressures of 0.1 MPa and 2 MPa. The ratio of heating period to droplet lifetime was found to increase with flow velocity at elevated ambient pressure, where the heating period was found to increase with ambient pressure.

It can be seen from the literature above that diesel droplet evaporation in the presence of forced convection has yet to be examined in regard to the applicability of the  $d^2$ -law and hence determining the vaporization rate. The focus was more on the heating period. On the other hand, the literature revealed that experimental investigations of diesel droplet evaporation in the presence of forced convective flow are still missing.

### **2.1.2. Biodiesel Droplet Vaporization**

Biodiesel fuel physical properties are dependent on the feedstock type, where only a handful of biodiesels have been explored in regard to droplet evaporation, primarily soybean, canola, rapeseed and sunflower oil derived biofuels.

### **2.1.2.1. Effect of Ambient Temperature**

#### ***Experimental Studies***

Droplet evaporation using biodiesel derived from rapeseed and sunflower oil has been explored by the work of Morin et al. [5] for ambient temperatures ranging from 473 K to 1020 K under atmospheric pressure. Both biodiesels displayed similar behaviour with respect to the evaporation rate and the length of the heating period. The significance of the heating period was found to be most prominent at 600 K, where the heating period represented 60 percent of the droplet lifetime. Below 600 K, the heating period represented less than 20 percent of the lifetime; however, above 600 K, the increased ambient temperature reduced the heating period to approximately 40 percent of the droplet lifetime. After the elapse of the heating period, the projected droplet surface decreased linearly where the  $d^2$ -law was found to be applicable. This has been confirmed for soybean biodiesel examined by [37]. The average vaporization rates for both biodiesels were found to be very close, where the evaporation rate increased monotonically with ambient temperature. Interestingly, a residue remained on the quartz fiber at the end of evaporation for ambient temperatures between 523 K and 773 K, however this residue material disappeared for higher ambient temperatures. Further study of biodiesel droplet evaporation was conducted by Morin et al. [6] by varying ambient temperature as well as ambient pressure for rapeseed biodiesel in a comparative study with n-decane. The effect of ambient temperature on the heating period at elevated ambient pressures was not mentioned directly, however, the authors mentioned that the evaporation rate could not be used to solely characterize the biodiesel droplet evaporation. The evaporation rate increased with ambient temperature for temperatures

below the critical temperature; however these increases were relatively small in comparison with the observed changes in the supercritical region.

Promvongsa et al. [9] studied palm oil biodiesel droplet evaporation at a relatively low ambient temperature of 473 K at atmospheric pressure. The fuel displays an initial heating period that quickly transitions into a quasi-linear decrease in the projected surface area. The authors believe that the  $d^2$ -law may not be applicable to palm oil biodiesel droplet evaporation despite the relatively linear decrease in the projected surface area. This contrasts the work that [5] had done with rapeseed biodiesel for a similar ambient temperature of 481 K, where an approximately linear decrease in the projected surface area was observed (i.e., the  $d^2$ -law). This ambiguity regarding the  $d^2$ -law around this relatively low ambient temperature may be due to the differences in physical properties of the biodiesels.

From the above discussion, it can be seen that information regarding the effect of ambient temperature on the heating period at elevated ambient pressure still has to be examined. The evaporation rate was measured for elevated ambient pressures and temperatures, however, there was no observable trend regarding the effect of ambient temperature on biodiesel droplet evaporation reported by the authors. The effect of ambient temperature on the evaporation rate of biodiesel droplet at atmospheric pressure has been found to increase the evaporation rate monotonically. The  $d^2$ -law was observed for ambient temperatures greater than 473 K, however, one author questions the applicability of the  $d^2$ -law at 473 K, therefore further work may be needed to clarify if biodiesel droplet evaporation at 473 K does indeed follow the  $d^2$ -law.

### *Numerical Studies*

Zhang and Kong [27] simulated soybean biodiesel evaporation for supercritical ambient temperatures of 858 K, 912 K and 1019 K at atmospheric pressure. The biodiesel droplet initially undergoes a noticeable heating period due to the relatively low volatility, which transitions into a fairly linear surface regression profile. The droplet lifetimes have been reported as 8.11, 6.20 and 5.08 seconds for the previously mentioned ambient temperatures. The droplet lifetime decreases rapidly with ambient temperature especially since all the tested ambient temperatures are beyond the critical temperature of biodiesel. The numerical model was validated using experimental data for single component (n-heptane) droplets, bi-component (decane and n-heptane) droplets as well as biodiesel droplets to validate the model for high temperature vaporization simulation. The biodiesel data used for validation was taken from [5].

Dirbude et al. [38] simulated droplet vaporization of rapeseed and sunflower oil derived biodiesel for ambient temperatures that ranged from 550 K to 1050 K at atmospheric pressure under near quiescent conditions. The flow is meant to simulate the free convection environment that was present in the experimental work of Morin et al. [5]. The model focuses on the quasi-steady evaporation portion of the droplet lifetime only; therefore the heating period was exempt from this simulation by assuming an initial droplet surface temperature of 415 K. Five convective correlations taken from literature [38] were used to reproduce the experimental evaporation rate for rapeseed and sunflower oil derived biodiesels that was observed by Morin et al. [5]. Three of the correlations only accounted for convection, while the remaining two correlations included convection and the blowing effect. The correlations that incorporated the blowing effect which were

expected by the authors to be effective for the higher evaporation rates associated with higher ambient temperatures were found to overestimate the droplet lifetime, whereas two of the correlations that only included convection were found to give the closest fit to the experimental data. The  $d^2$ -law was observed because the simulation only considers the quasi-steady portion of biodiesel droplet evaporation. This shows agreement with the work done by Hallett and Legault [37] where soybean biodiesel droplet evaporation was simulated and subsequently verified by experiment for ambient temperatures ranging from 693 K to 993 K, where the  $d^2$ -law was also observed.

From the above discussion, it can be seen that the effect of ambient temperature on biodiesel droplet evaporation has been primarily examined for atmospheric pressure, leaving a gap in knowledge regarding the combination of elevated ambient temperature and pressure. There is little work that has simulated the entire droplet lifetime of biodiesel, which is surprising considering the importance of the heating period in the overall droplet lifetime which has been shown in previous experimental work [5]. There is an apparent lack of numerical work regarding droplet evaporation regarding biodiesel derived from a wide range of feedstocks.

#### **2.1.2.2. Effect of Ambient Pressure**

##### ***Experimental Studies***

Biodiesel droplet evaporation under different ambient pressures has been experimentally studied by Morin et al. [6] using rapeseed derived biodiesel. The ambient temperatures ranged from 573 K to 973 K and the ambient pressure was varied from 0.1 MPa to 5 MPa under normal gravity conditions. Biodiesel droplet evaporation was found

to have a heating period for all of the ambient conditions tested; however, this information was not presented, whereas the information regarding the evaporation rate was presented. The evaporation rate was found to increase with ambient pressure for pressures greater than the critical pressure for ambient temperatures up to 873 K. Below the critical pressure, only two ambient pressures were used; atmospheric pressure and 1 MPa, where the evaporation rate also increased with ambient pressure for ambient temperatures of 673 K and higher. The general trend that the evaporation rate increases with ambient pressure does not mean that the droplet lifetime decreases with ambient pressure, especially since the authors have commented that the evaporation cannot be used as the sole parameter to characterize biodiesel droplet evaporation.

From the above discussion, it can be seen that while the evaporation rate has been presented for a large range of ambient conditions, there are still questions regarding the droplet lifetime especially since the heating period was not presented. It is clear that the limited range of ambient subcritical pressure examined so far is insufficient to form a trend and thus requires further experimentation.

### *Numerical Studies*

Zhang and Kong [10] simulated the effect of ambient pressure on biodiesel droplet evaporation for an ambient temperature of 900 K. Ambient pressure was varied from 0.1 MPa to 5 MPa, where two observations were made; the first shows that ambient pressure extends both the temporal and physical swelling of the heating period, and the second shows that the droplet lifetime decreases with ambient pressure. The reduction of the droplet lifetime due to ambient pressure is a result of the increased surface

temperature of the droplet as well as the reduced enthalpy of vaporization. The authors noted that the rate of vaporization increases with ambient pressure only beyond a threshold ambient temperature, where the effect of ambient pressure below that threshold has the opposite effect. Investigation of the threshold temperature was conducted on diesel droplet evaporation; however, the authors had noted that each fuel should have a unique threshold temperature.

Zhang and Kong [10] validated their numerical model using experimental data for n-heptane droplet evaporation for elevated ambient temperature and pressure. The results showed good agreement with the published data.

From the above discussion, it can be seen that the effect of ambient pressure has only been numerically studied for biodiesel droplet evaporation at an ambient temperature greater than the critical temperature of the fuel. Further investigation into ambient pressure effects involving subcritical ambient temperatures are still needed. The numerical model used by Zhang and Kong [10] was validated using experimental data for n-heptane droplet evaporation as opposed to using experimental data for biodiesel droplet evaporation.

### **2.1.2.3. Effect of Forced Convective Flow**

#### ***Numerical Studies***

Biodiesel droplet evaporation in the presence of forced convective flow has only been studied numerically to date; where all of the studies focused on evaporation at atmospheric pressure at an ambient temperature of 800 K. Saha et al. [36] examined the vaporization of biodiesel in a hot convective flow with an initial velocity of 5 m/s. The

evaporation of the droplet was found to have an initial heating period followed by a quasi-steady decrease in the droplet surface area following the  $d^2$ -law. No comparison between these results and free convection droplet evaporation were made. The numerical model was validated using experimental data for bi-component droplets composed of n-heptane and decane.

Barata [34] simulated droplet evaporation for rapeseed derived biodiesel in a hot turbulent cross flow. Simulations used an ambient temperature of 800 K at atmospheric pressure and a cross flow velocity of 10 m/s. The biodiesel droplet was simulated with preheating to 443 K and without preheating. The preheating effect was found to significantly reduce the droplet heating period as well as the droplet lifetime. The author presented very little information regarding droplet evaporation, as the prime focus of the paper was on droplet dispersion within a spray.

Saha et al. [35] simulated droplet vaporization using rapeseed derived biodiesel in the presence of a hot convective flow at atmospheric pressure. Two initial droplet sizes were used in the simulation; 20  $\mu\text{m}$  and 400  $\mu\text{m}$ . The progression of the droplet lifetime was given as the normalized droplet diameter rather than the normalized square diameter; which does not confirm with the  $d^2$ -law. The presented results showed that no heating period was observed for both droplet sizes. Unfortunately, the evaporation rate was not presented, whereas the droplet lifetime was shown, however, this result was not compared with literature. The effect of forced convection was not compared to free convection, as the focus of the study was on the comparison of biodiesel-diesel blends.

Gu et al. [13] numerically simulated droplet evaporation using rapeseed derived biodiesel in a hot turbulent cross flow, where the ambient temperature was 800 K at atmospheric pressure with a flow velocity of 10 m/s and an injection velocity of 3.5 m/s. The injection velocity was selected by the author as an optimized value. The cross flow turbulence intensity was 20 percent of the mean cross flow kinetic energy. Droplet evaporation was studied with respect to the evolution of the diameter rather than the squared diameter. The droplet lifetime was presented in comparison to other fuels such as Jet-A fuel, where there was no mention of heating period or evaporation rate or if the droplet followed the  $d^2$ -law. The effect of forced convection was never mentioned. The numerical model was validated using experimental data for a bi-component droplet composed of n-heptane and decane under a forced convection using a relatively low ambient temperature as well as using experimental data for forced convection at relatively high ambient temperature for pure decane droplet evaporation.

From the above discussion, it can be seen that there are very limited studies regarding biodiesel droplet evaporation under forced convection, where no comparisons between forced and free convection were made as well as no comparisons between the respective studies that simulated the phenomenon. There is no numerical work regarding biodiesel droplet evaporation under forced convection at elevated ambient pressure. All studies used the same ambient temperature (i.e., 800 K), leaving a lot room of expansion in this field of study. There is also no experimental work to this author's knowledge regarding biodiesel droplet evaporation under forced convection.

### **2.1.3. Droplet Vaporization Biodiesel-Diesel Blends**

#### **2.1.3.1. Effect of Ambient Temperature**

##### *Experimental Studies*

Promvongsa et al. [9] studied droplet evaporation using biodiesel-diesel blends of 5, 10, 20 and 50 percent by volume of palm oil biodiesel. Droplet evaporation was conducted at a relatively low ambient temperature of 473 K under atmospheric pressure. The evaporation of the fuel droplet blends was observed to have no heating period. The authors found that by adding only 5 percent biodiesel to pure diesel fuel, the evaporation rate was decreased by 20 percent. The evaporation rate was found to decrease with biodiesel content within the blend. The ambient temperature used was not sufficiently high enough for diesel fuel to follow the  $d^2$ -law, whereas biodiesel shows a linear trend. The blends were found to follow the  $d^2$ -law. The authors further noted that the  $d^2$ -law can be applied to certain droplet blends of biodiesel and diesel fuel.

From the above discussion, it can be seen that very little experimental work has been done in regards to droplet evaporation of biodiesel-diesel blends. Further work is needed particularly at higher ambient temperatures as well as higher ambient pressures, where no experimental work could be found in the literature in regards to droplet evaporation of biodiesel-diesel blends at elevated ambient pressures.

##### *Numerical Studies*

Zhang and Kong [27] simulated droplet evaporation of biodiesel-diesel blends of 5 and 20 percent by volume of soybean biodiesel. The ambient temperatures used for this simulation were 858 K, 912 K and 1019 K under atmospheric pressure. The droplet

lifetime was found to increase with biodiesel content within the blend; however, the heating period observed for the blends mirrored that of diesel fuel whereas pure biodiesel required a longer heating period. The differences in the droplet lifetime between the blends occurred after the heating period, where the slopes of the surface regression profiles were found to be quite similar, with differences resulting from biodiesel content. The droplet lifetime of each fuel blend decreased with ambient temperature; however, there was no mention of the evaporation rate. The numerical study found that the majority of the diesel components will evaporate before the biodiesel components begins to evaporate; this is a result of biodiesel components having lower volatilities in comparison to the majority of the diesel components. Near the end of evaporation most of the biodiesel components have evaporated, where the heaviest diesel components still remain. This shows that the volatility of the fuel components controls the evolution of the droplet composition during evaporation.

From the above discussion, it can be seen that droplet evaporation of biodiesel-diesel blends have only been studied numerically under ambient temperatures greater than the critical temperature of both parent fuels. The reported results make mention of blended fuel droplets having different slopes, but they did not mention whether or not these blended droplets followed the  $d^2$ -law. Further numerical work is needed regarding the effect of ambient pressure under elevated ambient pressure on biodiesel-diesel blended droplet evaporation.

### **2.1.3.2. Effect of Ambient Pressure**

#### *Numerical Studies*

Zhang and Kong [10] numerically studied droplet evaporation of biodiesel-diesel blends for a 20 percent by volume blend of biodiesel. The ambient temperature used in this study was 900 K and the ambient pressure ranged from 0.1 MPa to 5 MPa. The droplet lifetime was found to decrease with ambient pressure, where the initial heating period grew both temporally and in volume swelling; however, once the heating period ends the rate of vaporization increases with ambient pressure netting a lower droplet lifetime. The ambient pressure reduced the mass transfer as well as the enthalpy of vaporization; these two factors compete with each other during the heating period until a balance is found with respect to the droplet surface temperature. Once a balance is reached, rapid vaporization occurs, particularly for ambient pressures beyond the critical pressure of both fuels.

It is clear that the effect of ambient pressure on droplet evaporation of biodiesel-diesel blends has only been studied for one fuel blend as well as only one ambient temperature. Further numerical work is needed to investigate the effect of ambient pressure on other fuel blends in conjunction with ambient temperatures, particularly ambient temperatures below the critical temperature of both parent fuels. Experimentally there is no available information regarding droplet evaporation of biodiesel-diesel blends at elevated ambient temperatures.

### **2.1.3.3. Effect of Forced Convection**

#### *Numerical Studies*

Saha et al. [36] numerically studied droplet evaporation of biodiesel-diesel blends in the presence of a hot convective flow for blends of 20 (B20) and 50 (B50) percent by volume biodiesel. The ambient temperature and pressure were 800 K and 0.1 MPa, respectively, with an initial velocity of 5 m/s. The simulated results show the B20 blend initially has a similar surface regression profile to that of diesel fuel for the first half of the droplet lifetime, after which the droplet evaporation rate appears to slow down with an entirely different surface regression rate. The B50 blend also follows this trend with the exception of having a slightly longer heating period, followed by a slower evaporation rate that transitions more quickly into a slower evaporation rate that is very similar to pure biodiesel. This behaviour is quite similar to that of a bi-component droplet where the more volatile component dominates the initial stages of evaporation followed by the less volatile component. The bi-component nature of these multicomponent droplets is part of the given assumptions which was validated using experimental data for a bi-component droplet composed of n-heptane and decane. Unfortunately, this study did not compare the effect of forced convection with the effect of free convection.

Saha et al. [35] numerically studied droplet evaporation of biodiesel-diesel blends in the presence of a hot convective flow for blends of 10, 20 and 50 percent by volume of rapeseed biodiesel. The ambient temperature and pressure were 800 K, and 0.1 MPa, respectively, with a flow velocity of 10 m/s. The fuel droplets were injected perpendicularly into the cross flow with a velocity of 1 m/s. The droplet lifetime was presented with respect to the droplet diameter rather than the squared droplet diameter

versus time. The blended fuel droplets were observed to not have a heating period, where the droplet diameter was found to decrease linearly with time. Whether or not the  $d^2$ -law can be applied to these droplets is presently unknown. The effect of forced convection on the blended fuel droplets was not investigated directly and no comparison was made with the free convection case.

From the above discussion, it can be seen that the effect of forced convection on droplet evaporation of biodiesel-diesel blends has been sparsely studied numerically, where the same ambient conditions (i.e., temperature and pressure) were used with the difference being the velocity of the droplet relative to the flow. There is further numerical work needed to directly study the effect of forced convection on droplet evaporation of biodiesel-diesel blends for both elevated ambient pressure as well as different ambient temperatures. There is currently no experimental work available that studies the effect of forced convection on biodiesel-diesel droplet evaporation.

#### **2.1.4. Conclusions**

In summary, diesel droplet vaporization under free convection has been studied experimentally at elevated ambient temperatures and atmospheric pressure, whereas numerical studies have examined the effects of both ambient temperature and pressure. Contrastingly, biodiesel droplet vaporization has been studied experimentally under free convection conditions for a wide range of ambient temperatures and pressures, whereas numerical studies have examined only selected ambient temperatures coupled with pressures. Droplet vaporization of blends of biodiesel and diesel fuel has been studied for a limited range of ambient conditions both experimentally and numerically. However, there are no published experimental or numerical studies on the vaporization of biodiesel,

diesel or their blends droplet under forced convective flow at elevated ambient temperature and pressure conditions. A summary of literature on droplet vaporization of diesel, biodiesel and their blends is given in Table **2.1**.

**Table 2.1.** Summary of literature on droplet vaporization of diesel, biodiesel and their blends.

Ref.	Fuel Type	Ambient Conditions ( $P_{\infty}$ , $T_{\infty}$ )	Flow Conditions	Droplet Suspension Technique (Diameter)	Initial Diameter [mm]	Study
[5]	B100 (rapeseed and sunflower oil)	473-1020 K; 1 bar	Free convection	Single fiber* (0.4 mm)	0.70-1.30	Exp.
[6]	B100 (rapeseed oil)	473-973 K; 1-50 bar	Free convection	Single fiber* (0.4 mm)	0.87-1.23	Exp.
[7]	B0 (diesel)	471-1073 K; 1 bar	Free convection	Single fiber* (0.1-0.2 mm)	0.70-1.70	Exp.
[8]	B0	684-917 K; 1 bar	Free convection	Single fiber* (0.4 mm)	1.00-1.42	Exp. and Num.
[9]	B0, B5, B10, B20, B50 and B100 (palm oil)	473 K; 1 bar	Free convection	Single wire** (0.2 mm)	N/a	Exp.
[10]	B0, B20 and B100 (5 methyl esters)	900 K; 1-50 bar	Free convection	N/a	0.10	Num.
[11]	B0	500-1000 K; 1-40 bar	Free convection	N/a	0.10	Num.
[12]	B0	500-2000 K; 1-20 bar	Laminar (0-70 m/s)	N/a	0.01-0.20	Num.
[13]	B100 (rapeseed oil)	800 K; 1 bar	Turbulent cross-flow ( $U=10$ m/s, $I=20\%$ )	N/a	0.08	Num.
[23]	B0	398-473 K; 1 bar	Free convection	Single fiber* (N/a)	2.50	Exp.
[27]	B0, B5, B20 and B100 (5 methyl esters)	748-1019 K; 1 bar	Free convection	N/a	0.87-1.23	Num.
[28]	B0	973 K; 1 bar	Free convection	N/a	0.10	Num.
[30]	B0	973 K; 1 bar	Free convection	N/a	0.10	Num.
[31]	B0	473-1000 K; 1 bar	Free convection	N/a	1.20-1.30	Num.
[32]	B0	2000 K; 1-20 bar	Free convection	N/a	N/a	Num.
[33]	B0	950 K; 1.86-130 bar	Free convection	N/a	0.03	Num.
[34]	B0, B100 (rapeseed oil)	800 K; 1 bar	Laminar flow (10 m/s)	N/a	0.23	Num.
[35]	B0, B10, B20, B50 and B100 (rapeseed oil)	800 K; 1 bar	Laminar flow (10 m/s)	N/a	0.02 and 0.40	Num.
[36]	B0, B20, B50 and B100 (rapeseed oil)	800 K; 1 bar	Laminar flow (5 m/s)	N/a	0.10	Num.
[37]	B100 (soybean oil)	693-993 K; 1 bar	Free convection	Single fiber* (0.7 mm)	1.50-1.70	Exp. and Num.
[38]	B100 (rapeseed and sunflower oil)	550-1050 K; 1 bar	Free convection	N/a	1.23	Num.

\*Quartz fiber. \*\*Thermocouple wire.

## **2.2. Droplet Combustion**

The literature regarding combustion of diesel fuel, biodiesel and their blends is reviewed in this section.

### **2.2.1. Diesel Droplet Combustion**

#### **2.2.1.1. Effect of Ambient Temperature**

##### *Experimental Studies*

Kobayasi [14] experimentally studied droplet combustion of light diesel oil under atmospheric pressure and normal gravity. The droplets were observed having an initial heating period prior to combusting. The heating period is directly related to the ignition delay where Raslavicius and Bazaras [39] found that the ignition delay can represent a significant portion of the droplet lifetime (ignition delay was measured from the time the droplet was first placed within the hot environment until the droplet ignited) and which decreases with ambient temperature. The ambient temperature range used by [39] was from 930-1010 K, and Kobayasi [14] used an ambient temperature range of 901-1268 K where the burning rate was found to increase monotonically with ambient temperature. This relationship between burning rate and ambient temperature was also observed by Saito et al. [40] for similar experimental conditions where diesel droplet combustion was conducted in the presence of acoustic oscillations (e.g., sound waves). The relative effect of the acoustic oscillations were observed to enhance the droplet burning rate by allowing the flame temperature to be 673-1073 K higher than the non-oscillating case. The flame temperature was found to be independent of ambient temperature without oscillations present in the flow [40]. Normal gravity experiments benefit from buoyancy induced

flow (e.g., free convection) whereas microgravity does not have this advantage. In fact the lack of flow under microgravity allows for the formation of a soot shell around the droplet surface between the flame and liquid fuel [41]. Pan et al. [41] observed that the burning rate under microgravity is dependent on the droplet size where a larger droplet (528  $\mu\text{m}$ ) would form a soot shell as opposed to a small droplet (445  $\mu\text{m}$ ). The large droplet's soot shell caused a noticeable reduction in the droplet burning rate.

### ***Numerical Studies***

Raslavicius and Bazaras [42] numerically studied diesel droplet combustion under atmospheric pressure and normal gravity. The ambient temperature was varied from 770-860 K. Ignition delay was the primary focus of the study where ambient temperature causes a reduction of the ignition delay, whereas droplet size was found to significantly delay droplet combustion. Droplet size was found to have a more substantial impact for lower ambient temperatures in comparison to the highest values used in the study.

It can be seen that the effect of ambient temperature on diesel droplet combustion has been studied for both normal gravity and to a lesser extent, microgravity. Ignition delay and burning rate both strongly depend on the ambient temperature, whereas the production of soot only becomes a significant issue under microgravity conditions.

#### **2.2.1.2. Effect of Ambient Pressure**

##### ***Experimental Studies***

Diesel droplet combustion was experimentally studied with respect to ambient pressure by Gollahalli et al. [43]; however the combustion involved emulsions of diesel and water rather than pure diesel fuel. The study only focused on droplet fragmentation

with respect to ambient conditions. This study [43] was the only available work dealing with the effect of ambient pressure on diesel droplet combustion where no numerical studies could be found. Considering this study which examined only droplet fragmentation, other aspects of droplet combustion such as burning rate, flame standoff ratio, etc. can still be explored for the effect of ambient pressure.

### **2.2.1.3. Effect of Forced Convection**

#### ***Experimental Studies***

Experimentally the effect of forced convection on diesel droplet combustion has been studied using two methods; firstly using the porous sphere technique at room temperature and pressure; and secondly using free falling droplets in a furnace. Both experimental methods operate at normal gravity under atmospheric pressure. Rajesh et al. [20] used the porous sphere technique and varied the free stream velocity from 0.4 to 2 m/s where the transition velocity associated with the change from an envelope flame to a wake flame was observed; however the exact velocity of the transition was not reported. The mass burning rate was found to increase with free stream velocity where this has also been observed by [17] using blends of diesel and ethanol. Instead of using a porous sphere, Li et al. [18] studied free falling diesel droplets under an ambient temperature that was maintained between 980K and 1040 K. The falling droplet velocity was not reported; however, the presence of a heating period and a burning rate of  $0.82 \text{ mm}^2/\text{s}$  was reported in agreement with the findings of [19].

## *Numerical Studies*

Diesel droplet combustion under the effect of forced convection has been studied numerically by Rajesh et al. [20] for the same conditions used in their experimental work (see *Experimental Studies*) which allowed for direct comparison with their experimental data. The simulation predicted that diesel droplet combustion followed the  $d^2$ -law (Rajesh et al. [20] and Prakash et al. [44]) where the corresponding burning rate was determined. The burning rate was underestimated but followed a similar trend of the experiments which could be accounted for by the lack of appropriate models for radiation and soot, which reportedly was linked to the over predicted flame standoff ratio and the underestimated conductive heat transfer to the droplet from the flame.

The effect of forced convection has been explored experimentally for diesel droplet combustion, the direct effect of varying the flow field around a droplet as opposed to a porous sphere has not been studied, similarly, numerical studies have not directly examined the effect of forced convection (e.g., by varying the flow field), but rather have examined a few specific case studies that deal with the flow conditions associated engine conditions [44].

### **2.2.2. Biodiesel Droplet Combustion**

#### **2.2.2.1. Effect of Ambient Temperature**

##### *Experimental Studies*

The effect of ambient temperature on biodiesel droplet combustion has been studied experimentally with most of the emphasis focusing on ignition delay [15, 39]. Marchese et al. [15] observed biodiesel droplet burning under normal gravity for ambient

temperatures between 1000 K and 1300 K under atmospheric pressure. The ignition delay of biodiesel as well as the neat methyl esters decreased with ambient temperature similarly to what was reported in [39]. Interestingly, the ignition delay decreases with microgravity [15] as well as with the size of the droplet suspension fiber. Microgravity experiments have reported the presence of a heating period prior to combustion (Pan and Chiu [45], where combustion under microgravity (Pan and Chiu) has shown that burning of a biodiesel droplet follows the  $d^2$ -law and produces a spherical flame. The burning rate was dependent on the formation of a soot shell, in a similar manner to what was observed for diesel droplet combustion under microgravity (see *Experimental Studies* in section 2.2.1.1). The production of soot shells may exist for biodiesel droplet combustion under microgravity; however, neat methyl esters such as methyl decanoate (Liu et al. [21]) and methyl butanoate (Farouk et al. [46]) have shown no sign of soot shell formation. Biodiesel droplet flames have standoff ratios observed to increase over the droplet lifetime [21, 46] primarily due to the reduction in the droplet size over time.

### *Numerical Studies*

The effect of ambient temperature on biodiesel droplet combustion has been primarily studied numerically on ignition delay (Marchese et al. [15] and Raslavicius and Bazaras [42]) where numerical work was done in parallel with experiments under normal [15 and 42] and microgravity [15]. During the ignition delay period, the droplet undergoes an apparent heating period similar to what is observed for droplet vaporization in a hot environment where higher ambient temperatures reduce the droplet ignition delay. Subsequently, the flame produced by droplet combustion was found to depend on the size of the supporting.

It can be seen that the effect of ambient temperature on biodiesel droplet combustion has been experimentally examined for ignition delay and to a lesser extent for other parameters under both normal and microgravity conditions where the ambient pressure was only atmospheric. Numerically, biodiesel droplet combustion has been studied for the same conditions as the experimental where the experimental data were used for direct comparison with the numerical results.

#### **2.2.2.2. Effect of Ambient Pressure**

The effect of ambient pressure on biodiesel droplet combustion represents knowledge that can be applied to spray combustion where the ambient pressure in the combustor of an internal combustion engine or gas turbine is well above atmospheric pressure. Unfortunately, there have been no experimental or numerical studies available that address the effect of ambient pressure on biodiesel droplet combustion.

#### **2.2.2.3. Effect of Forced Convection**

##### ***Experimental Studies***

Biodiesel droplet combustion in the presence of forced convection has been studied experimentally using two techniques; namely the porous sphere technique and the free falling droplet in a furnace. The porous sphere experiments were conducted by Raghavan et al. [16] at room conditions by varying the free stream velocity under normal gravity. The mass burning rate for an envelope flame was observed to increase with both laminar free stream velocity and sphere diameter [16] where the free stream mean velocity was varied from 0.4 m/s to 1 m/s and the sphere diameter was varied from 8 mm to 13.6 mm. Similarly, Rajesh et al. [20] reported that the biodiesel burning rate increases

with the free stream velocity ranging from 0.4 to 1.46 m/s using a 16.2 mm diameter porous sphere. The flame standoff distance upstream the sphere of an envelope flame was observed to decrease with the free stream velocity [16]. On the other hand, free falling droplet experiments conducted by Li et al. [18] observed that the droplet first undergoes an initial heating period, followed by combustion where the  $d^2$ -law was followed (Li et al. [18], Botero et al. [19]), allowing for the determination of the burning rate. However, the free falling velocity was not reported. The normalized flame size (i.e., instantaneous flame diameter normalized by the initial droplet diameter) was observed to follow a similar behavior to that of the droplet size. The flame was observed to have a bright yellow colour indicating the presence of soot. Soot collection was found to depend on the flame size.

### ***Numerical Studies***

The effect of forced convection on biodiesel droplet combustion was numerically studied by [44] where the numerical simulations show that the mass burning rate for a biodiesel droplet increases with free stream velocity. This was experimentally verified by [44] to have good agreement where the biodiesel droplet followed the  $d^2$ -law. Similarly, Rajesh et al. [20] numerically simulated the results from their porous sphere experiments (see *Experimental Studies* in this section).

It can be seen that the effect of forced convection on biodiesel droplet combustion has not been experimentally studied by varying the free stream velocity with an individual droplet as opposed to a porous sphere. Numerical results have only been

applied in conjunction with experimental results. Therefore, further work is needed which involves a hot forced convective flow on biodiesel droplet combustion.

### **2.2.3. Biodiesel-Diesel Blended Fuel Droplet Combustion**

#### **2.2.3.1. Effect of Ambient Temperature**

##### *Experimental Studies*

The effect of ambient temperature on biodiesel-diesel blended droplet combustion was experimentally studied by Raslavicius and Bazaras [39] where the ambient temperature ranged from 930 K to 1010 K under atmospheric pressure and normal gravity. The ignition delay of B30 decreases with ambient temperature in a similar manner as the parent fuels where the biodiesel content noticeably increases the ignition delay relative to pure diesel fuel. This was also observed in [47] for a B10 blend under similar ambient conditions where the addition of just 10 percent biodiesel changed the relationship between ignition delay and ambient temperature in comparison to pure diesel fuel. However, the burning rate of the blends was observed by Pan et al. [41] for both normal and microgravity conditions where the burning rate decreased with diesel content under microgravity as opposed to normal gravity where a minimum value occurred for a 50 percent biodiesel blend. The effect of ambient temperature on the blends was not experimentally studied by Pan et al. [41].

##### *Numerical Studies*

The effect of ambient temperature on droplet combustion of biodiesel-diesel blends has only been studied numerically by Raslavicius and Bazaras [42] for a B30 blend with emphasis on the ignition delay. The simulation used ambient temperatures

ranging from 770 K to 870 K at atmospheric pressure under normal gravity. Ignition delay while decreasing with ambient temperature was observed to increase with droplet size, where the significance of droplet size becomes important for lower ambient temperatures.

These studies have shown that the effect of ambient temperature on droplet combustion of biodiesel-diesel blends has only been sparsely examined. Experimentally, the prime focus of the studies has been ignition delay, similarly for numerical studies. The range of ambient temperatures used has been limited to about 100 degrees where the numerical and experimental studies fail to overlap. Also the composition of the blends has also been limited to B10 and B30.

#### **2.2.3.2. Effect of Ambient Pressure**

The effect of ambient pressure on droplet combustion of biodiesel-diesel blends has yet to be studied experimentally nor numerically.

#### **2.2.3.3. Effect of Forced Convection**

##### ***Experimental Studies***

The effect of forced convection on droplet combustion of biodiesel-diesel blends was experimentally studied using the free falling droplet technique (Botero et al. [19]) and the porous sphere technique (Raghavan et al. [16]). Botero et al. [19] found that castor oil biodiesel reduced the burning rate of the blends. Raghavan et al. (using porous sphere method) observed that the burning rate of an envelope flame increases with laminar free stream velocity for blends of B60, B70, B80 and B90 where no definitive trend was found between blend composition and the burning rate. All of the blends used

by Raghavan et al. [16] transition from an envelope flame to a wake flame for a free stream velocity range of 0.4 m/s to 1.0 m/s where the transition velocity decreased with diesel content.

### ***Numerical Studies***

The only numerical study dealing with forced convection effects on droplet combustion of biodiesel-diesel blends was done by Prakash et al. [44]. The combustion was simulated under room conditions where the free stream velocity was constant at 42 m/s. Blends B20, B40, B60 and B80 were found to not follow the  $d^2$ -law, instead 3 modes of burning were found, the first mirror diesel fuel, the second was a combination of the two fuels and the last mode mirrored biodiesel behavior. The explicit effect of forced convection was not investigated but rather the focus of the study was on the compositional effects.

The previously mentioned studies have shown that the effect of forced convection has not been directly studied for droplet combustion of biodiesel-diesel blends, whereas the majority of the focus has been on the effect of droplet composition on the combustion of these blends.

#### **2.2.4. Conclusions**

In summary, diesel droplet combustion has been studied experimentally under normal and microgravity conditions at elevated ambient temperature at atmospheric pressure, while numerical studies have mirrored the experimental test conditions. Similarly, biodiesel droplet combustion has been studied under similar ambient conditions in which the experimental and numerical studies focused on the same test

conditions. In contrast to their parent fuels, biodiesel-diesel blends have had dissimilar ambient temperatures used for their experimental and numerical studies, respectively. A common theme is the non-existence of studies dealing with droplet combustion under elevated ambient pressure for all of these fuel droplets, except for one study dealing with diesel droplet fragmentation. Droplet combustion of diesel, biodiesel or their blends has not been examined under forced convection at elevated pressure. A summary of droplet combustion of diesel, biodiesel and their blends is given in Table **2.2**.

**Table 2.2.** Summary of literature on droplet combustion of diesel, biodiesel and their blends.

Ref.	Fuel Type	Ambient Conditions ( $P_{\infty}$ , $T_{\infty}$ )	Flow Conditions	Droplet Suspension Technique (Diameter)	Initial Droplet Diameter [mm]	Study
[14]	B0 (Diesel)	901-1268 K; 1 bar	Free convection	Single fiber* (0.1-0.2 mm)	0.70-1.70	Exp.
[15]	B100 (Methyl decanoate)	Normal and microgravity; 1050-1300 K; 1 bar	Free convection	Cross fiber** (14 $\mu$ m)	1.00-1.30	Exp.
[16]	B60, B70 ,B80 ,B90 and B100 (Karanja oil)	298 K; 1 bar	Laminar flow (0.40-1.00 m/s)	Porous sphere (8.0-13.6 mm)	N/a	Exp.
[17]	B0	298 K; 1 bar	Laminar flow (0.40-1.00 m/s)	Porous sphere (8.0-13.6 mm)	N/a	Exp.
[18]	B0 and B100 (Waste vegetable oil)	980-1040 K; 1 bar	Laminar flow (N/a)	Free falling droplet	0.23-0.25	Exp.
[19]	B0 and B100 (Castor oil)	980-1040 K; 1 bar	Laminar flow (N/a)	Free falling droplet	0.23-0.25	Exp.
[20]	B0 and B100 (Jatropha oil)	298 K; 1 bar	Laminar flow (0.40-2.00 m/s)	Porous sphere (16.2 mm)	N/a	Exp. and Num.
[21]	B100 (Methyl decanoate)	Microgravity; 298 K; 1 bar	Free convection	Cross fiber** (14 $\mu$ m)	0.53-0.57	Exp. and Num.
[39]	B0, B30 and B100 (Rapeseed oil)	930-1010 K; 1 bar	Free convection	Single fiber* (N/a)	0.95-1.05	Exp.
[40]	B0	800-1268 K; 1 bar	Free convection	Single fiber* (0.1 mm)	0.98-1.42	Exp.
[41]	B0, B25, B50, B75 and B100 (N/a)	Normal and microgravity; 298 K; 1 bar	Free convection	Cross fiber** (7 $\mu$ m)	0.45 and 0.53	Exp.
[42]	B0, B30 and B100 (Rapeseed oil)	770-870 K; 1 bar	Free convection	N/a	0.10-0.20	Num.
[44]	B0, B20, B40, B60, B80 and B100 (Jatropha and karanja oil)	298 K; 1 bar	Laminar flow (0.44-0.82 m/s)	Porous sphere (8-10 mm)	8.00-10.00	Exp. and Num.
[45]	B0, B50 and B100 (Waste vegetable oil)	Microgravity; 298 K; 1 bar	Free convection	Cross fiber** (2.5 $\mu$ m)	0.46 and 0.53	Exp.
[46]	B100 (Methyl butanoate)	Microgravity; 298 K; 1 bar	Free convection	Cross Fiber** (14 $\mu$ m)	0.53-0.55	Exp. and Num.
[47]	B0, B10 and B100 (Rapeseed oil)	860-1005 K; 1 bar	Free convection	Single fiber* (0.8 mm)	2.24-2.26	Exp.

\*Quartz fiber. \*\*Silicon carbide fibers.

## **Chapter 3 - Experimental Apparatus and Test Conditions**

### **3.1. Experimental Apparatus**

The experimental apparatus will be discussed in this section; however, certain aspects of the experimental apparatus will only be mentioned in brevity as the majority of the details can be found in [48].

#### **3.1.1. Introduction**

The experimental apparatus used in this experimental work is a test rig that was designed to produce isotropic and homogeneous turbulence, while being capable of operating under elevated ambient pressure and temperature [48]. The ability to vary the ambient conditions allows for variation of the turbulent Reynolds number as well as the turbulent length and time scales. The majority of the details concerning this experimental apparatus can be found in [48], whereas this section will only briefly describe the experimental setup and highlight in detail the upgrades.

#### **3.1.2. Spherical Turbulence Chamber**

The test rig is a spherical vessel made of stainless steel with inner and outer diameters of 380 and 405 mm, respectively. The volume of the chamber is 28.73 litres. Figure 3.1 shows the spherical chamber with a number of flanges welded onto the original sphere. Details about the spacing and exact locations of the flanges can be found in [48]. The 4-inch viewing ports were covered with quartz windows [48] which made it possible to contain the high temperature and pressure environment while maintaining a high quality optical view into the chamber. The 5-inch viewing ports were used for two purposes: to mount the heating system plates (see heating system section) and to provide

additional viewing using quartz windows in order to conduct flow field measurements using Laser Doppler Velocimetry (2D-LDV) as well as Particle Image Velocimetry (PIV). The 4.5-inch fan mounting flanges were used to mount each of the 8 fans with their motors. The smaller 10 accessory ports (includes sensor ports in Figure 3.1) were used for different purposes. They can be grouped as top sensor ports, side accessory ports and one bottom accessory port. The top center port was used to mount a fiber hold for droplet experiments, where the four adjacent top ports were used to mount a pressure gauge (see Appendix A for details), a pressure transducer, a mechanical pressure release valve and the remaining port was sealed with a plumbing plug. The mechanical pressure release valve only actuates if the pressure inside of the chamber exceeds the safe operational limit of 300 psig. The release pressure can be adjusted via a screw. There are 4 side accessory ports, where one port was used to mount a supply line for compressed air and nitrogen, another port was used for the droplet injector/ignition system and the final two ports were each used to mount a thermocouple (see Appendix A for details) for each respective heating system plate. The bottom accessory port was used for evacuating gases from the chamber.

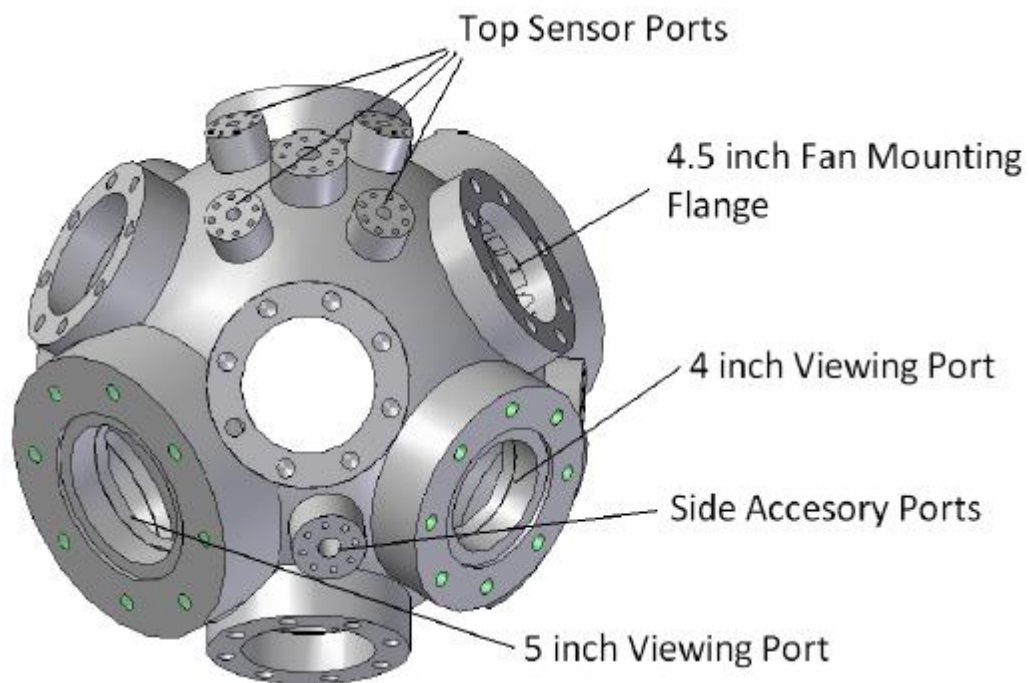


**Figure 3.1.** Schematic diagram of the spherical chamber with flanges arrangement [48].

### 3.1.3. Sealing Surfaces

The spherical chamber's numerous flanges represent a large number of sealing surfaces, which must be properly sealed to maintain the set ambient pressure and hence prevent gases leakage. There are 3 types of seals which were tried; gasket seals, o-ring seals (both static and dynamic) and shaft seals.

Gasket seals were used for the quartz windows which were originally sealed using Teflon gaskets; however their exposure to the elevated ambient temperature caused these gaskets to deform extensively due the elevated ambient pressure inside the chamber and consequently failed. The graphite gaskets did not deform like the Teflon gaskets, however, the graphite gaskets would adhere to the quartz window as well as the chamber outer wall due to elevated gas temperature. Finally, the material NA60 (see Appendix B)

was selected. It has a thickness of 1/16 inches to minimize the amount of force acting on the gasket's cross-sectional area. Just to mention that only the quartz windows were sealed with this material (gaskets) whereas the rest of the flanges were sealed using o-rings.

The majority of the o-ring seals were static seals, with one exception being the droplet injector/ignition system which used a dynamic seal [48]. All of the o-ring seals with the exception of the heating system plates were made of Viton (a registered trademark of DuPont Performance Elastomers L.L.C. – see Appendix B), while the o-rings chosen for the heating system plates were made of silicon because of the proximity to the heating elements which then requires an o-ring with a higher temperature rating (see Appendix B).

The shaft seals were used for the fan shafts to prevent leakage from the chamber; these seals were made of poly-amide filled Teflon (see material specs/properties and manufacturer's contact info – see Appendix B). The seals were designed with a 3 lip sealing surface in order to prolong the lifespan of the seals. The seals were designed by Sean Fabbro [48] and manufactured in house, where the majority of the specifications and the manufacturing process details can be found in [48]. There are dimensional differences between the current seals and the seal dimensions reported by Fabbro [48] where the exact dimensions of the current seals can be found in Appendix B. Figure 3.2 identifies the seal face which should be facing towards the outside of the chamber, while the rest of the seal including the seal o-ring groove slides into a machined port in the fan flange. Figure 3.2 shows the appearance of the seal lips after being manufactured where the face of each lip is parallel to the seal face. In order to produce an effective sealing

surface against the fan transmission shaft, the face of each seal lip must be deformed prior to installation.

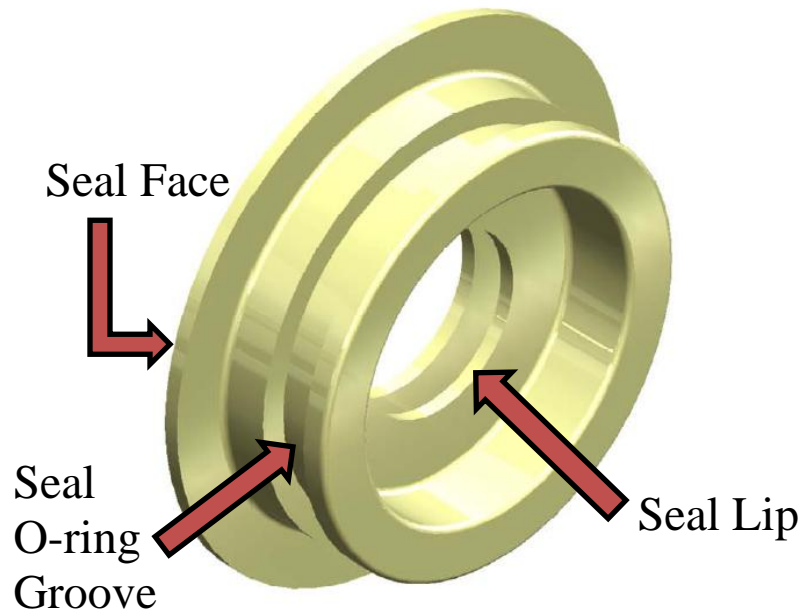


**Figure 3.2.** Fan shaft seal with key features labeled [48].

The deformation of seal lips (as shown in Figure 3.3) was accomplished using a seal forming tool which consists an aluminum shaft with a conical end that slides through the seal (in the direction shown by the blue arrow in Figure 3.3) in order to deform the seal lips. The deformed seal lips will eventually form a high pressure seal against the running surface of the fan transmission shaft [48] by sliding a portion of the fan shaft through the seal lips. Only the hardened middle section of the fan transmission shaft slides through the seal because that section of the shaft has a very smooth surface finish in order to prevent damage to the relatively softer seal material (see seal material properties in Appendix B). Figure 3.4 shows the seal before deformation and after deformation where the deformed seal lips protrude towards the inside of the chamber. Once the seal and the

fan transmission shaft have been fully installed, their mated surfaces require that the fan shaft be rotated at a relatively high (at least 2000 RPM) speed while the chamber is pressurized to complete the forming process of the seal and ensure minimal leakage.

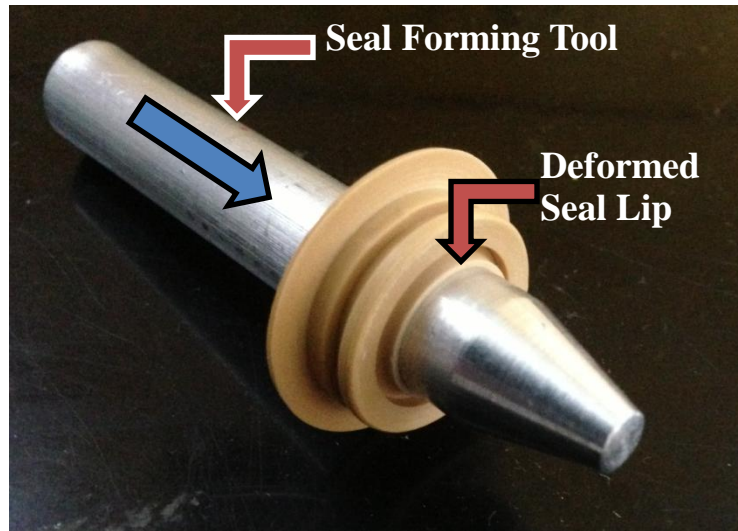


**Figure 3.3.** Seal deformation prior to installation.

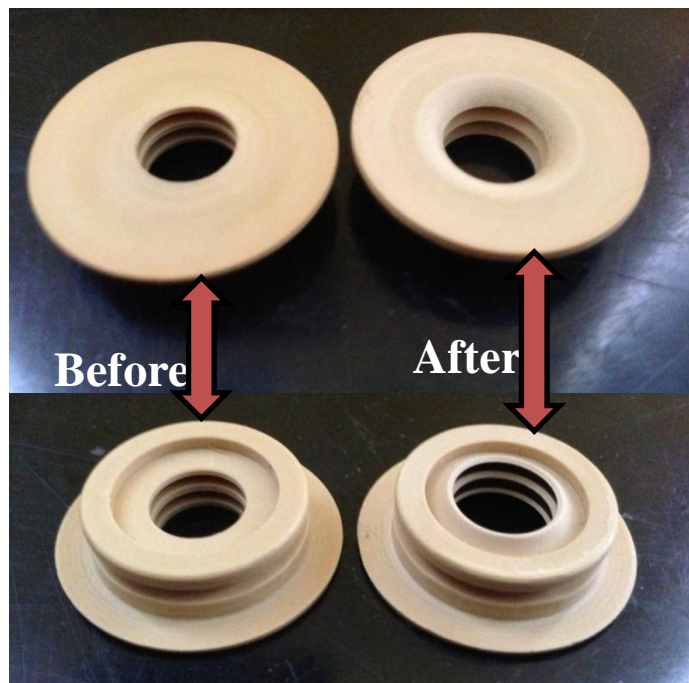


**Figure 3.4.** Fan shaft seal before and after deformation.

### **3.1.4. Turbulence Generation and Fan Design**

Turbulent flow is generated by 4 pairs of axial opposed fans. Each of the six bladed axial fans is located 200 mm face to face from the opposing fan. These fans are each driven by a servomotor connected via a fan transmission assembly. Each servomotor is synchronized by manual adjustment of the servomotor drive's amplifier, where the synchronization of all the eight fans is within  $\pm 5$  revolutions per minute (RPM). Further details regarding the servomotors, the servomotor drives, their control system using LabView and the fan blade design were reported in [48].

#### **3.1.4.1. Fan Transmission Assembly**

Detailed description of the fan transmission assembly can be found in [48]; however, there are some minor modifications which were incorporated in the existing fan transmission assembly reported in [48]. There are two main modifications which concern changes to the alignment bearings and the key connection between the stainless steel section and the hardened steel middle section of the fan transmission shaft (see Figure 3.5). The alignment bearings required having their lubricating grease changed to a higher temperature lubricant rated for 316 °C (see Appendix C). The connection between the two previously mentioned shaft sections, as shown in Figure 3.5, was made by using a separate piece made of steel that sits inside of a hole inside of the both shaft sections, as opposed to the previously used method of having the connection piece built as part of the stainless steel shaft section [48]. Figure 3.5 shows the fan transmission assembly in an exploded view with the shaft key connector as a separate component. The shaft key connector is made of mild carbon steel in order to minimize damage to the holes of both respective shafts.

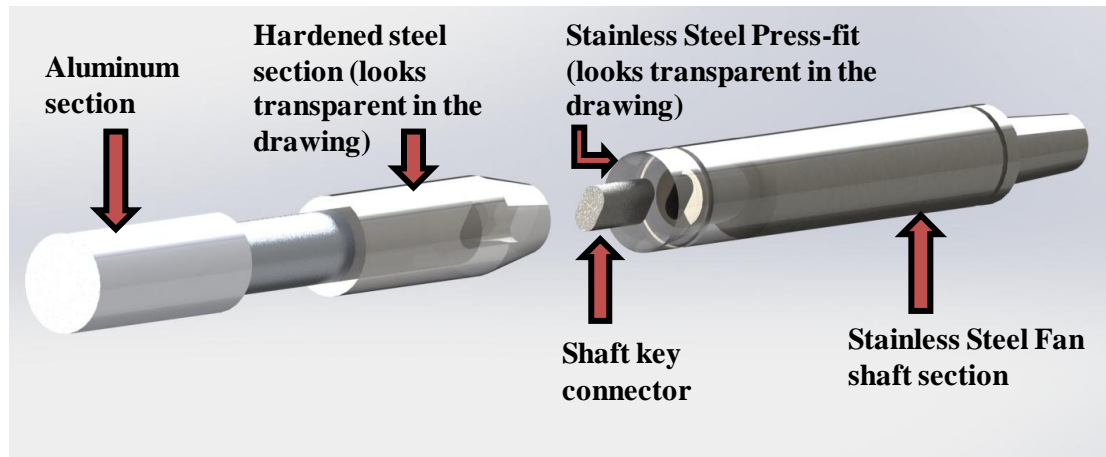


**Figure 3.5.** Fan transmission shaft assembly [48].

### 3.1.5. Heating System

The experimental apparatus required the ability to elevate and control the ambient temperature of the gas inside of the spherical chamber. The original heating system designed and developed in [48] was found to have a fundamental flaw regarding the connections between the individual heating plates, where it was discovered that the nickel chromium wire could not be soldered together. This required design and development of a new heating system in order to produce an elevated ambient temperature within the chamber.

#### 3.1.5.1. Heating Plate Design

An idea was put forth to use the 5 inch window ports to contain heating elements where these elements were determined through consultation with an application engineer from Omega Engineering Inc., to be tubular heating elements due to the necessity of keeping the electrical connections outside of the chamber.

The first heating plate was designed to have heating elements bent in such a way that they did not protrude beyond periphery of the fan blades in order to minimize interaction with the flow field and formation of turbulent structures. The heating elements were individually spaced approximately 1 inch apart from one another to minimize the possibility of the elements overheating and burning out. Figure 3.6 shows the first heating plate fully assembled where the individual elements were installed in a circular steel plate with each element was bent in a similar manner to an oven element (see Appendix D). However due to space constriction of the chamber's 5 inch opening, the bottom and upper heating elements had to be bent with an additional curvature that would fit inside of the opening (see Appendix D). Each heating element is 0.246 inches in diameter and has a total length of 18 inches with a power output of 255 W. The heating elements were designed by the manufacturer to be powered from a 110 volt electrical outlet.

A second heating plate was developed to make up for the deficiencies (see Heating Test section) of the first heating plate by focusing on more power. However, due to dimensional constraints posed by the 5 inch opening, it was determined that the largest heating elements that could fit were tubular heating elements with 0.375 inch diameter (see Appendix D). A similar design to the first heating plate was used; that is 3 heating elements bent in the same manner as the first heating plate with the same spacing between each respective heating element. The manufacturer, Etirex, custom made the length of these elements and bent them to our specifications (see Appendix D), where each element was found to have 450 W of power and designed to operate using 110 volt electricity. Figure 3.7 shows the fully assembled second heating plate.



**Figure 3.6.** First heating plate.



**Figure 3.7.** Second heating plate.

### 3.1.5.2. Heating Control System

The control system consists of a programmable digital controller with a single input for a thermocouple, a solid state relay, a finned heat sink, thermally conductive paste, a thermocouple, a power cord, 2 switches and a pilot light. All of these components were assembled inside of a CSA certified electrical box that contains all exposed electrical connections. Additionally, a second electrical box was mounted onto the flange of the 5-inch port opening to cover the exposed electrical terminals from the heating elements as shown in Figure 3.5. Electrical power is transferred from the heating system controller through a flexible plastic conduit to the second electrical box, where a ground wire ensures that the experimental setup does not become accidentally energized. Figure 3.8 shows the electrical box covering the heating element terminals.



**Figure 3.8.** Electrical box covering the heating element electrical terminals.

Figure 3.9 shows the heating system controller. It shows the main power switch that controls the power coming into the box - where a pilot light (if illuminated) shows

that power is being supplied to the box. The controller itself shows the temperature measured by the thermocouple with a red digital display, and the set point for the controller is shown with a green digital display. Adjustment of the set point (i.e., the desired operating temperature for the experiment) can be easily done by pressing the up or down arrow buttons located on the controller. Once the controller detects that the current temperature measurement is below the set point, a 5 volt signal is sent to the solid state relay, where the relay transfers power to the heating elements; however, in between the heating elements and the relay is an illuminated switch that can control whether or not power is transmitted to the heating elements. The illuminated switch was added as a safety precaution to prevent power from being directly transferred to the heating elements if the controller was ever turned off with the set point above room temperature.

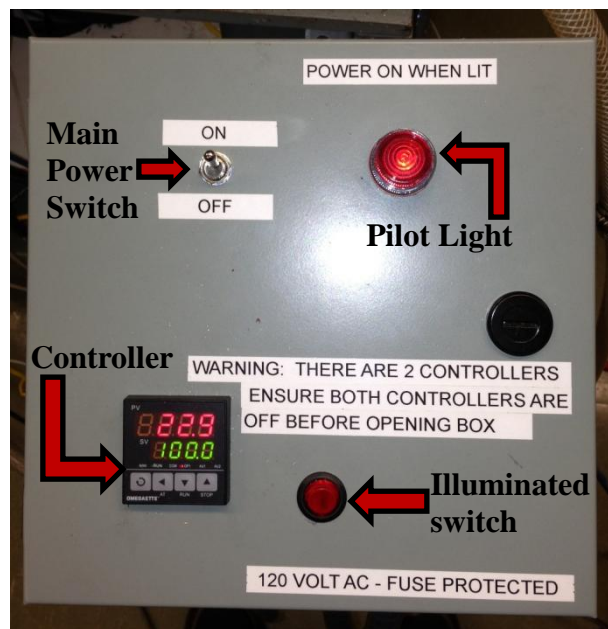


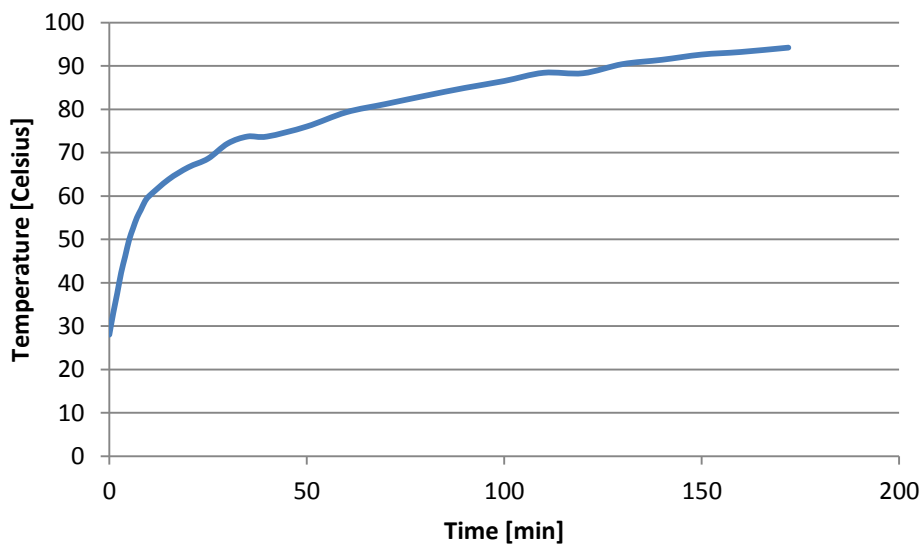
**Figure 3.9.** Heating system controller.

A heating system controller is needed for each heating plate due to the required power consumption for the two heating plates being approximately 2115 W with the

approximate amount of electrical current needed is 19.2 amps from a 110 volt electrical outlet. Using two electrical boxes/controllers was determined to be the most cost effective choice, rather than having an electrical contractor install a 30 amp dedicated power supply line to the experiment.

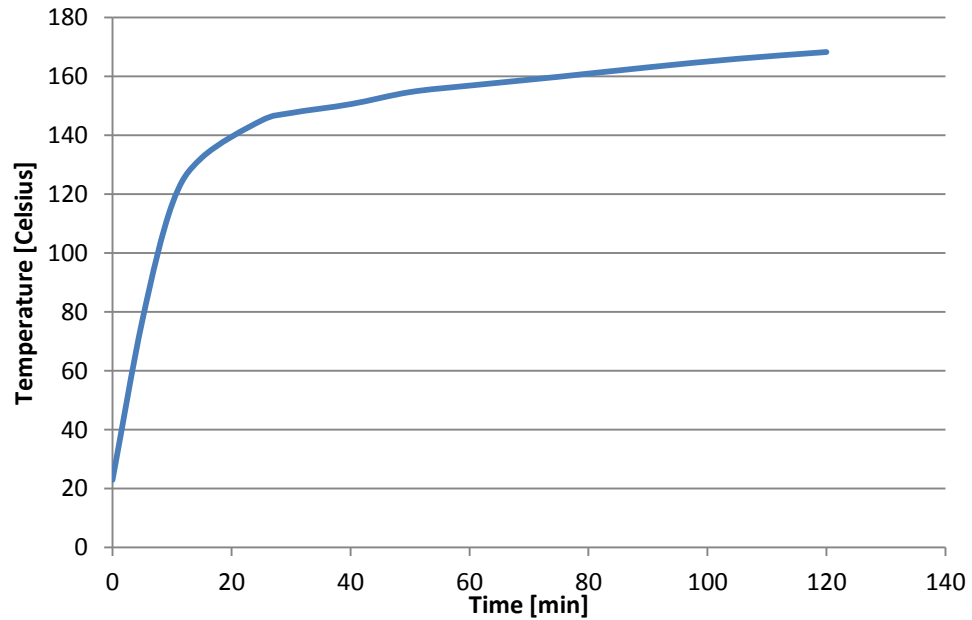
### 3.1.5.3. Heating System Tests

Tests were conducted under atmospheric pressure using low fan speeds (500 RPM) in order to mix the air while minimizing convective heat loss through the chamber walls. Figure 3.10 shows the test results of the first heating system (shown in Figure 3.6) with no insulation inside of the chamber. It shows that the maximum temperature that was reached after 2.5 hours was approximately 95°C. This temperature was too low to evaporate biodiesel; therefore the addition of insulation (see Chamber Insulation section for details) inside of the chamber along the wall was installed in order to minimize heat loss.



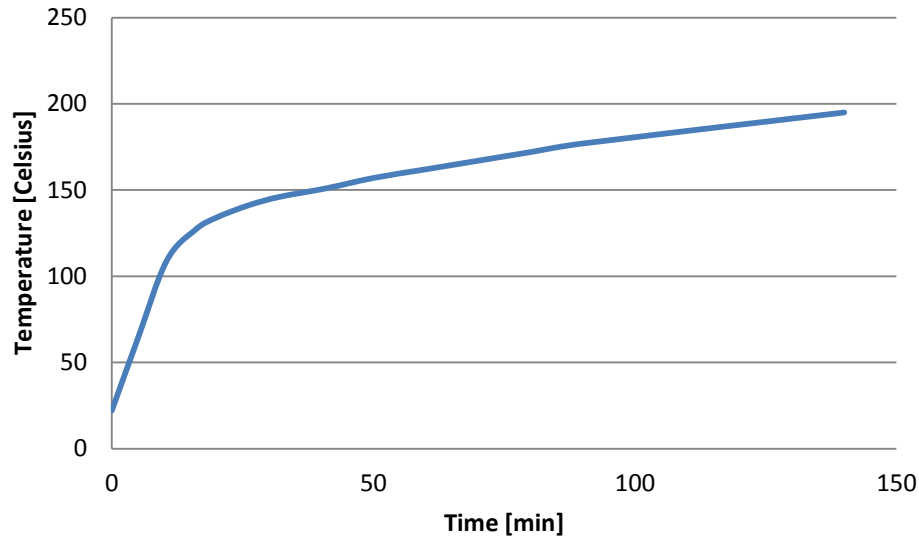
**Figure 3.10.** Chamber heating test with first plate and no insulation.

Figure 3.11 shows the test results of the second heating system (shown in Figure 3.7) with the inside of the chamber being insulated where a maximum ambient temperature of over 160 °C achieved in 2 hours.



**Figure 3.11.** Chamber heating test with first plate and internal insulation.

Figure 3.12 shows that running the two heating plates at the same time significantly shortened the time needed to reach; for example 150 °C in only 40 minutes. The maximum temperature reached was 195 °C in 2.3 hours.



**Figure 3.12.** Heat test with both heating plates and insulation of the inside of the chamber.

In order to shorten the heat up time for the experiment, insulation (see Chamber Insulation section) and heating tape [48] were added externally to the chamber outside, where the heating tape was wrapped around the outside wall of the chamber and the insulation was placed onto the heating tape. These two additions provided a significant reduction in the heating time as it only took 25 minutes to reach a temperature of 200 °C.

#### **3.1.5.4. Chamber Insulation**

The aforementioned tests revealed that the chamber walls as well as the quartz windows represent a massive heat sink. Therefore insulation made of alumina-silica fibers with a thickness of 0.125 inches was placed along the inside wall of the chamber with the insulation kept in place by using a high temperature silicone adhesive. Insulation was also placed onto the inside face (between the heating elements and the steel plate) of the heating plates to further aid in minimizing heat loss as shown in Figure 3.13. Tests revealed that insulation behind the fans was susceptible to rip apart at high rotational

speeds (high levels of turbulence) under elevated ambient pressure. Therefore no insulation behind the fans was used.



**Figure 3.13.** Insulation of the inner chamber wall.

Insulation of the outside surface/walls of the chamber was performed via using a blanket made from alumina-silica fibers with a 1 inch thickness. The external insulation was cut into rectangular shapes that fit in between the various flanges of the chamber as well as on top of the accessory ports with two layers of the insulation were installed over all accessible areas to further reduce heat loss (see Figure 3.14). Additionally, the flange faces for each of the viewing ports had a layer of the 0.125 inch thick insulation attached to the surface using a high temperature silicone.

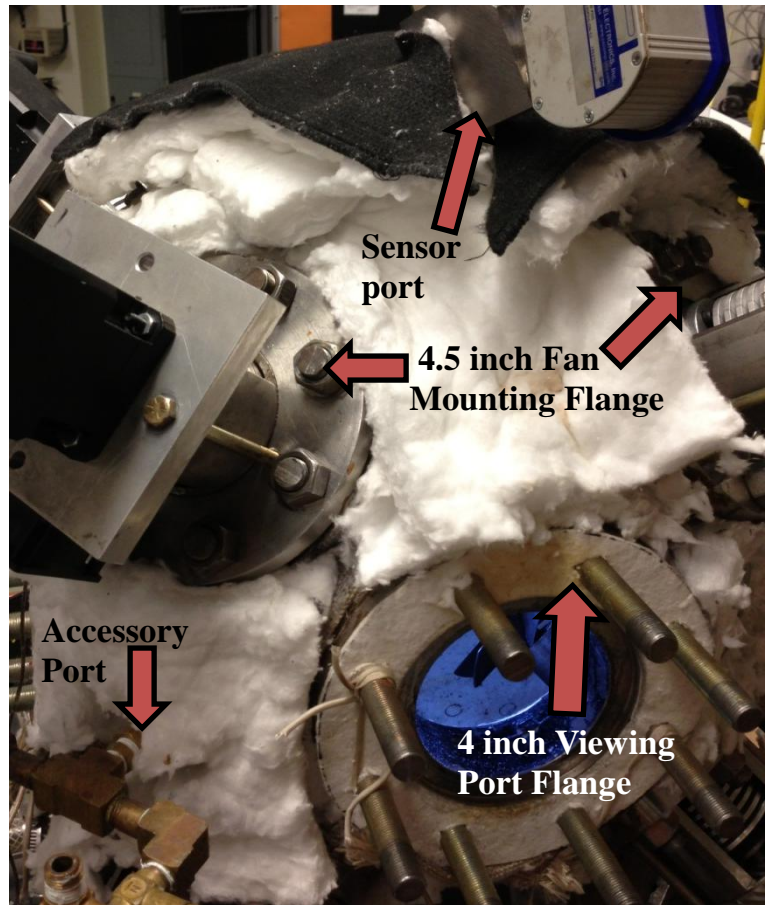


**Figure 3.14.** Outside view of chamber with external insulation.

### **3.1.6. Droplet Suspension**

The droplet suspension in the center of the chamber was achieved by vertically suspending a quartz fiber filament with a stem diameter of approximately 150 to 290  $\mu\text{m}$  with a 400 to 500  $\mu\text{m}$  spherical nodule/sphere at its to support the droplet. Further details regarding the quartz fiber support system can be found in [48].

### 3.1.7. Droplet Injection/Ignition System

The details regarding the droplet injection system for this experimental apparatus can be found in [48]. This section reports detailed description of the droplet ignition system which was initiated by Fabbro [48].

#### 3.1.7.1. Ignition Wire

The droplet igniter described in [48] recommends the use of a straight piece of resistance wire (i.e., heating wire) to heat and subsequently ignites the droplet fuel vapour. However, preliminary experimentation found that by coiling the resistance wire, the local temperature around the coil remains hotter in the presence of a convective flow in comparison to a straight piece of wire. Figure 3.15 shows the wire element ignition head with a coiled piece of 28 gauge resistance wire made of Kanthal APM (iron-chromium-aluminium alloy made by Kanthal, a brand of the Sandvik Group). The coiled piece of wire also allowed for a greater length of resistance wire to be used which in turn provided additional electrical resistance in order to not draw an excessive amount of electrical current.

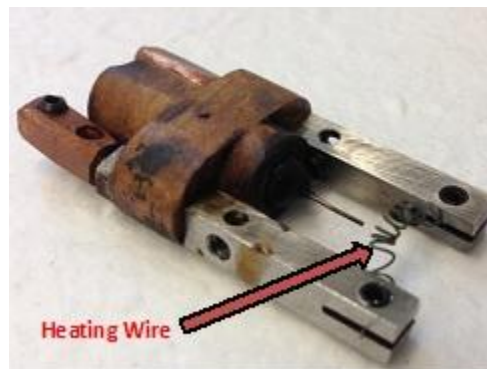


**Figure 3.15.** Wire element ignition head [48].

### 3.1.7.2. Ignition Power Source

The igniter's heating element was originally planned to be used in conjunction with a direct current power supply that would supply a constant voltage, however, initial testing revealed that the lack of control over the applied voltage limited the range of ambient conditions that the ignition element would successfully ignite decane droplet. The igniter requires a relatively low amount of voltage (between 12 and 30 volts), while being able to draw a relatively large amount of electrical current (between 4 to 10 amps), this is dependent on the convective heat transfer from the igniter to the ambient air inside of the chamber, which is directly related to the Reynolds number of the flow (i.e., the rotational speed of the fans and ambient pressure). Therefore, it was determined that control of the applied voltage should be adopted, which could be accomplished by drawing power from a variable autotransformer (i.e., variac) and a 30 volt transformer. Power from the transformer is then transferred through 18 gauge stranded wires which were run through the inside of the injector outer tube as shown in Figure **3.16**. Further details regarding the individual components of the ignition system can be found in Appendix E.

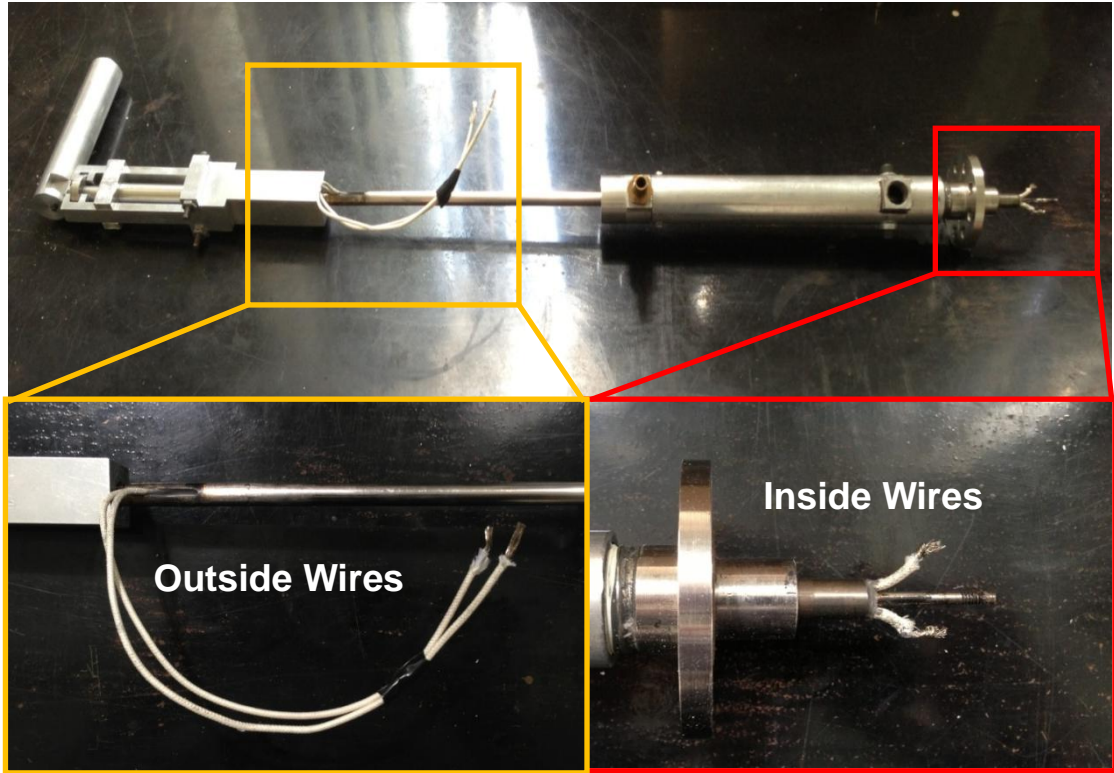


**Figure 3.16.** Droplet injector with electrical wires for ignition system [48].

### 3.1.8. Image Capture Setup and Procedure

Details concerning the image capturing setup and procedure can be found in [48]; however, further complementary information is described here. For instance, the light source used to backlight the suspended droplet was changed from an LED array to a 250 W halogen lamp. The halogen lamp was used to provide a more intense light background, which in turn helped to optimize the contrast of the droplet with respect to the rest of the image background. The one negative aspect of the halogen lamp is in regard to the amount of heat it gives off, which was found to affect the droplet evaporation if the proximity of the lamp to the quartz was too close. Experimental testing found that if the halogen lamp was placed at least one meter away from the quartz window, then the heat transfer to the droplet would be negligible. Thus, a circular galvanized section of a duct

with an inner diameter of 4 inches and a length of 5 feet was used. This duct was found to act as spacer between the lamp and the window, and also to focus the light rays of the lamp toward the window. The inside of the duct was spray painted white with high temperature barbeque paint to help reflect the light towards the window.

### **3.1.9. Image Processing**

An in-house image processing code was developed to determine the droplet size by analyzing images of the project surface area of a droplet with a contrasting background. The method uses a calibration image of a ruler in place of where the fiber normally resides, which is subsequently printed and measured on paper using a ruler. This uses edge detection in combination with closure conditions for the upper and lower edges of the droplet. Further details regarding the calculation of the droplet surface area along with the Matlab code can be found in Appendix F.

## **3.2. Test Conditions**

In order to successfully conduct droplet evaporation of biodiesel, diesel and their blends, an ambient temperature above the flash point of both fuels was needed, where the minimum flash points of these fuels were at least 50°C and 140°C [25,49], respectively. The experimental setup was used to conduct preliminary testing using an ambient temperature of 150°C. The results from those tests had shown that biodiesel appeared to have a linear surface regression profile in agreement with the  $d^2$ -law, however, diesel fuel was found to have an extremely non-linear surface regression profile. The experimental setup was found to have a maximum sustainable ambient temperature of 200°C, this temperature was limited by the seal materials used on the experimental setup.

Droplet vaporization experiments were conducted using the highest available ambient temperature (200°C) in order to approach conditions in a gas turbine engine. Ambient pressure was varied from atmospheric pressure up to 16 bar, where 16 bar was the highest ambient pressure used due to limitations encountered with the gasket material that seals the quartz windows. The rotational speed of the fans was varied in 500 RPM increments from 0 RPM up to the highest speed that a droplet could remain on the fiber.

Combustion experiments were conducted using an ambient temperature of 150°C, which exceeds the minimum flash point for both parent fuels, where ignition was caused by a heating element. Ambient pressure and the rotational speeds test conditions were varied in the same manner as for the droplet vaporization experiments.

## Chapter 4 - Results and Discussion: Droplet Vaporization

### 4.1. Turbulence Characterization

Turbulence characterization at elevated ambient pressure and room temperature was reported in [48, 50]. The results revealed that turbulence is homogeneous and isotropic in the central spherical volume of the vessel with an approximate diameter of 40 mm. However, additional testing was performed at ambient temperature up to 100°C and the results are presented here.

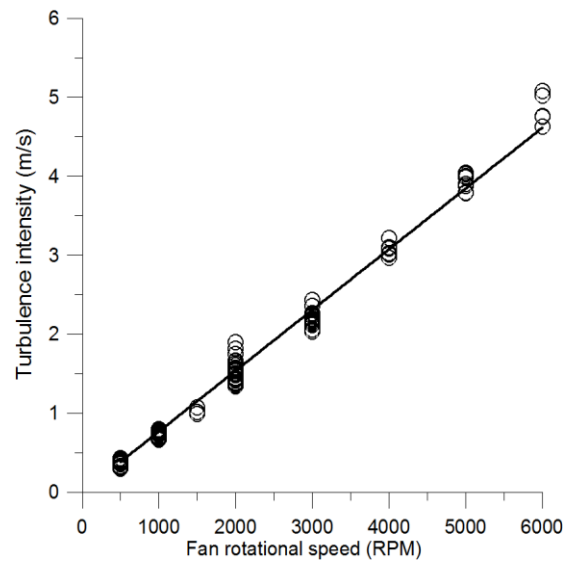


**Figure 4.1.** Variation of turbulence intensity with rotational speed of fans.

Figure 4.1 presents the turbulence intensity as a function of the fans rotational speed in the central volume of the chamber (with a diameter of 40 mm). This figure revealed that the relationship between turbulence intensity and the fans rotational speed remains linear (as at room temperature [48,50]) and appears unaffected by the variation in the ambient temperature. This relationship was found to be  $q^{0.5}$  (m/s) = 0.00077N (RPM), where N is the fan rotational speed [50]. Figure 4.2 shows that increasing the air/ambient

temperature up to 100°C does not significantly affect the isotropy of turbulence. This figure shows that the level of turbulence isotropy remains similar to that at room temperature as reported in [48,50].

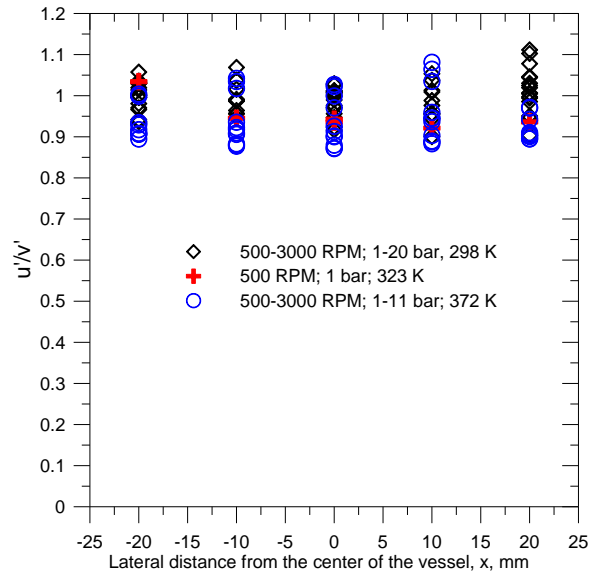
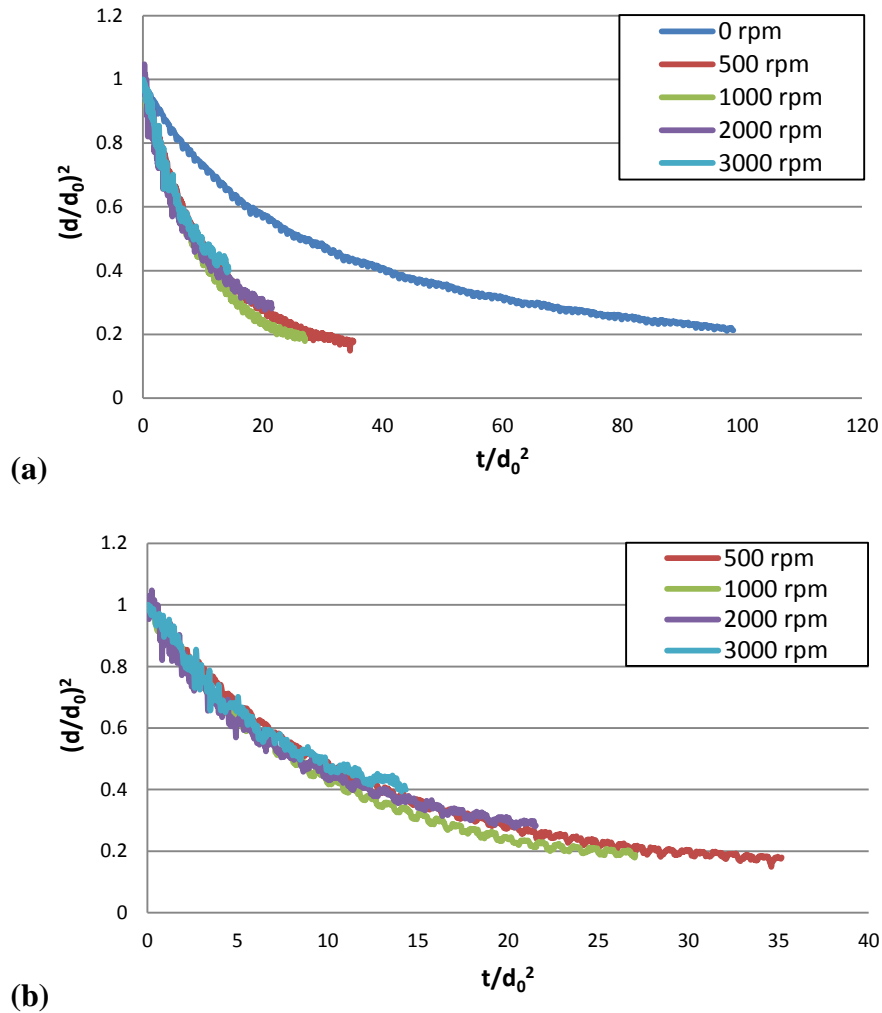


**Figure 4.2.** Variation of  $u'/v'$  along the radial distance from the center of the vessel for various fans speed at different ambient pressures and temperatures.

## 4.2. Droplet Vaporization

This section presents the results of the vaporization process of diesel, biodiesel and their blends under turbulent flow conditions at elevated pressure and temperature conditions.

### 4.2.1. Diesel Droplet



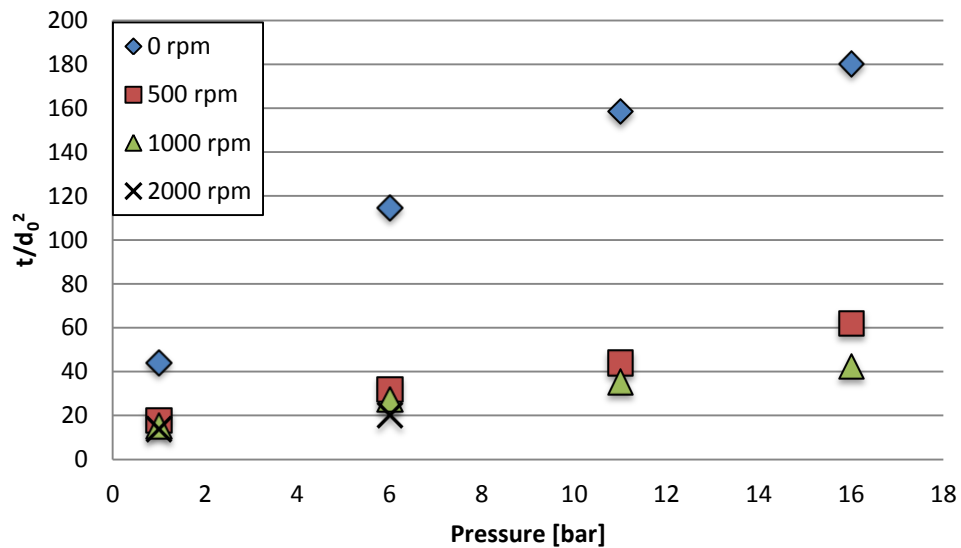
**Figure 4.3.** Time history of the squared normalized diameter for different fans speeds at  $T_{amb} = 473K$  and  $P_{amb} = 6$  bar for diesel droplet comparing evaporation at (a) free convection and forced convection and (b) forced convection.

Figure 4.3 (a) and Figure 4.3 (b) show the temporal variation of the projected surface area for diesel (B0) droplet evaporation for different fan speeds at ambient temperature and pressure of 473 K and 6 bar, respectively. Three main observations can be taken from Figure 4.3 (a) and Figure 4.3 (b). Firstly, the non-linear change in the projected surface area of the diesel droplet reveals that the diesel fuel droplet does not follow the classical  $d^2$ -law. Diesel fuel used in these experiments has a chemical

composition approximated as hydrocarbons ranging from C10 to C22, which shows the multicomponent behavior of the fuel, where diesel fuel has a boiling point ranging between 423-603 K. The relatively low ambient temperature of 473 K used in this experimental work does not provide enough of a reduction in the enthalpy of vaporization for the mid-range and heavier components that comprise diesel fuel to vaporize at the same rate as the lighter components. Secondly, the presence of two types of oscillations in the surface regression profile. The observed higher frequency oscillations are caused by the threshold value used in the image processing code which is affected by the variations in the image intensity caused by the light source used to back light the droplet. The lower frequency oscillations only occur at fan speeds of 500 RPM and greater where the suspended droplet begins to move in all directions while still suspended onto the quartz fiber. The droplet motion has been captured by the high speed camera where the droplet movement was observed to increase with fan speed. The droplet movement intensified at higher fan speeds where the addition of elevated ambient pressure limited the initial droplet size that can be held onto the fiber because of the high turbulence intensity. The droplet movement onto the fiber is believed to result from interactions between the turbulent structures and the droplet. Thirdly, the reduction of diesel droplet lifetime by transitioning from free to forced convection is evident in Figure 4.3 (a) where the droplet lifetime of the 500 RPM case is 72 percent shorter than the free convection case. Further increases in fan speed to 1000 RPM and higher lead to shorter droplet lifetimes. However, these decreases are minor in comparison to the 0 RPM with the 500 RPM transition. The percent difference with respect to the free convection case for each of the different fan speeds can be found in Table 4.1.

**Table 4.1.** Diesel droplet lifetime at 6 bar and 473 K.

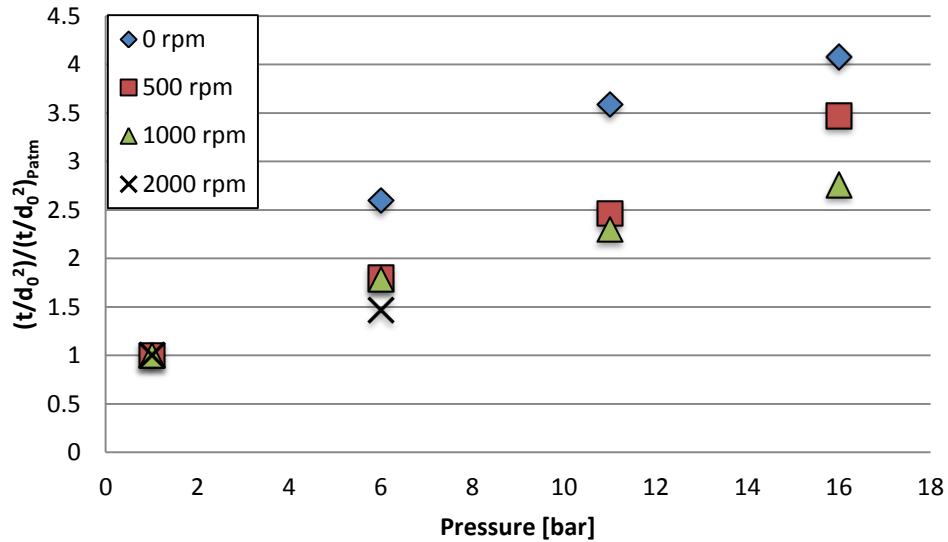
Fan Speed [RPM]	Lifetime ( $t/d_0^2$ ) [sec/mm <sup>2</sup> ]	% Difference with 0 RPM
0	114.7175	0.00%
500	32.06504	-72.05%
1000	27.29911	-76.20%
2000	20.23952	-82.36%
3000	11.30097	-90.15%



**Figure 4.4.** Diesel droplet lifetime as a function of ambient pressure for given fans speed at  $T_{amb} = 473$  K.

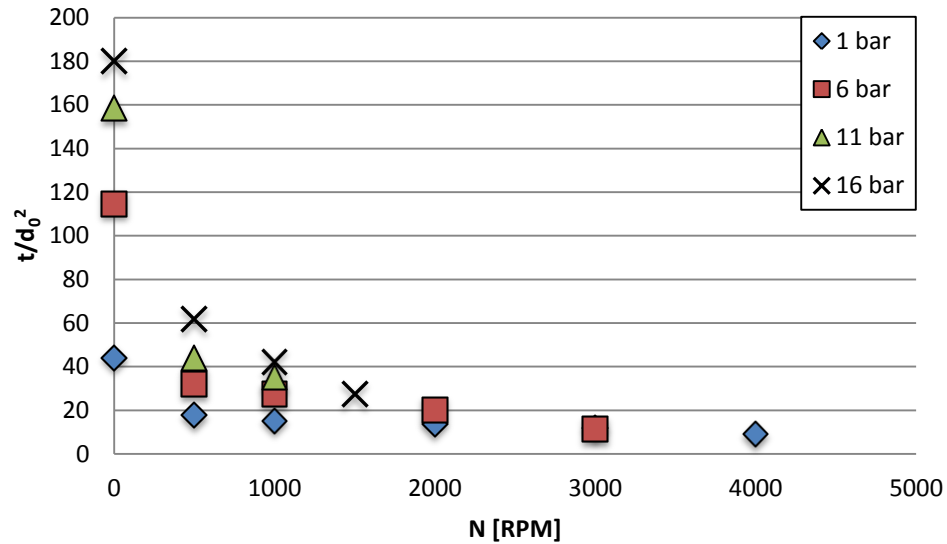
Figure 4.4 presents the diesel droplet lifetime as a function of ambient pressure for different fan speeds at an ambient temperature of 473 K. The evaporation of diesel fuel droplet under these ambient conditions have shown that, for a given ambient pressure and temperature, the lifetime of a diesel droplet decreases with turbulence intensity where ambient pressure enhances the relative effect of flow turbulence. The droplet lifetime of diesel follows a trend where increasing ambient pressure for a given turbulence intensity (fan speed) results in a longer droplet lifetime. This trend occurs as a result of increasing

the ambient pressure which causes the droplet surface temperature to increase; however, this increase is mitigated and dominated by the reduced mass transfer number which results in an increased droplet lifetime.



**Figure 4.5.** Normalized diesel droplet lifetime for different ambient pressures at a given fans speed at  $T_{amb} = 473$  K.

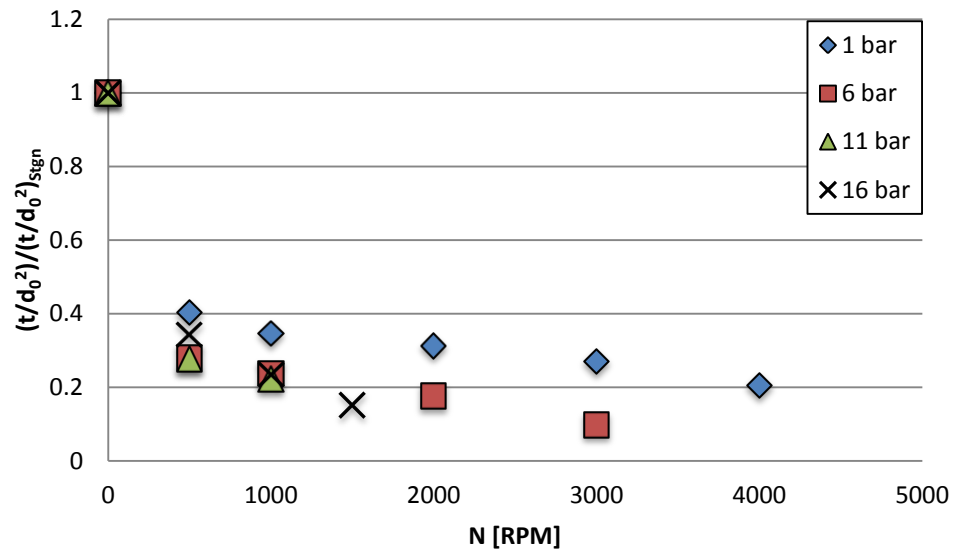
Figure 4.5 presents the normalized diesel droplet lifetime as a function of ambient pressure for different fan speeds at a relatively low ambient temperature of 473 K. For each fan speed, the droplet lifetime was normalized by its corresponding value at 1 bar ambient pressure. This figure shows that the normalized droplet lifetime increases with ambient pressure at any given fan speed (i.e. turbulence intensity). It can also be observed that, at any given ambient pressure, the normalized droplet lifetime decreases with turbulence intensity where the differences between the different fan speeds grow with ambient pressure.



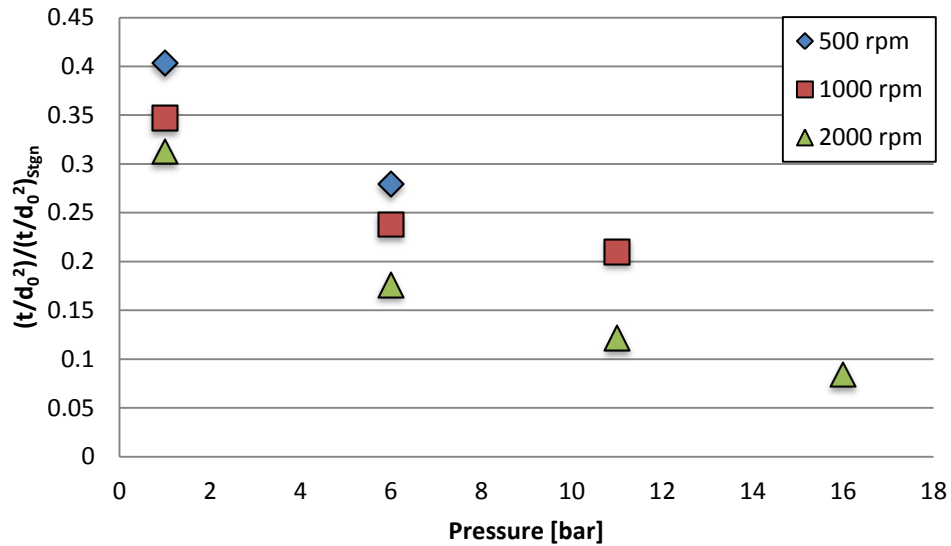
**Figure 4.6.** Diesel droplet lifetime as a function of fans rotational speed for different ambient pressures at  $T_{\text{amb}} = 473 \text{ K}$ .

Figure 4.6 presents the diesel droplet lifetime as a function of fan speed (i.e., turbulence intensity) at various ambient pressures. This figure shows that increasing the fan speed at fixed ambient conditions (i.e., ambient temperature and pressure) reduces the droplet lifetime of diesel fuel for all of the tested ambient pressures. The transition from free convection (0 RPM) to forced convection (500 RPM) shows a drastic decrease in droplet lifetime for all ambient pressures. The presence of the turbulence allows for greater heat transfer by means of convection as well as enhancing the convection of fuel vapour away from the vicinity of the droplet surface via turbulent diffusion. Further increases in fan speed beyond 500 RPM create less substantial reduction in the diesel droplet lifetime. However, it should be noted that increased ambient pressure improves the relative decrease in droplet lifetime with respect to fan speed. Figure 4.7 helps to visualize these relative differences by normalizing the droplet lifetime by its corresponding value at 0 RPM. Figure 4.7 shows that while normalized droplet lifetime

of diesel fuel decreases with fan speed, it also decreases with ambient pressure at a given fan speed for ambient pressures less than 12 bar. The relative effects of diffusing the fuel vapour away from the droplet surface are shown to be more vital at elevated ambient pressures in comparison to the free convection case where the forced convection shows that diesel fuel requires greater heat transfer to vaporize its heavier components.



**Figure 4.7.** Normalized diesel droplet lifetime as a function of fans speed for different ambient pressures at  $T_{\text{amb}} = 473$  K.



**Figure 4.8.** Normalized droplet lifetime of diesel fuel as a function of ambient pressure at  $T_{amb} = 473$  K.

Figure 4.8 presents the normalized droplet lifetime of diesel fuel as a function of ambient pressure for different fan speeds. The droplet lifetimes were normalized by the droplet lifetime corresponding to the free convection case at each respective ambient pressure. This figure shows that increasing the turbulence intensity not only reduces the droplet lifetime for a given ambient pressure but the effect of reducing droplet lifetime is enhanced at elevated ambient pressures. This figure helps to clarify the dominant parameter affecting B0 evaporation where subsequent increases in fans rotational speed significantly reduce the droplet lifetime, while increases in ambient pressure causes a reduction in the normalized droplet lifetime for any given fans rotational speed.

## 4.2.2. Biodiesel Droplet

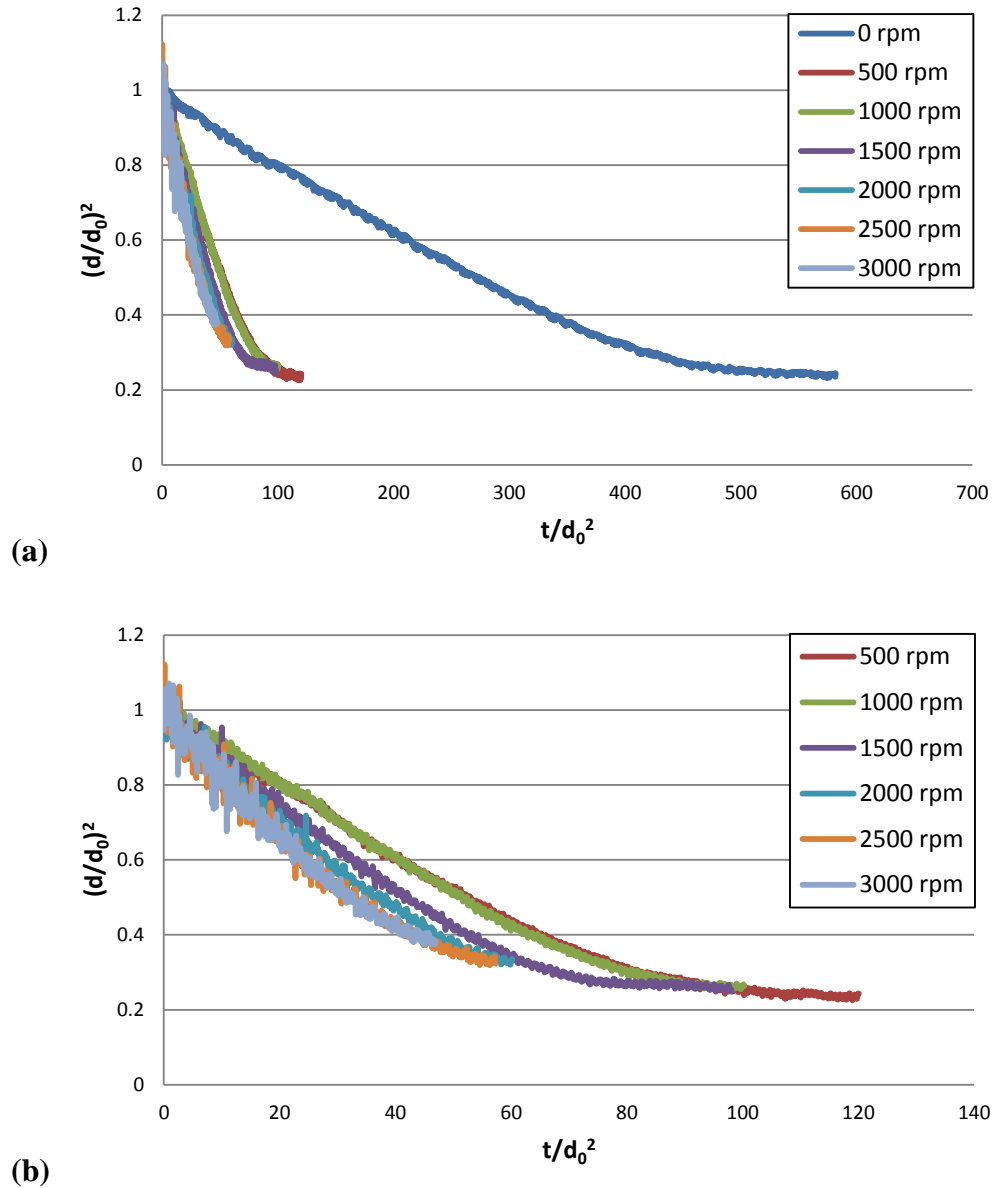


**Figure 4.9.** Time history for squared normalized diameter of biodiesel droplet for various fan speeds at  $P_{\text{amb}} = 6$  bar and  $T_{\text{amb}} = 473$  K for (a) free and forced convection cases and (b) forced convection cases.

Figure 4.9 (a) and Figure 4.9 (b) present the normalized surface regressions profiles for biodiesel (B100) droplet at elevated ambient temperature and pressure for different fan speeds. Biodiesel droplet vaporization at this relatively low ambient

temperature can be seen in Figure 4.9 (a) and Figure 4.9 (b) that both free and forced convection cases follow the classical  $d^2$ -law. Droplet evaporation experiments found in literature dealing with biodiesel at this ambient temperature have only shown data for atmospheric pressure, where results for rapeseed and sunflower [5] and palm oil [9] have been shown to follow the  $d^2$ -law. The observed oscillations of the projected droplet surface area increase with fan speed in a similar manner as those observed with the diesel droplet; however, the amplitude of the oscillations observed for B100 are larger than those observed for diesel fuel, which indicates that B100 is more susceptible to deformation via interaction with the turbulent structures.

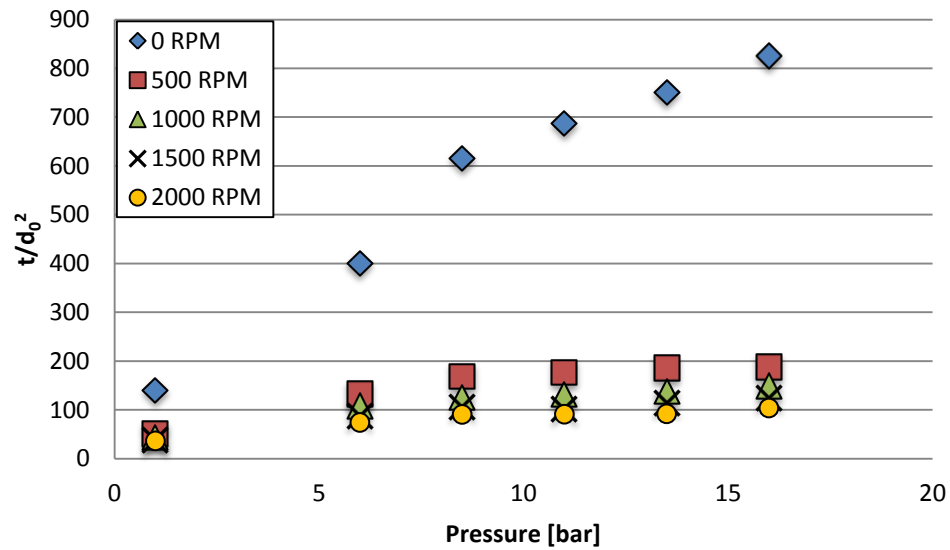


**Figure 4.10.** Biodiesel droplet lifetime as a function of ambient pressure for various fan speeds at  $T_{amb} = 473$  K.

Figure 4.10 presents droplet lifetime of biodiesel (B100) as a function of ambient pressure for different fan speeds. This figure shows that biodiesel droplet lifetime decreases with turbulence intensity (i.e., fan speed) at all tested ambient pressures. This trend follows a similar behaviour observed by Birouk and Fabbro [50] where ambient

pressure was found to retard the evaporation rate of n-heptane droplet where that trend was observed for all fan speeds. Birouk and Fabbro [50] conducted their experiments at room temperature; therefore heat transfer through modes of convection as well as conduction through the suspension fiber was minimal. The differences between the present experimental data and that of Birouk and Fabbro [50] are the fuel type (biodiesel which is a multicomponent fuel primarily composed of C16-C18 methyl esters derived from soybean oil [49]) and heat transfer to the droplet due to the elevated ambient temperature as previously mentioned.

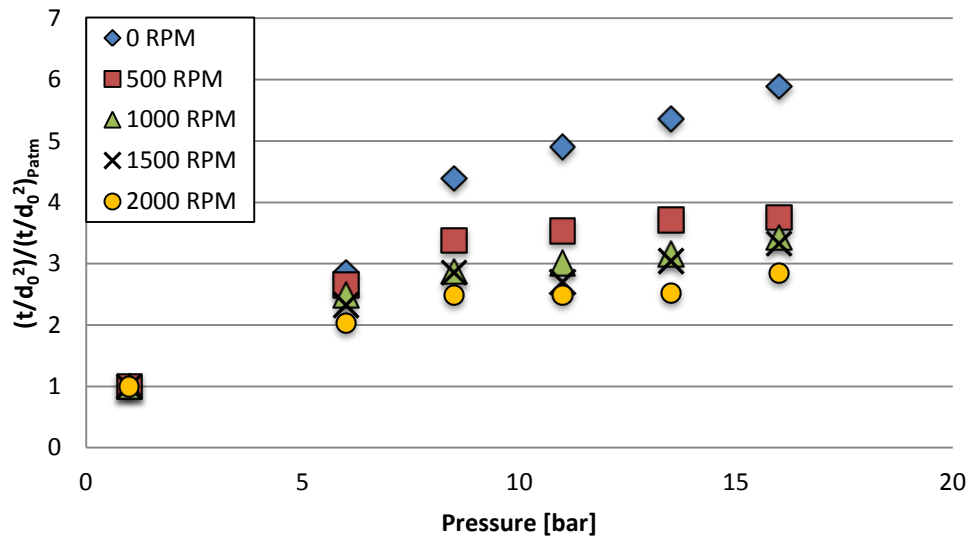


**Figure 4.11.** Normalized droplet lifetime of B100 as a function of ambient pressure for various fan speeds at  $T_{amb} = 473$  K.

Figure 4.11 presents the normalized droplet lifetime of biodiesel (B100) as a function of ambient pressure for different fan speeds (i.e., turbulence intensities). For each fan speed, the droplet lifetime is normalized by the corresponding value at atmospheric pressure. This figure shows more clearly the same trend found from Figure 4.10, where the normalized droplet lifetime increases with ambient pressure for all tested

fans rotational speed. The relative increase in droplet lifetime due to ambient pressure appears to decrease with fan speed; this implies that the turbulence is more effective at diffusing fuel vapour away from the droplet surface as well as enhancing convective heat transfer to the droplet surface. The turbulence hastens convective heat transfer to the droplet surface, which in turn allows the heat to internally diffuse within the droplet causing the droplet temperature to increase. The increased droplet temperature accelerates the phase change from liquid to solid and consequently generating more vapour at the droplet surface. The role of turbulence is to diffuse the vapour away from the droplet surface which results in a steeper gradient of vapour mass at the droplet surface and extending outwards.

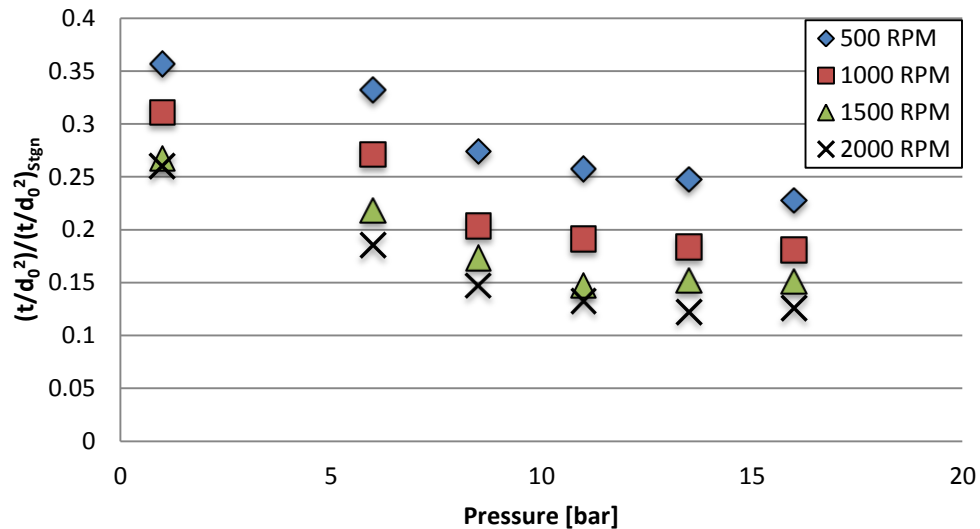


**Figure 4.12.** Biodiesel droplet lifetime as a function of ambient pressure for different fan’s speed.

Figure 4.12 presents biodiesel (B100) droplet lifetime as a function of ambient pressure for various fan speeds. The droplet lifetime was normalized using the corresponding value under free convection (i.e., 0 RPM) conditions at a given ambient

pressure. Two observations can be made from this figure; the first shows a reduction in the droplet lifetime with increasing turbulence intensity, and the second shows a general trend where the normalized droplet lifetime of B100 decreases with ambient pressure for a given turbulence intensity. The debate as to which parameter has a stronger influence over the droplet lifetime of B100 can be seen in this figure, where fans rotational speed (i.e., turbulence intensity) is clearly the dominant parameter affecting B100 evaporation. The influence of turbulence intensity is more apparent at elevated ambient pressures by the larger differences in droplet lifetime between the various fan speeds; this follows the trend observed by Birouk and Fabbro [50], where n-heptane droplet evaporation was accelerated by the presence of turbulence which was further exacerbated by ambient pressure.

### 4.2.3. Biodiesel-Diesel Blends

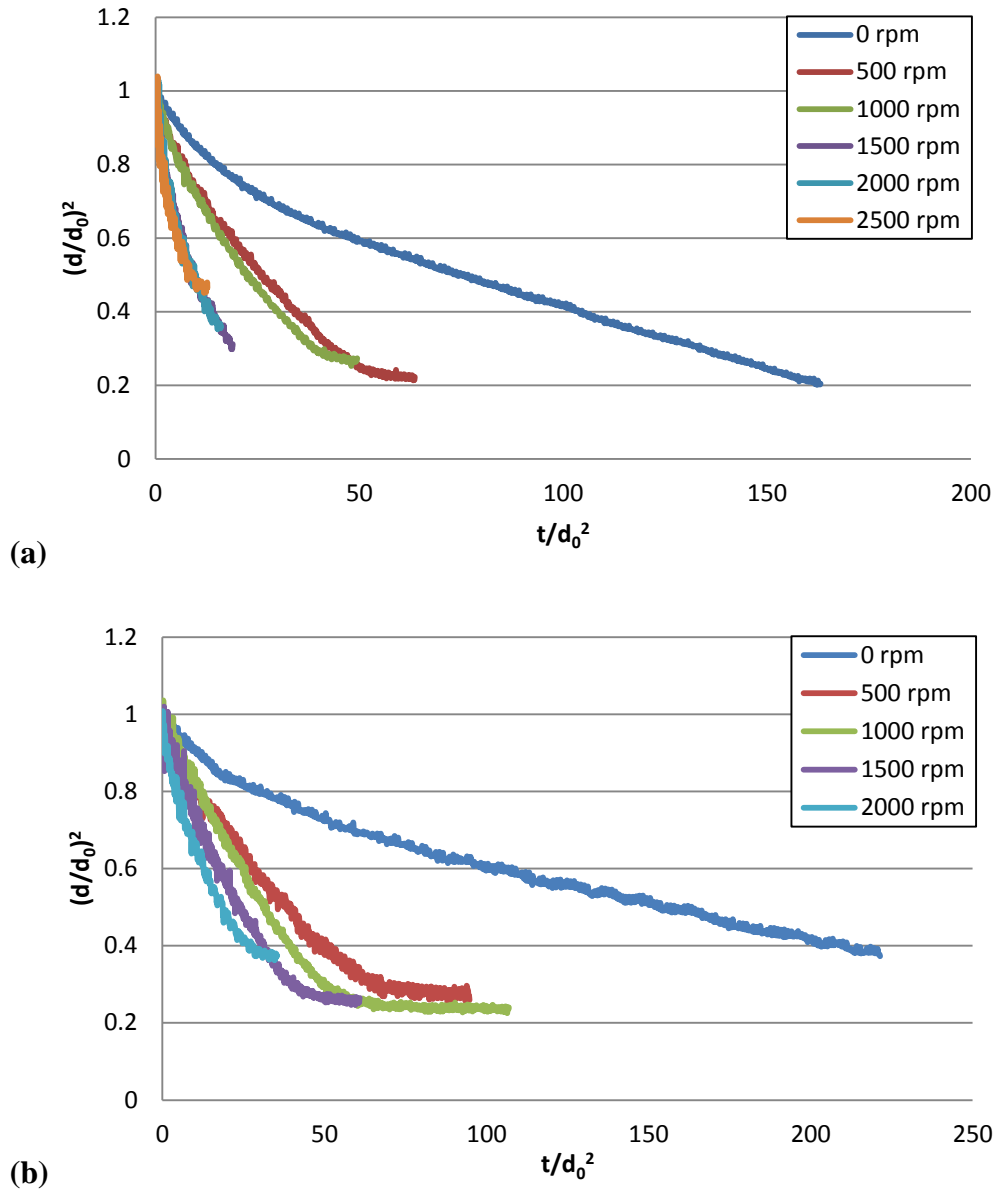


**Figure 4.13.** Time history of the squared normalized diameter for different fans speeds at  $T_{\text{amb}} = 473\text{K}$  and  $P_{\text{amb}} = 6$  bar for (a) B20 droplet and (b) B50 droplet.

Figure 4.13 (a) and Figure 4.13 (b) present the time history of the normalized droplet diameter for biodiesel-diesel blends B20 and B50 (i.e., 20 and 50 percent biodiesel by volume), respectively. Initial observations show the influence of both parent fuels on each respective fuel blend, where the beginning of droplet evaporation shows a

non-linear decrease in the projected droplet surface area, this non-linear behaviour is representative of diesel droplet evaporation under these ambient conditions. The surface regression profiles for both fuel blends transition from a non-linear behaviour to a quasi-steady or linear behaviour which is indicative of biodiesel evaporation and hence follows the  $d^2$ -law. The transition between behaviours in the case of B20 droplet only requires an additional 5 to 10 percent of the droplet lifetime in comparison with the B50 droplet. The non-linear behaviour becomes a less significant portion of the droplet lifetime for both fuel blends as fan speed (i.e., turbulence intensity) increases, especially from free convection (i.e., 0 RPM) conditions to forced convection (i.e., 500 RPM and higher) conditions. Further increases in fan speed provide a temporal reduction to the non-linear portion of the surface regression profile; however, the existence of this behaviour remains even at the highest fan speeds used in this experimental work. The non-linear behaviour diminishes at higher turbulence intensities as a result of the increased heat transfer to the droplet surface, where the lower molecular weight components of diesel fuel initially vaporize allowing time for the surface temperature of the droplet to increase until it is sufficient to vaporize biodiesel and the heavier diesel components. The presence of biodiesel in the fuel blends is evident, where the percentage of linear behaviour of the droplet lifetime constitutes a value well beyond the percentage of biodiesel present within each blend. It can be observed that the droplet lifetime of B50 is more sensitive to changes in fans rotational speed than the B20 droplet lifetime, this is a result of the biodiesel content present in the blends, where the parent fuels diesel and biodiesel have shown distinctly different levels of sensitivity to changes in fan speed (where biodiesel

droplet lifetimes noticeably decrease with turbulence intensity while diesel droplet lifetimes have comparatively shown minimal change in droplet lifetime).

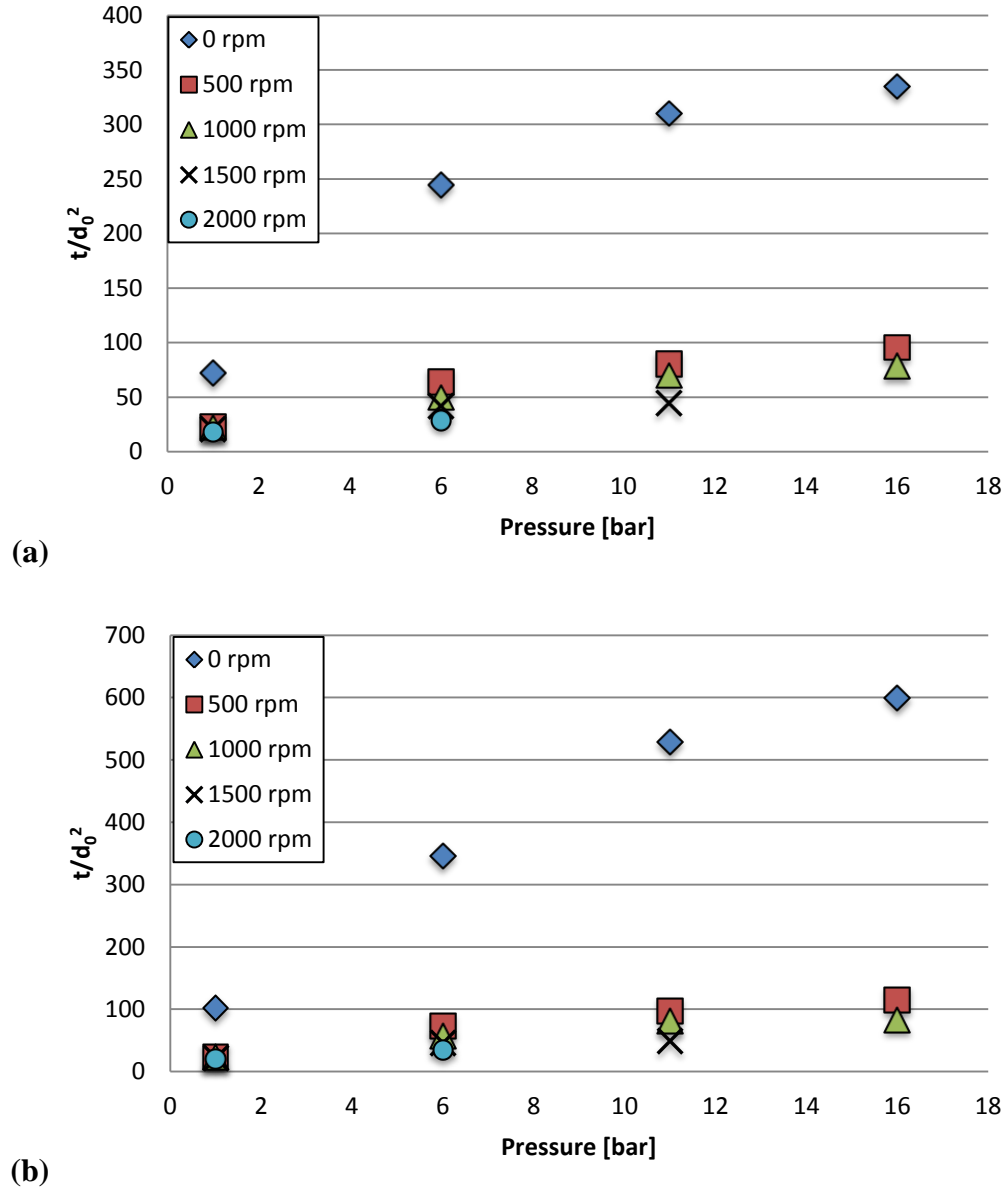
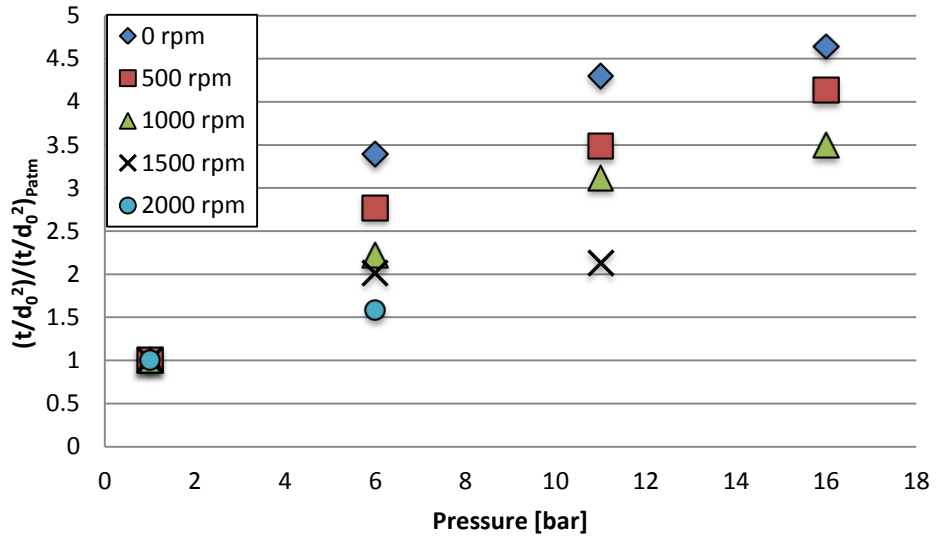


**Figure 4.14.** Droplet lifetime as a function of ambient pressure at a given fans speed at  $T_{amb} = 473$  K for (a) B20 droplet and (b) B50 droplet.

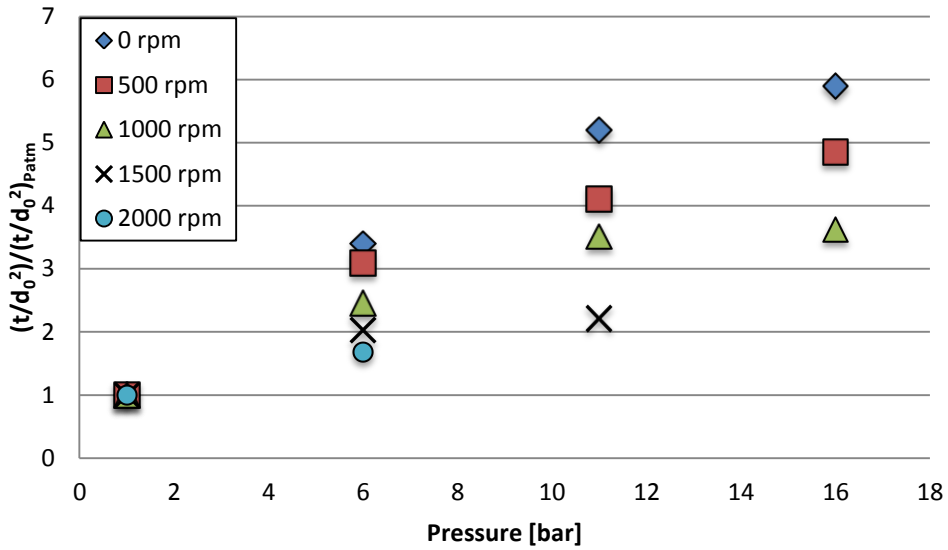
Figure 4.14 (a) and Figure 4.14 (b) present the droplet lifetime as a function of ambient pressure at given fans rotational speed for fuel blends B20 and B50, respectively. Both fuel blends display similar trends observed by the parent fuels with respect to

ambient pressure, where the droplet lifetime increases with ambient pressure at any fans rotational speed. Additionally, both fuel blends have shown similar trends observed by both parent fuels where increasing ambient turbulence results in a reduction in the droplet lifetime at any given ambient pressure.

The relative effect of ambient pressure on the droplet lifetime can be seen for both fuel blends B20 and B50 in Figure 4.15 (a) and Figure 4.15 (b), respectively. The droplet lifetimes were normalized using the corresponding value at atmospheric pressure for each respective fan speed. These figures show how ambient pressure increases droplet lifetime regardless of the fans speed. The blended droplet lifetime trends with respect to ambient pressure follow the same behaviour as their parent fuels.

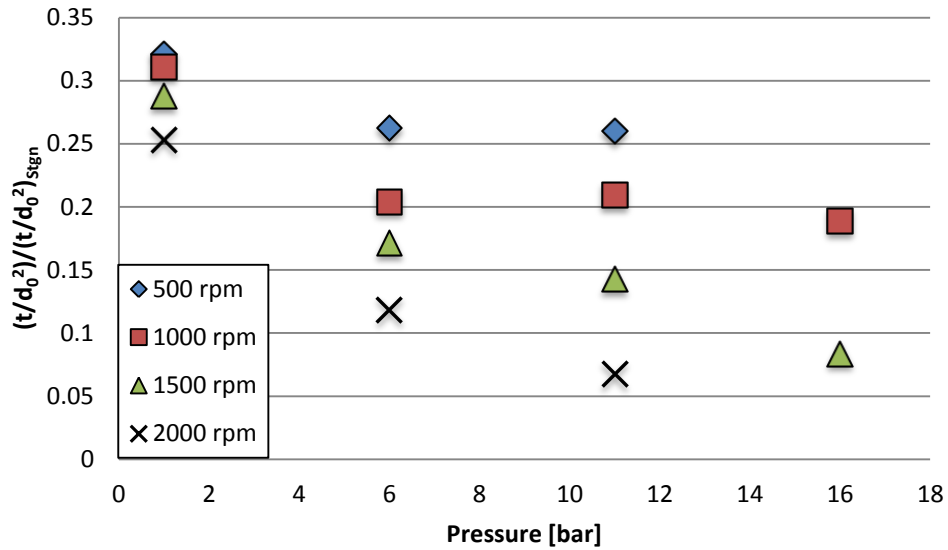


(a)

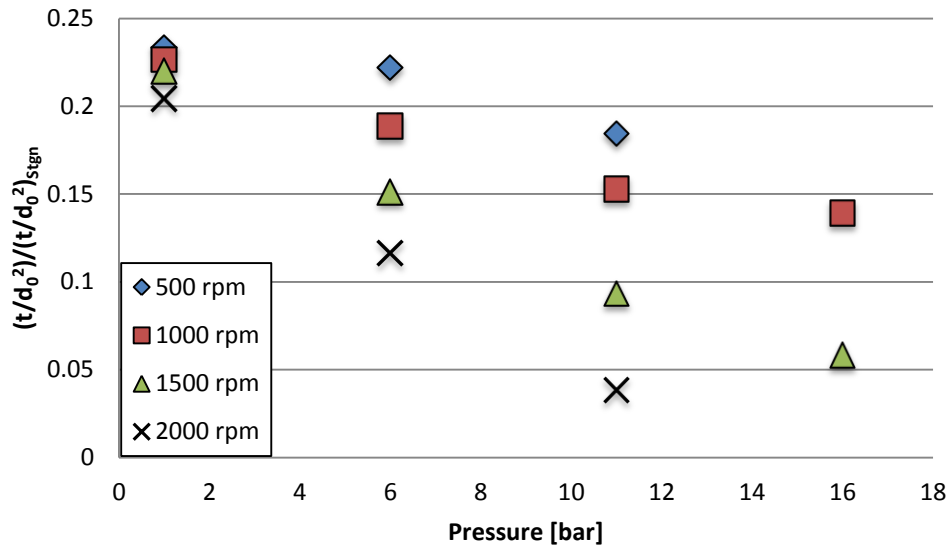


(b)

**Figure 4.15.** Normalized droplet lifetime as a function of ambient pressure at given fan speeds for (a) B20 droplet and (b) B50 droplet.



(a)



(b)

**Figure 4.16.** Variation of droplet lifetime with ambient pressure at different fan speeds for (a) B20 droplet and (b) B50 droplet.

The relative effect of turbulence intensity (i.e., fans speed) is shown in Figure 4.16 where the droplet lifetime is normalized by the values corresponding to free convection conditions at a given ambient pressure. These figures show how ambient turbulence effectively reduces the droplet lifetime for both fuel blends, which follows the behaviour displayed by both parent fuels. The gaps between the droplet lifetimes of

different fans speed increases with ambient pressure where ambient pressure amplifies the reduction in droplet lifetime caused by ambient turbulence. Experimental data for fans speed in excess of 1500 RPM could not be successfully acquired for ambient pressures beyond 11 bar using the present method of droplet suspension. The effect of ambient pressure in enhancing the impact of ambient turbulence is more prominent for the B50 droplet evaporation, whereas the B20 droplet evaporation shows this relationship with less consistency.

#### 4.2.4. Comparison of Droplet Blends

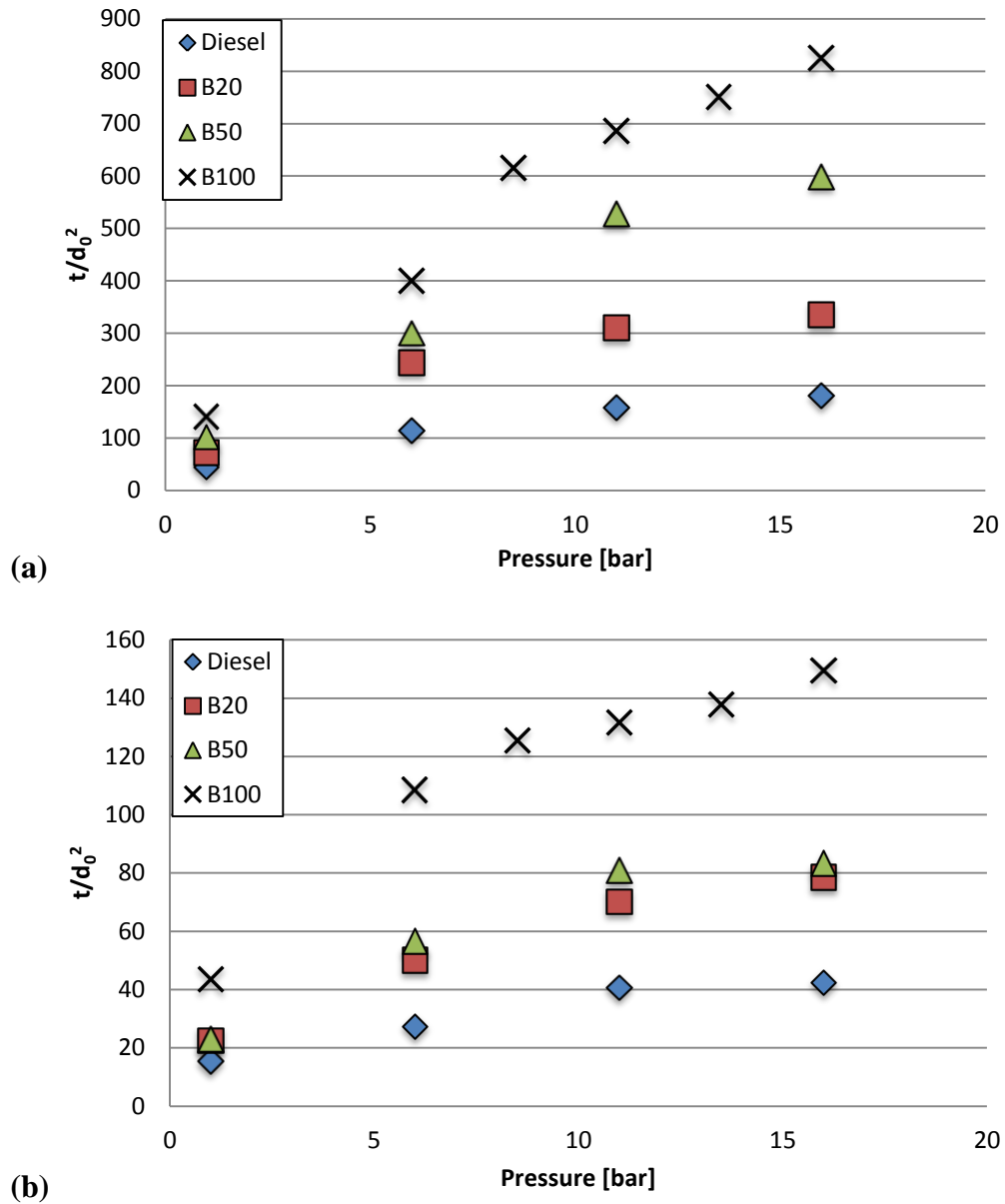


**Figure 4.17.** Comparison of droplet lifetimes for B0, B20, B50 and B100 as a function of ambient pressure at  $T_{amb} = 473$  K for (a) 0 RPM and (b) 1000 RPM.

The comparison of droplet lifetimes for B0, B20, B50 and B100 fuel blends as a function of ambient pressure are shown in Figure 4.17 (a) and Figure 4.17 (b) for fans speed of 0 RPM and 1000 RPM, respectively. In the presence of free convection (i.e., 0 RPM), it appears that droplet lifetime increases not only with biodiesel content, but also

the biodiesel content becomes more significant at elevated ambient pressure such that the relative difference in droplet lifetime between B20 and B50 increases with ambient pressure. For forced convection (i.e., 1000 RPM), biodiesel content still increases droplet lifetime, however, this increase is far less substantial as a function of ambient pressure in comparison with 0 RPM fan speed. One reason behind the reduced difference in droplet lifetime between B20 and B50 at 1000 RPM is due to biodiesel's lower volatility in comparison to that of diesel fuel, where previous experimental work on n-alkane hydrocarbons has shown that turbulent flow creates the highest increase in evaporation of the least volatile fuel droplet with respect to the zero fan speed case [51]. These figures show that the droplet lifetimes of biodiesel-diesel blends increase with biodiesel content, while showing that the increase in biodiesel content does not represent a proportional increase in droplet lifetime. Table 4.2 shows the percentage difference between the experimentally observed droplet lifetime of B20 and B50 blends in comparison to the rule of mixtures weighted average of the parent fuels' corresponding values. The tabulated values show that for all of the flow conditions, except for B50 at 1000 RPM, the observed droplet lifetime not only exceeds the calculated value, but in numerous cases this difference is above 15 percent. The fact that most of the droplet lifetimes of the biodiesel-diesel blends exceeded their parent fuels weighted average estimates (calculated by using the rule of mixtures) shows the dominant presence of biodiesel in the blended fuel droplet. However, the droplet lifetime of B50 was under predicted which further illustrates the non-proportional relationship between the droplet lifetime of the blends and biodiesel content.

**Table 4.2.** Droplet lifetime % difference from weighted average of parent fuels.

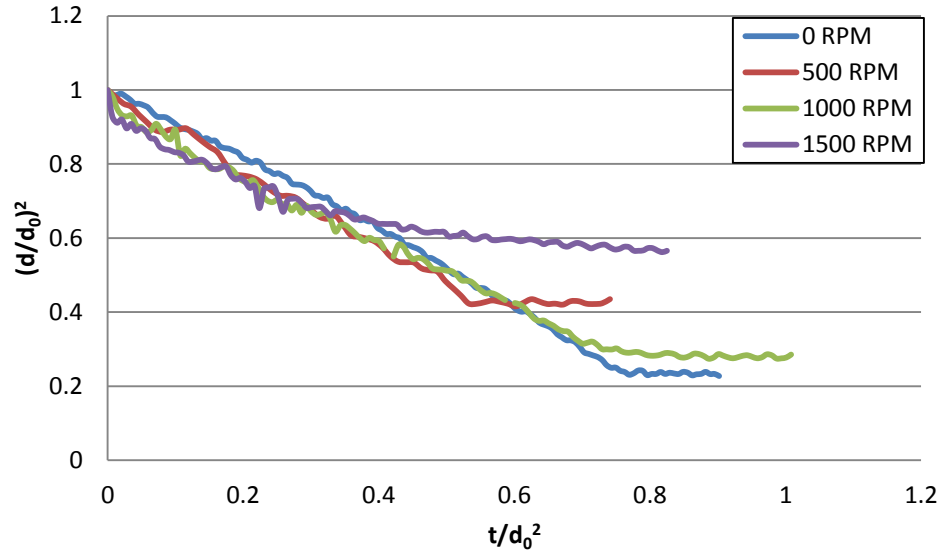
Fan Speed [RPM]	Pressure [bar]	B20 [%]	B50 [%]
0	1	13.86	10.37
0	6	42.35	16.54
0	11	17.38	24.98
0	16	8.30	19.16
1000	1	7.00	-21.84
1000	6	14.67	-16.74
1000	11	19.15	-6.15
1000	16	23.31	-13.03

#### **4.2.5. Error Analysis**

The error analysis has shown that the image processing method used to determine the droplet size yields a maximum error of 7 percent where the majority of the errors lie between 1 and 5 percent of the droplet size. Further discussion of the error analysis can be found in Appendix G.

## Chapter 5 - Results and Discussion: Droplet combustion

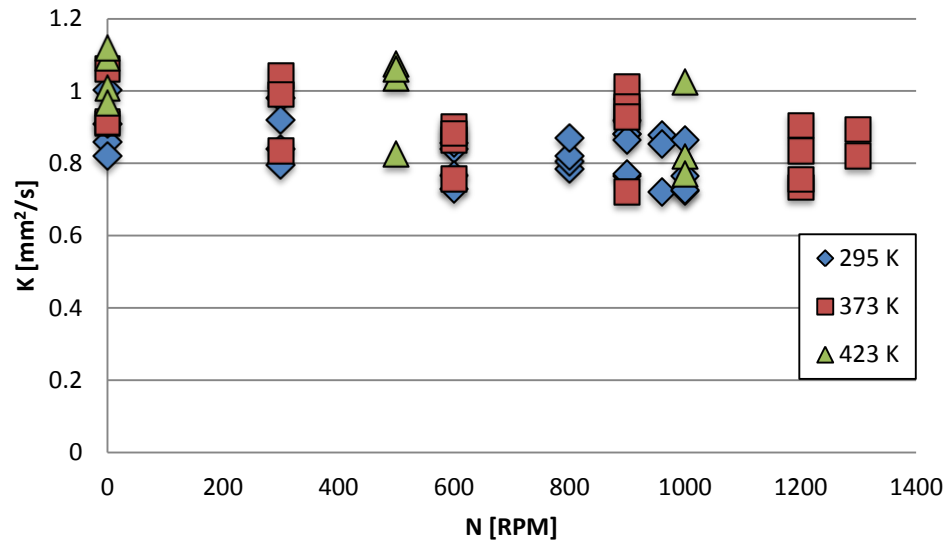
### 5.1. Diesel Droplet Combustion



**Figure 5.1.** Time histories of the normalized droplet projected surface area of diesel droplet burning in turbulent atmosphere at  $T_{\text{amb}} = 423$  K and  $P_{\text{amb}} = 1$  bar.

Figure 5.1 shows the diesel (B0) droplet surface regression profile burning in turbulent environment at an ambient temperature and pressure of 423 K and 1 bar, respectively. Several observations regarding the surface regression profiles of diesel droplet combustion can be made. There are two types of oscillations shown in Figure 5.1. The smaller amplitude high frequency oscillations are caused by the light source as mentioned earlier in the diesel droplet vaporization section of this thesis. The larger amplitudes non-uniform oscillations, which are associated with the fans speed greater than 0 RPM, are caused by the droplet deformation. It can also be observed that the diesel droplet combustion has a linear surface regression profile under both free (zero-rpm) and forced convection conditions; that is, there is no clear distinction between the surface regression profiles under different flow conditions explored here. It should be noted that

for the 1500 RPM fan speed, the diesel droplet surface regression profile appears to have two distinct slopes; the first slope, which is the higher one, corresponds to droplet burning, while the slower (second) slope corresponds to the droplet vaporization which is an indication of the flame extinction prior to the complete depletion of the droplet. Another observation for diesel droplet combustion concerns the non-occurrence of microexplosions during its burning for an ambient temperature of 423 K. However, for ambient temperatures of 295 and 373 K, microexplosions were observed only in the presence of free convective flow. The composition of diesel fuel contains a vast number of components with different volatilities [25]. At lower ambient temperatures, the more volatile components do not preferentially vaporize prior to combustion allowing for components of sufficiently different volatilities to be present within the droplet [53]. These higher volatile components reach a superheated state before diffusion can transport them from the droplet interior to the droplet surface which creates a bubble, leading to a microexplosion.



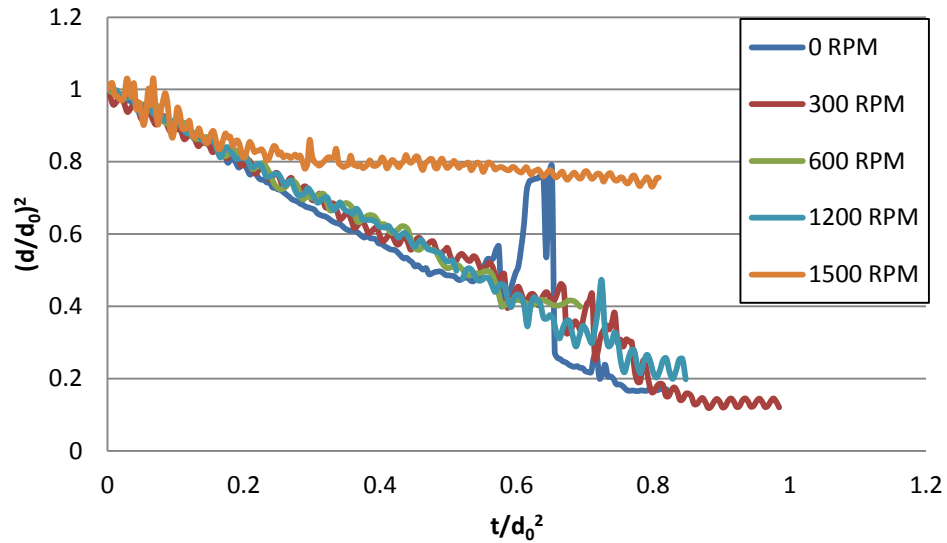
**Figure 5.2.** B0 droplet burning rate as a function of fan speed for different ambient temperatures at  $P_{\text{amb}} = 1$  bar.

Figure 5.2 shows the diesel droplet burning rate for different fan speeds at atmospheric pressure and ambient temperatures up to 423 K (at least 4 tests were completed at any given test conditions). This figure shows that the measured values for the diesel droplet burning rate do not change noticeably when increasing the turbulence level (fans speed) where there is nearly no difference between the turbulent and free convection (zero-rpm). This figure shows also that the burning rate did not vary with ambient temperature at any turbulence level. Furthermore, the turbulence effects on the burning rate for diesel droplet combustion with respect to the corresponding free convection conditions are in agreement with the results found for droplet combustion of mono- and bi-component hydrocarbons [54]. As shown in Figure 5.2, the lower burning rate shown at higher turbulent levels (fans speed) correspond to the conditions near the flame extinction limit. This is attributed to heat losses from the droplet flame due to

increased flow convection around the droplet (that is the entrainment of large cold mass of pockets into the droplet and the convection of the flame away from the droplet). The flame extinction limit was found to increase with ambient temperature where turbulent velocities of 0.80 and 1.0 m/s correspond to flame extinction at ambient temperatures of 295 and 373 K, respectively. Comparatively, the laminar flame speed of diesel fuel is on the order of 0.82 m/s [55] for an ambient temperature of 470 K. Data available for the laminar flame speed of diesel fuel are limited by the difficulty of maintaining a fuel/air mixture for a fuel with a high boiling point and a low vapour pressure [56] at a relatively low ambient temperature. However, it appears that diesel droplet combustion experiences flame extinction at a turbulent velocity that is slightly greater than the laminar flame speed. This disagrees with the reported findings of Birouk et al. [54] where hydrocarbon droplet flame extinction occurred for a turbulent velocity on the same order of magnitude as the corresponding fuel's laminar flame speed.

The repeatability of the results has shown significant spread of the data for diesel droplet combustion under ambient pressure of 1 bar (as shown in Figure 5.2). The range of tested fan speeds has also shown that the maximum relative error of the burning rate does not exceed 20 percent.

## 5.2. Biodiesel Droplet Combustion



**Figure 5.3.** Time histories of the normalized droplet projected surface area of B100 droplet burning with different fan speeds at  $T_{\text{amb}} = 423 \text{ K}$  and  $P_{\text{amb}} = 1 \text{ bar}$ .

Biodiesel droplet combustion time histories for different fan speeds (i.e., turbulence intensities/levels) can be seen in Figure 5.3. The surface regression profile for biodiesel droplet combustion displays similar trend and oscillations to what was found in the diesel droplet combustion (Section 5.1). One phenomenon common to all biodiesel droplets was the occurrence of a microexplosion. The microexplosion takes the form of a sudden and rapid increase in droplet size followed by a relatively quick decrease (i.e. explosion) that reduces the projected droplet surface area, as shown in Figure 5.3. Figure 5.4 shows snapshots of microexplosion during biodiesel droplet combustion where it was observed to occur in the latter half of the droplet lifetime. The existence of microexplosions for droplet combustion of pure biodiesel is quite surprising since the composition is primarily made up of C16-C18 methyl esters [49], whereas microexplosions typically occur within fuel droplets where at least two components have

sufficiently different volatilities (e.g., [53]). The presence of the microexplosion phenomenon does not agree with the B100 droplet combustion experiments conducted by Pan et al. [41] using 445  $\mu\text{m}$  diameter droplets. Pan et al. [41] conducted their experiments at room temperature on a cross fiber composed of two 7  $\mu\text{m}$  diameter carbon fibers. The experimental results reported here were with a much larger (about 500  $\mu\text{m}$  diameter) suspension fiber. Since the microexplosion phenomenon occurs during the latter half of the droplet lifetime, it is believed to be a result of the heat conduction from the flame through the supporting fiber into the droplet interior, raising the fuel temperature of the droplet interior to a superheated state.

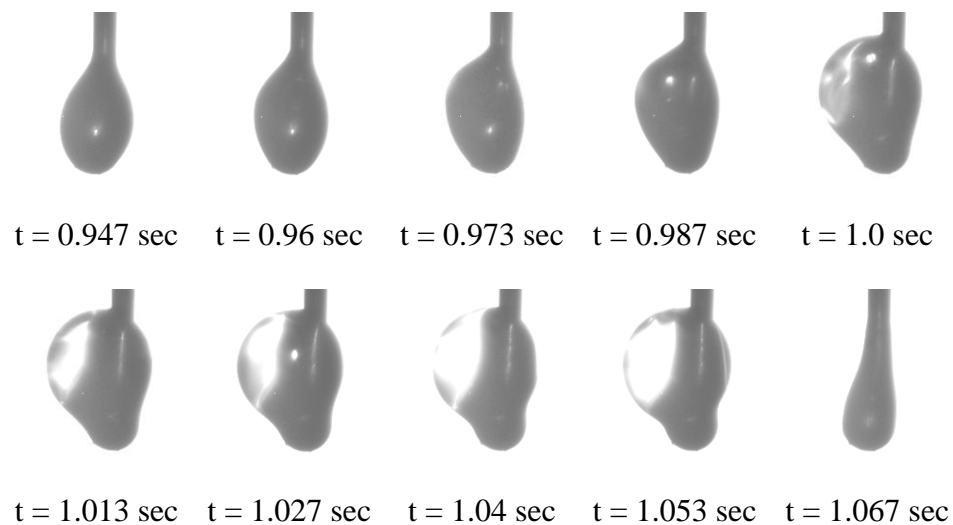


**Figure 5.4.** Snapshots of microexplosion phenomenon occurring during biodiesel droplet combustion for 0 RPM fan speed at  $T_{\text{amb}} = 423 \text{ K}$  and  $P_{\text{amb}} = 1 \text{ bar}$ .

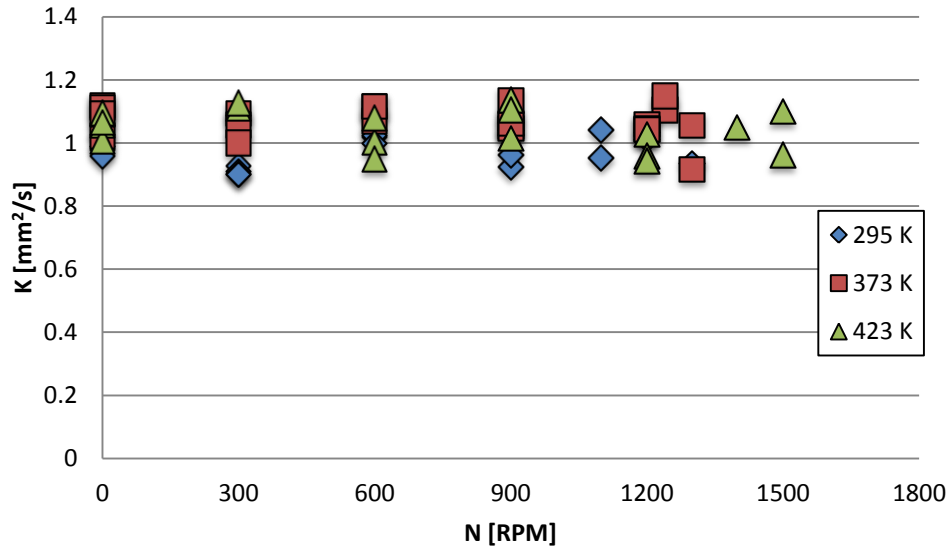


**Figure 5.5.** B100 droplet burning rate as a function of fans speed for various ambient temperatures at  $P_{\text{amb}} = 1$  bar.

Figure 5.5 shows the B100 droplet burning rate for different fans speed at ambient temperatures up to 423 K and atmospheric pressure. Similarly to diesel fuel, the burning rate of B100 fluctuates around the value that corresponds to free convection conditions for turbulence intensities (i.e., fans speeds) greater than zero. That is, the B100 burning rate does not seem to be noticeably affected by the presence of a turbulent flow field around the droplet. The observed trend for the burning rate as a function of turbulent velocity agrees with the results found by Birouk et al. [54] where turbulence effects were negligible in comparison to the stagnant (i.e., 0 RPM) case. In contrast to diesel fuel, the burning rate of B100 does not show a noticeable decrease once the turbulent velocity approaches the flame extinction limit. The flame extinction limit for B100 was found to occur for turbulent velocities between 0.95 and 1.20 m/s at ambient temperatures of 295 and 423 K, respectively. Comparatively, the laminar flame speed of B100 for ambient

conditions of 470 K and atmospheric pressure was only 0.83 m/s. These results show that the flame extinction limit occurs for turbulent velocities greater than the laminar flame speed of B100 which disagrees with the reported findings of Birouk et al. [54] where hydrocarbon flame extinction occurred for turbulent velocity on the same order of magnitude as the laminar flame speed.

### 5.3. Biodiesel-Diesel Blends

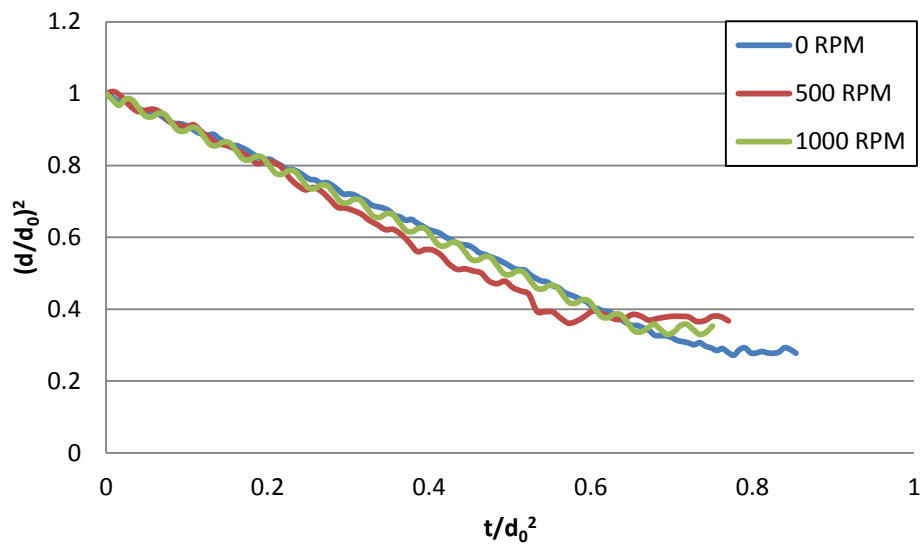


**Figure 5.6.** Time histories of the normalized droplet projected surface area of B20 droplet burning with different fan speeds at  $T_{\text{amb}} = 423$  K and  $P_{\text{amb}} = 1$  bar.

The temporal variation of the normalized squared droplet diameter for different fans speed (i.e., turbulence intensities) at a given ambient pressure for B20 and B50 are shown in Figure 5.6 and Figure 5.7, respectively. B20 and B50 droplet combustion behaviour follows a similar behaviour to its diesel fuel parent in regards to the linearity and presence of oscillations within the surface regression profiles. The distinction between the surface regression profiles for free (i.e., 0 RPM) and forced convection (i.e., starting at 500 RPM) for both blended fuel droplets follow the behaviour of their diesel

fuel parent as these profiles are not noticeably separated as they were for droplet vaporization. B20 droplet combustion was observed to not have microexplosion phenomenon. However, the micro-explosion phenomenon is present for B50 droplet combustion as shown in Figure 5.7 where the time history of the normalized square diameter for B50 clearly shows the presence of microexplosion for the free convection case. In the presence of forced convection (at, e.g., 500 RPM) there is a noticeable sudden reduction in the droplet size at the end of its lifetime. The occurrence of micro-explosion phenomenon is an indication of the dominance of biodiesel content in the B50 blend.

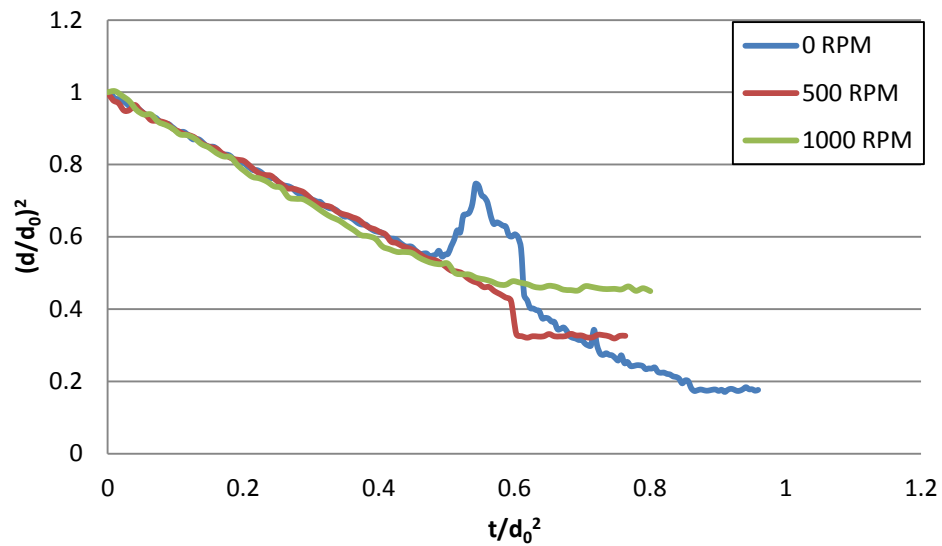


**Figure 5.7.** Time histories of the normalized droplet projected surface area of B50 droplet burning with different fan speeds at  $T_{\text{amb}} = 423 \text{ K}$  and  $P_{\text{amb}} = 1 \text{ bar}$ .

#### 5.4. Comparison of Droplet Blends

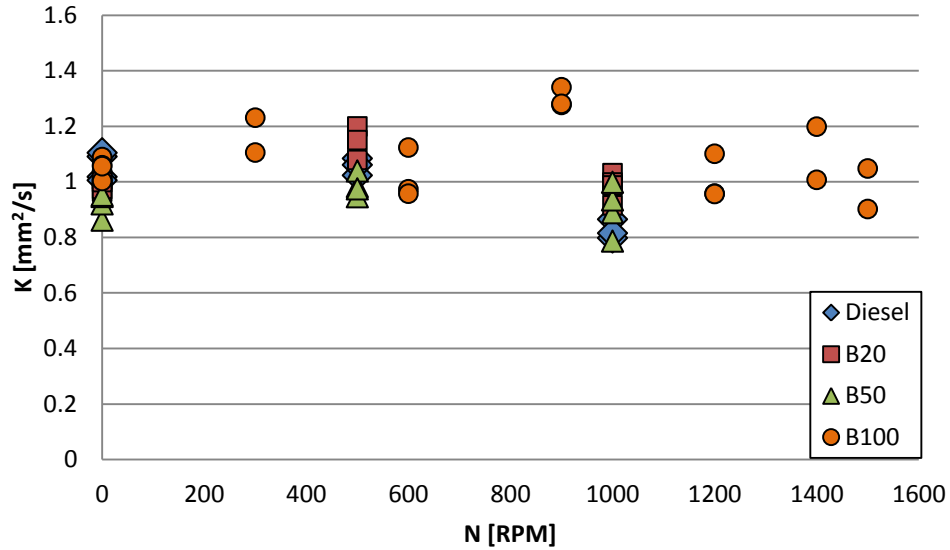


**Figure 5.8.** Comparison of droplet burning rates for B0, B20, B50 and B100 as a function of fan speed at  $T_{amb} = 423$  K and  $P_{amb} = 1$  bar.

Figure 5.8 shows a comparison of the burning rate between the blends and their parent fuels. This figure shows that the trend of the burning rate of the two blends (B20 and B50) is very similar to that of the diesel especially closer to the flame extinction limit. The observed trend of the burning rates for B0, B20, B50 and B100 under normal gravity conditions are comparable to the results obtained by Pan et al. [41] for small droplets with an average diameter of 445  $\mu\text{m}$ . Pan et al. [41] found that biodiesel-diesel blends had slightly lower burning rates than both parent fuels where the lowest value was observed for B50. The burning rates reported by Pan et al. [41] for B0 and B100 were approximately 0.75 and 0.77  $\text{mm}^2/\text{s}$ , respectively under room temperature conditions. In contrast to Pan et al. [41], the results reported here were at ambient temperature ranging between 295 and 423 K where the measured burning rate for B0 and B100 were between 0.99 and 1.05  $\text{mm}^2/\text{s}$ , and 0.99 and 1.06  $\text{mm}^2/\text{s}$ , respectively. Based on the measurements

made for B0 and B100, it appears that the differences between these two sets of data may be attributed to the droplet suspension fiber size. In the present study, the quartz fiber is approximately 500 $\mu\text{m}$  whereas it is less than about 20  $\mu\text{m}$  in Pan et al. [41].

## **5.5. Discussion**

The behaviours of B0 and B100 with respect to changes in turbulence intensity (i.e., fans speed) are similar, with one exception occurring for turbulent velocities close to flame extinction where the burning rate decreases for B0 whereas B100 shows negligible change. It appears from Figure 5.8 that, away from the flame extinction limit, the droplet burning rate did not show any sensitivity to nature of the flow field around the droplet (either laminar or turbulent). This could be attributed the fuel molecular diffusivity which increases in the presence of a flame, and consequently increases the vapor diffusion away from the droplet surface. Therefore, it is possible that the molecular diffusion of vapor masks that induced by the presence of a turbulent flow field around the droplet. As for the decrease in the burning rate of diesel fuel, B20 and B50 at a turbulence level approaching the flame extinction limit, it is believed to be a result of the heat loss from the droplet flame where higher turbulence levels increase the convection of larger mass of cold ambient air into the flame and hence reduce its temperature. On the other hand, the burning rate of B100 near the extinction limit does not follow similar trend which is believed to be the result of its significantly lower molecular diffusivity and also its relatively lower liquid thermal conductivity which cause a relatively higher vapor formation (i.e., gasification rate). It is believed that at this high level of turbulence (i.e., the flame extinction limit), the heat loss from the flame starts regaining its dominance over turbulence diffusion. Rajesh et al. [20], who used a porous sphere, reported that the

burning rate of B0 and B100 increases with the free stream velocity of a laminar flow in the range between 0.40 m/s and 1.46 m/s. Their results agree with those of Raghavan et al. [16] who also examined the biodiesel burning rate where they used a porous sphere exposed to a laminar free stream having a velocity in the range of 0.4 m/s to 1 m/s.

Rajesh et al. [20] also reported that the burning rate of diesel droplet is higher than that of biodiesel at any given laminar free stream velocity. This trend disagrees with the present results of both diesel and biodiesel (B100) as well as their blends under turbulent flow environment at standard pressure and temperature conditions. It is believed that the increase in the burning rate with the free stream mean velocity is due to 1) the increase in the vapour formation around the porous sphere as a results of the proximity of the flame front upstream the porous sphere (in other words, this increase in the vapor formation results from the increased heat transfer into the droplet as the flame front moves closer to the droplet surface (from the free stream side)), and 2) the increased air/oxidizer mass convection at the vicinity of the porous sphere which eventually needed to combust the surrounding available vapor. In contrast, turbulent flow tends to diffuse heat outwards from the droplet flame and convect cold air into the droplet envelop flame. These turbulence effects predominate (i.e., enhanced heat loss from the flame to the ambient) as turbulence intensity is further increased which led to a drop in the burning rate below its corresponding value at zero-RPM (no flow).

## Chapter 6 - . Conclusions and Recommendations

### 6.1. Conclusions

A high pressure vessel capable of generating high levels of turbulence at elevated ambient temperature was employed to study droplet vaporization and combustion of diesel, biodiesel and their blends. The main concluding remarks are summarized below.

Droplet vaporization of B0, B20, B50 and B100 has shown that at a relatively low ambient temperature of 473 K, B0 does not follow the  $d^2$ -law, whereas B100 obeys the  $d^2$ -law. However, the blends B20 and B50 displayed a mixed behaviour of both parent fuels where initially the droplet vaporization follows B0 behaviour before shortly transitioning to B100 behaviour and thereby obeying the  $d^2$ -law throughout most of its lifetime. Droplet lifetime of the blends increased with B100 content. Turbulence was found to exert an apparent effect in reducing the droplet lifetime of all fuels. Moreover, it was found to be more effective in reducing the droplet lifetime (i.e., increasing the droplet vaporization rate) of all fuels when raising the ambient pressure.

Droplet combustion of B0 showed negligible change with turbulence intensity up to 0.40 m/s; however, turbulence intensities beyond 0.40 m/s caused a reduction in the burning rate of B0. This reduction is believed to be due to the heat loss from the flame as a result of the turbulent convective effect. The burning rate of B100 showed similar trend except that the B100 burning rate remained almost unchanged with turbulence level (with respect to no-flow case) until flame extinction. On the other hand, the burning rate of B20 and B50 displayed a mixed behaviour of both parent fuels; nevertheless, diesel fuel had

predominance over the burning rate. Finally, the flame extinction limit of each fuel occurs at a turbulent velocity slightly greater than its counterpart laminar flame speed.

## **6.2. Recommendations for Future Work**

Over the course of this research, a number of recommendations can be made regarding the existing experimental setup as well as further exploration with the experimental testing conditions to help explain the observed phenomena. These recommendations are summarized below.

Recommendations for future research:

- Further exploration of droplet combustion of B0, B20, B50 and B100 is necessary to fully map the combustion behaviour of these fuel droplets with respect to ambient turbulence. To fully map this behaviour, turbulence intensities associated with fan speeds in between existing data points should be tested as well as fan speeds beyond 1000 RPM. Repetition of existing experimental data should be done in order to verify the observed results. The additional data allows for the determination of the more accurate flame extinction conditions, while providing further confirmation of the observed trend for the burning rate as a function of turbulence intensity. The additional experimentation should be conducted at atmospheric as well as elevated ambient pressures where the flame extinction as well as the burning rate trend is necessary for researchers conducting numerical simulations to validate their codes prior to simulating practical combustion systems.

- Investigation of the droplet flame shape and size under different ambient conditions (e.g., temperature, pressure, flow). This could be accomplished using a high speed colour camera possessing a relatively high frame rate. The droplet flame shape and size are important as they affect nearby constituents (e.g., neighbouring droplets, local air movement, etc.) in a spray combustion system via heat and mass transfer. These effects would in turn affect the accuracy of numerical simulations which used these data as part of the validation process.
- Development of enhanced image processing technique is necessary in order to resolve droplet burning rates of all test fuels at elevated ambient pressure. The soot content of the droplet flame obscures the current method of image processing where the flame surrounding the droplet creates gradients of the image contrast across both the droplet as well as the suspending fiber. The droplet size needs to be approximated using an ellipse that can adjust to subtle changes in image contrast in order to obtain proper edge detection.
- Exploration of different methods of droplet suspension, such as the cross fiber technique should be explored to determine the effect of fiber size on droplet suspension experiments (for both vaporization and combustion processes). The cross fiber technique utilizes two very fine fibers as small as  $7\ \mu\text{m}$  to create a cross at the center of the ambient environment that holds the droplet from moving via surface tension. The reduced fiber size would limit the contact area of the droplet-fiber interface which in turn would limit the heat transfer through the fiber into the droplet flame.

- Characterization of the turbulent flow field, specifically, the determination of the integral length under various ambient pressure and temperature conditions is vital for developing better understanding of the effect of turbulence.

Recommendations for improvements to the test apparatus:

- Radial ball bearings that can operate in the presence of ambient temperatures above 250°C are necessary in order to conduct higher temperature experiments within the spherical chamber. These bearings may be available commercially or may require an original design. These high temperature bearings are necessary in order to reduce the substantial service period that ensues over the course of conducting bearing maintenance. The reduced time costs associated with bearing maintenance would allow for faster acquisition of experimental results involving elevated ambient temperatures.
- Installation of a high temperature insulative coating on the inner chamber wall as well as the outer chamber wall to reduce heat transfer to the surrounding ambient. These coatings should have a low thermal conductivity, while the inner coating should also possess a chemical resistance to liquid and gaseous fuels as well as being resistant to fire. The reduced heat loss would hasten the time needed to reach thermal equilibrium as well as provide access to sustainable operating temperatures beyond 473 K, and thus approach those found in practical combustion systems.
- The sealing materials (e.g., o-rings and gaskets) need to be upgraded to materials with higher continuous service temperatures because the seal material limits the maximum operating ambient temperature of the experiment.

- Replacement of the of heating elements of one of the two existing two heating plates in order increase the power/heat output which allow to achieve higher ambient temperature as well as reduce the heat up.
- Redesign of the injector tube assembly is necessary in order to provide greater rigidity and reduce movement that is not associated with the droplet injection procedure. The redesign should use a material that is stronger than aluminum while utilizing a tighter fitting connection between the injector tube and the injector-chamber adapter. The relative movement of the injector tube creates difficulties while attempting to align the droplet injection needle with the suspended fiber. Also, the relative movement of the injector tube has caused several quartz fibers to break over the course of experimental testing which has resulted in slower acquisition of experimental data.

## References

- [1] S.P. Singh and Dipti Singh, Biodiesel production through the use of different sources and characterization of oils and their esters as the substitute of diesel: A review, *Renewable and Sustainable Energy Reviews* 14 (2010) 200-216
- [2] I.M. Atadashi, M.K. Arousa and A. Abdul Aziz, High quality biodiesel and its diesel engine application: A review, *Renewable and Sustainable Energy Reviews* 14 (2010) 1999-2008
- [3] A. Rehman, D.R. Phalke and R. Pandey, Alternative fuel for gas turbine: Esterified jatropha oil-diesel blend, *Renewable Energy* 36 (2011) 2635-2640
- [4] A. Datta and B.K. Mandal, Biodiesel production and its emissions and performance: A review, *IJSER* 3 (2012) 1-6
- [5] C. Morin, C. Chauveau and I. Gokalp, Droplet vaporisation characteristics of vegetable oil derived biofuels at high temperatures, *Exp. Thermal and Fluid Sci.* 21 (2000) 41-50
- [6] C. Morin, C. Chauveau, P. Dagaut, I. Gokalp and M. Cathonnet, Vaporization and oxidation of liquid fuel droplets at high temperature and high pressure: Application to n-alkanes and vegetable oil methyl esters, *Comb. Sci. And Tech.* 176 (2004) 499-529
- [7] K. Kobayasi, The evaporation velocity of single droplets of liquids, *The Technology Reports of the Tohoku University* 18 (1954) 209-222
- [8] T. Daho, G. Vaitilingom, O. Sanogo, S.K. Ouiminga, B.G. Segda, J. Valette, P. Higelin and J. Koulidiati, Model for predicting evaporation characteristics of vegetable oil droplets based on their fatty acid composition, *Int. J. Heat Mass Transfer* 55 (2012) 2864-2871
- [9] Promvongsa, Vallikul, Fungtammasan and Grehan, On Evaporation Constants of Biodiesel-Diesel Blends: The Effects of Blending Ratios, *Journal of Metals, Materials and Minerals* 20 (2010) 43-45
- [10] L. Zhang and S. Kong, High-pressure vaporization of multi-component petroleum-biofuel mixtures under engine conditions, *Combustion and Flame* 158 (2011) 1705-1717
- [11] Y. Ra and R.D. Reitz, A vaporization model for discrete multi-component fuel sprays, *International Journal of Multiphase Flow* 35 (2009) 101-117
- [12] J.S. Chin and A.H. Lefebvre, The role of the heat-up period in fuel drop evaporation, *Int J Turbo Jet-Engines* 2 (1985) 315-325

- [13] X. Gu, S. Basu and R. Kumar, Dispersion and vaporization of biofuels and conventional fuels in a crossflow pre-mixer, *Int. J. Heat Mass Transfer* 55 (2012) 336-346
- [14] K. Kobayasi, An experimental study on the combustion of a fuel droplet, *Proc. Combust. Inst.* 5 (1954) 141-148
- [15] A.J. Marchese, T.L. Vaughn, K. Kroenlein and F.L. Dryer, Ignition delay of fatty acid methyl ester fuel droplets: Microgravity experiments and detailed numerical modeling, *Proc. Combust. Inst.* 33 (2011) 2021-2030
- [16] V. Raghavan, S. Rajesh, S. Parag and V. Avinash, Investigation of combustion characteristics of biodiesel and its blends, *Comb. Sci. Technol.* 181 (2009) 877-891
- [17] S. Parag and V. Raghavan, Experimental investigation of burning rates of pure ethanol and ethanol blended fuels, *Combust. Flame* 156 (2009) 997-1005
- [18] T.X. Li, D.L. Zhu, N.K. Akafuah, K. Saito and C.K. Law, Synthesis, droplet combustion, and sooting characteristics of biodiesel produced from waste vegetable oils, *Proc. Combust. Inst.* 33 (2011) 2039-2046
- [19] M.L. Botero, Y. Huang, D.L. Zhu, A. Molina and C.K. Law, Synergistic combustion of droplets of ethanol, diesel and biodiesel mixtures, *Fuel* 94 (2012) 342-347
- [20] S. Rajesh, V. Raghavan, U.S.P. Shet and T. Sundararajan, Analysis of quasi-steady combustion of *Jatropha* bio-diesel, *Int. Commun. Heat Mass* 35 (2008) 1079-1083
- [21] Y.C. Liu, T. Farouk, A.J. Savas, F.L. Dryer and C.T. Avedisian, On the spherically symmetrical combustion of methyl decanoate droplets and comparisons with detailed numerical modeling, *Combust. Flame* 160 (2013) 641-655
- [22] D.J. Cookson, P. Iliopoulos and B.E. Smith, Composition-property relations for jet and diesel fuels of variable boiling range, *Fuel* 74 (1995) 70-78
- [23] M. Yupo, L. Xiangrong, W. Xiangyuan and L. Fushui, An experimental study on diesel fuel droplets coupling evaporation, *Advanced Materials Research* 383-390 (2012) 3068-3076
- [24] G.M. Faeth, Current status of droplet and liquid combustion, *Prog. Energy Combust. Sci.* 3 (1977) 191-224
- [25] Shell Canada Limited, "Material Safety Data Sheet Ultra Low Sulfur Diesel Fuel." Calgary, AB, Canada: Shell Canada Limited.

- [26] G.A.E. Godsave, Study of the combustion of drops in a fuel spray – the burning of single drops of fuel, Fourth Symposium (International) in Combustion (1953) 818-830
- [27] L. Zhang and S. Kong, Vaporization modeling of petroleum-biofuel drops using a multi-component approach, *Combustion and Flame* 157 (2010) 2165-2174
- [28] A.M. Lippert and R.D. Reitz, Modeling of multicomponent fuels using continuous distributions with application to droplet evaporation and sprays, SAE (1997) 131-145
- [29] J. Tamim and W.L.H. Hallett, A continuous thermodynamics model for multicomponent droplet vaporization, *Chem. Eng. Sci.* 50 (1995) 2933-2942
- [30] L. Zhang and S. Kong, Modeling of multi-component fuel vaporization and combustion for gasoline and diesel spray, *Chem. Eng. Sci.* 64 (2009) 3688-3696
- [31] W.L.H. Hallett, A simple model for the vaporization of droplets with large numbers of components, *Combust. Flame* 121 (2000) 334-344
- [32] J.S. Chin and A.H. Lefebvre, Steady-state evaporation characteristics of hydrocarbon fuel drops, *AIAA Journal* 21 (1983) 1437-1443
- [33] G.S. Zhu and R.D. Reitz, Engine fuel droplet high-pressure vaporization modeling, *J. Eng. Gas Turbines Power* 123 (2001) 412-418
- [34] J. Barata, Modelling of biofuel droplets dispersion and evaporation, *Renewable Energy* 33 (2008) 769-779
- [35] A. Saha, R. Kumar and S. Bahu, Infrared thermography and numerical study of vaporization of pure and blended bio-fuel droplets, *Int. J. Heat Mass Transfer* 53 (2010) 3862-3873
- [36] K. Saha, E. Abu-Ramadan and X. Li, Multicomponent evaporation model for pure and blended biodiesel droplets in high temperature convective environment, *Applied Energy* 93 (2012) 71-79
- [37] W.L.H. Hallett and N.V. Legault, Modelling biodiesel droplet evaporation using continuous thermodynamics, *Fuel* 90 (2011) 1221-1228
- [38] S. Dirbude, V. Eswaran and A. Kushari, Droplet vaporization modeling of rapeseed and sunflower methyl esters, *Fuel* 92 (2012) 171-179
- [39] L. Raslavicius and Z. Bazaras, Variations in oxygenated blend composition to meet energy and combustion characteristics very similar to the diesel fuel, *Fuel Process. Technol.* 91 (2010) 1049-1054.

- [40] M. Saito, M. Hosikawa and M. Sato, Enhancement of evaporation/combustion rate coefficient of a single fuel droplet by acoustic oscillation, *Fuel* 75 (1996) 669-674
- [41] K. Pan, J. Li, C. Chen and C. Wang, On droplet combustion of biodiesel fuel mixed with diesel/alkanes in microgravity condition, *Combust. Flame* 156 (2009) 1926-1936
- [42] L. Raslavicius and Z. Bazaras, Prediction of multi-component effects on ignition delay of oxygenated diesel fuel blends, *Indian J. Eng. Mater. Sci.* 17 (2010) 243-250
- [43] S.R. Gollahalli, M.L. Rasmussen and S.J. Moussavi, Combustion of drops and sprays of No.2 diesel oil and its emulsions with water, *Proc. Combust. Inst.* 18 (1981) 349-360
- [44] P. Prakash, V. Raghavan and P.S. Mehta, Analysis of multimode burning characteristics of isolated droplets of biodiesel-diesel blends, *J. Energ. Resour-ASME* 135 (2013) 024501
- [45] K. Pan and M. Chiu, Droplet combustion of blended fuels with alcohol and biodiesel-diesel in microgravity condition, *Fuel* (2013) article in press.
- [46] T.I. Farouk, Y.C. Liu, A.J. Savas, C.T. Avedisian and F.L. Dryer, Sub-millimeter sized methyl butanoate droplet combustion: microgravity experiments and detailed numerical modeling, *Proc. Combust. Inst.* 34 (2013) 1609-1616
- [47] L. Raslavicius and D. Marksaitis, Research into three-component biodiesel fuels combustion process using a single droplet technique, *Transport* 22 (2007) 312-315
- [48] S.C. Fabbro, "An experimental test facility for studying the effects of turbulence on the evaporation of fuel droplets at elevated pressure and temperature conditions," M. Sc. Thesis, Dept. Mech. & Mfg. Eng., University of Manitoba, Winnipeg, MB, 2012.
- [49] Marathon Petroleum Company LP, "Material Safety Data Sheet Marathon Biodiesel B100." Findlay, OH, USA, 2010.
- [50] M. Birouk and S.C. Fabbro, Droplet evaporation in a turbulent atmosphere at elevated pressure – Experimental data, *Proc. Combust. Inst.* 34 (2013) 1577-1584
- [51] M. Birouk, C. Chauveau, B. Sarh, A. Quilgars and I. Gokalp, Turbulence effects on the vaporization of monocomponent single droplets, *Combust. Sci. Technol.* 113-114 (1996) 413-428
- [52] Chromalox Inc. "Tubular Heaters Design & Installation Guidelines" [Online]. Available: <http://www.chromalox.com/catalog/resources/DG-component-tubular-heaters.pdf> [July 13, 2013].

- [53] J.C. Lasheras, A.C. Fernandez-Pello and F.L. Dryer, Experimental observations on the disruptive combustion of free droplets of multicomponent fuels, *Combust. Sci. Technol.* 22 (1980) 195-209
- [54] M. Birouk, C. Chauveau and I. Gokalp, Turbulence effects on the combustion of single hydrocarbon droplets, *Proc. Combust. Inst.* 28 (2000) 1015-1021
- [55] C.T. Chong and S. Hochgreb, Measurements of laminar flame speeds of liquid fuels: Jet-A1, diesel, palm methyl esters and blends using particle imaging velocimetry (PIV), *Proc. Combust. Inst.* 33 (2011) 979-986
- [56] C.T. Chong, "Combustion characteristics of alternative liquid fuels," Ph.D Thesis, Hughes Hall, University of Cambridge, Cambridge, England, 2011.
- [57] Y. Ra, R.D. Reitz, J. McFarlane and C.S. Daw, Effects of fuel properties on diesel engine combustion using diesel and bio-diesel fuels, *SAE Int. J. Fuels Lubr.* 1 (2009) 703-718

## Appendix A - Instrumentation

The following is a list of instrumentation used for measuring the experimental apparatus' operating conditions.

### Temperature Measurement Devices:

- K type thermocouples from Omega Engineering Inc.
  - Model No. KQXL-18G-[,], where [,] refers to the length of the thermocouple probe. Lengths of 6 and 12 inches were used.
  - Accuracy of  $\pm 2.2^{\circ}\text{C}$  or 0.75% of the rated temperature range.

### Pressure Measurement Devices:

- Digital pressure gauge from Ccomp Electronics (USA),
  - Model No.: DPG1000B500PSIG-ON-CC
  - Accuracy:  $\pm 0.25\%$  of full scale  $\pm$  least significant digit
- Pressure Transducer from Omegadyne Inc.
  - Model No.: PX01K1-500GV
  - Zero balance = 1% FS (Full Scale) or 5 psi
  - Linearity:  $\pm 0.05\%$  FS or  $\pm 0.25$  psi
  - Hysteresis:  $\pm 0.05\%$  FS or  $\pm 0.25$  psi
  - Repeatability:  $\pm 0.05\%$  FS or  $\pm 0.25$  psi
- Mechanical Pressure release valve from Swagelok
  - Model No.: SS-4CA-150
  - Adjustable cracking pressure range: 150-350 psi

Fan Speed Measurement Devices:

- Stroboscope from Shimpo Instruments (by ELECTROMATIC Equip't Co., Inc.)
  - Model No.: DT-315A
  - Flash Speed Range: 100-30,000 flashes per minute
  - Accuracy: +0.01% of reading

## Appendix B - Chamber Seals

### B.1. Introduction

The details regarding the various sealing surfaces of the spherical chamber are presented in this section where the specifications for the gaskets, o-rings and the fan shaft seals are presented in this appendage.

### B.2. Gasket Seals:

Gasket seals are used to create a seal against the surface of a quartz window; there are two sizes of windows corresponding to chamber port openings with diameters of 4 and 5 inches.

**Table B.1.** Gasket size specifications.

Gasket Location	Inside Diameter [in]	Outside Diameter [in]	Thickness [in]
4 inch View Port	4	4 15/16	1/16
5 inch View Port	5	5 15/16	1/16

The current gasket material in service is called NA-60, however previous experimentation was done using gaskets made of the following materials; graphite and Teflon. The material properties for all of the gasket materials are listed below.

**Table B.2.** Gasket material properties.

Property	NA-60 [web]	Graphite	PTFE (Teflon)
Max Pressure Rating (psi).	1000	2000	300
Max Temp. Limit (°F)	700	850	500
Max Contin. Temp. Limit (°F)	400	N/A	N/A
Max P x T (psi x F)	350,000	N/A	150,000
Colour	Green	Silver-gray	White

### B.3. O-ring Seals:

Sealing the rest of the flange ports was done with static o-ring seals as well as two dynamic o-ring seals for the droplet injection system. The various o-rings sizes are listed below for each respective seal in Table B.3, while the o-ring materials are listed in Table B.4. It should be noted that Viton Fluoroelastomer is a registered trademark of DuPont.

**Table B.3.** O-ring size specifications.

O-ring Locations	Inside Diameter [in]	Outside Diameter [in]	Thickness [in]	AS568A Dash No.
5 inch View Port	5 3/8	5 5/8	1/8	253
4 inch View Port	4 3/8	4 5/8	1/8	245
Fan Hub Assembly	4 1/4	4 1/2	1/8	244
Fan Shaft Seal	3/4	7/8	1/16	018
Accessory Ports incl. Top Center and Bottom	7/8	1 1/16	3/32	118
Sensor ports	7/8	1 1/16	3/32	118
Injector Adapter and Piston	1	1 3/16	3/32	120
Injector Fuel Piston #1	1/2	11/16	3/32	112
Injector Fuel Piston #2	3/8	5/8	1/8	204
Injector Teflon Insert	3/8	9/16	3/32	110

**Table B.4.** O-ring material properties.

O-ring material	Temperature Rating [°C]	Durometer Hardness	Colour
Buna-Nitrile	-37 to 121	A70	Black
Viton Fluoroelastomer	-9 to 204	A75	Brown or Black
Silicone	-53 to 218	A70	Red-orange
Teflon	-73 to 260	D55	White

#### B.4. Fan Shaft Seals

The properties and supplier of poly-amide filled Teflon are presented in this section as well as a dimensioned drawing of the fan shaft seal.

**Table B.5.** Material properties of poly-amide filled Teflon.

Property	Test Method	Value
Operating Temperature	N/A	-350 °F to 500°F
Tensile Strength	ASTM D-4745	2200 psi
Tensile Elongation	ASTM D-4745	175%
Specific Gravity	ASTM D-4745	1.83
Filler Content	N <sub>2</sub> Burn Out	N/A
Deformation	RT, 2000 psi, 24 hrs. 212°F, 2000 psi, 24 hrs.	3.5 - 4.0% 7.4%
Thermal Expansion	120 – 300°F	5.6

Supplier: Laird Plastics  
8 Plymount Street  
Winnipeg, MB R2X 2V7  
Phone: (204) 632-1136



## Appendix C - Fan Transmission Assembly

The details regarding the bearings and their lubricants as well as the specifications for the components of the fan transmission assembly are presented in this appendage.

### C.1. Bearings

The fan shafts all use the same size radial ball bearings. The specifications for the ball bearings are shown in Table C.1. The address of the supplier is also shown below.

**Table C.1.** Radial ball bearing specifications.

Part No.	R8-2RS
Inside Diameter [in]	1/2
Outside Diameter [in]	1 1/8
Height [in]	5/16

Supplier: Applied Industrial Technologies  
1495 St. James Street  
Winnipeg, MB  
R3H 0W9  
Phone: (204) 786-1167

### C.2. Lubricants

JetLube AP-5 was the lubricant used in the bearings for operation inside of high ambient temperature conditions. The properties of JetLube AP-5 are shown in Table C.2.

The corresponding supplier and manufacturer are also shown below.

**Table C.2.** Properties of Jet Lube AP-5.

Property	
Colour/Appearance	Black Smooth Grease
Base Oil	
Vis S.S.U. (@ 100°F)	975
Vis S.S.U. (@ 200°F)	70
Viscosity Index	66
Flash Point	230°C
Gravity A.P.I.	26
Pour Point	-35 °C
Solid Additives	MoS <sub>2</sub>
Grain Size	3/4 Micron
Solubility – Boiling Water	Insoluble
Dropping Point (ASTM D-566)	None
Penetration	265-295
Oxidation Stability	
P.S.I. Drop after 500 Hours	8
Shell 4-Ball Wear (ASTM D-2266)	
Scar Diameter	0.6
Shell 4-Ball Wear (ASTM D-2596)	
Weld Point, kgf	200
Load Wear Index	35
Timken EP (ASTM D-2509)	
Pass Load	11.5
Falex Seizure (ASTMD-3233)	
Seizure Load	7.57 kN (1,700 Ft.Lbs.)

Manufacturer: JET-LUBE OF CANADA LTD.  
Head Office, Warehouse & Manufacturing Facility  
3820-97 Street NW  
Edmonton, Alberta T6E 5S8  
Toll Free Phone: 1-888-771-7775  
Phone: (780) 463-7441

Supplier: Acklands-Grainger Inc.  
19 Scurfield Blvd  
Winnipeg, MB R3Y 1G4

Phone: (204) 944-3811

### **C.3. Fan Transmission Assembly Drawings**

The drawings for each component of the fan transmission assembly are shown in this section.

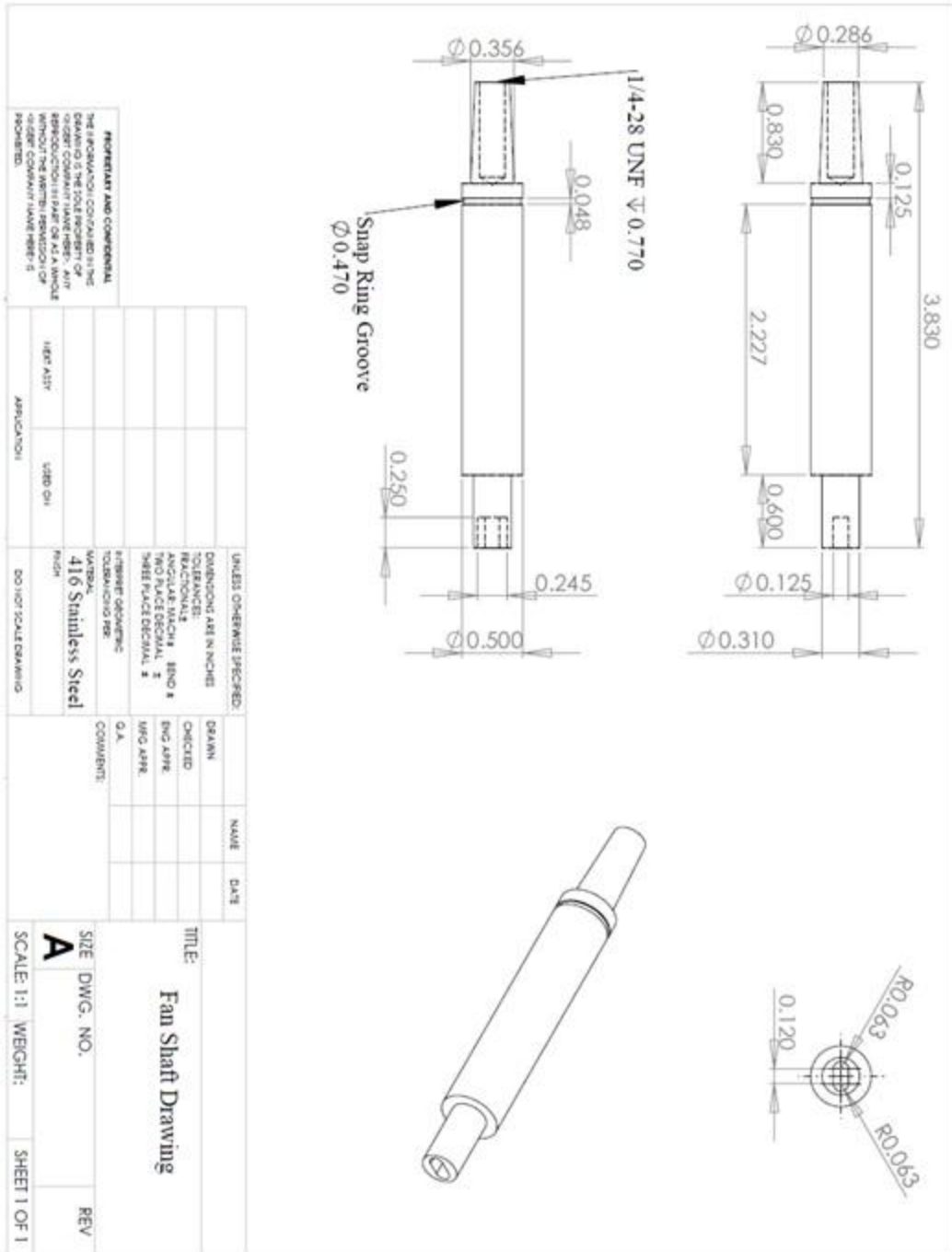


Figure C.1. Dimensioned drawing of fan shaft.

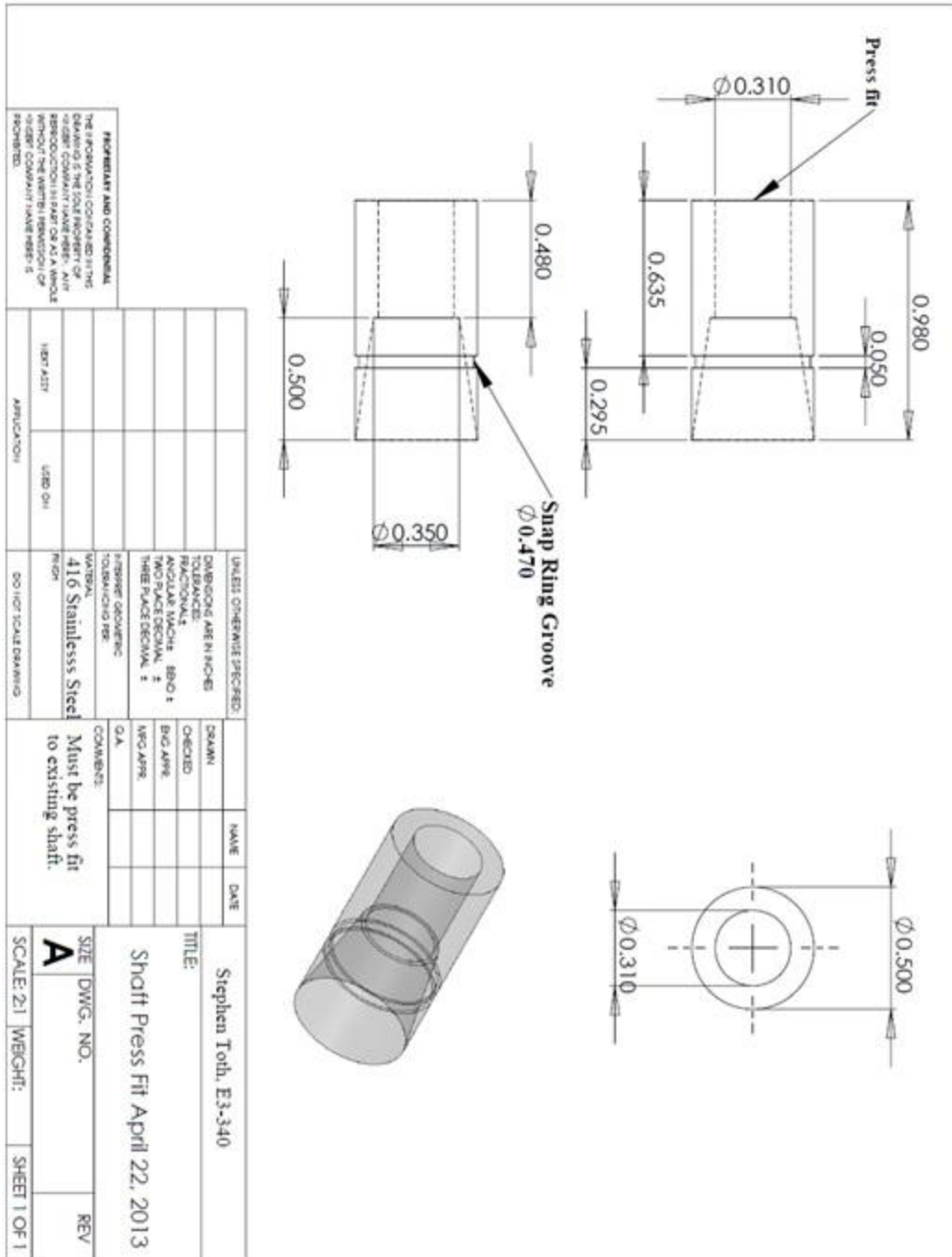
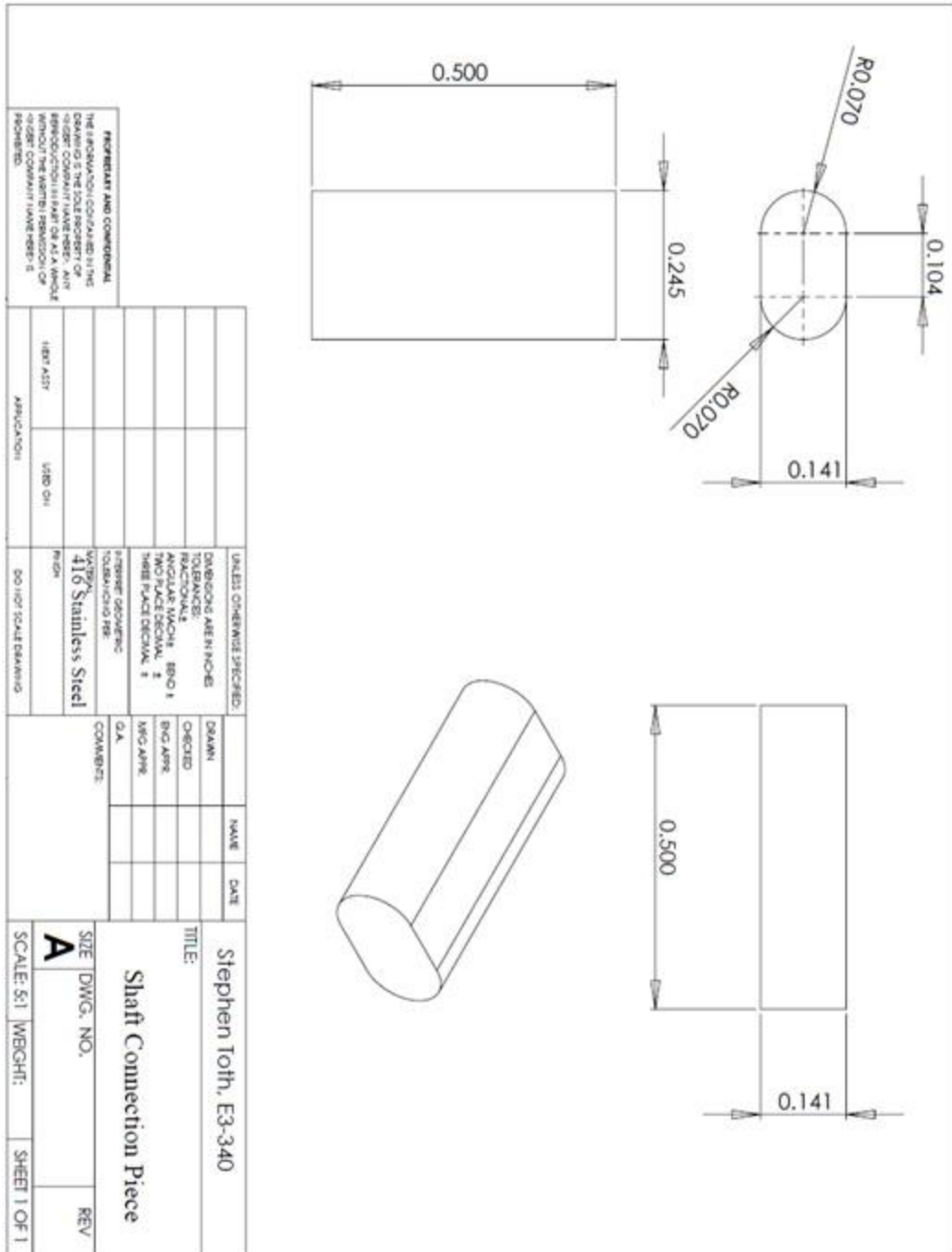


Figure C.2. Dimensioned drawing of shaft press-fit.



**Figure C.3.** Dimensioned drawing of shaft connection between fan shaft and hardened middle shaft section.

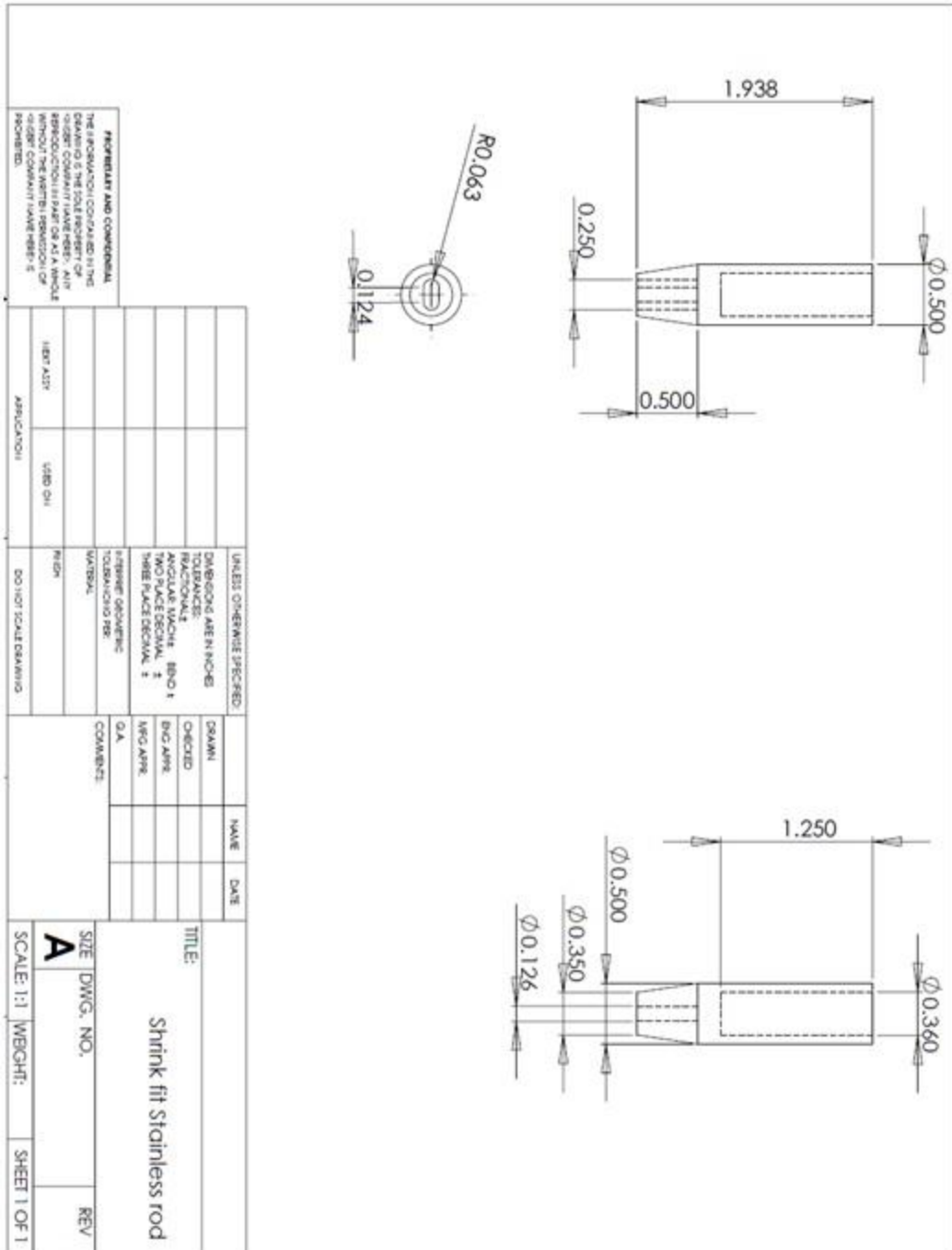


Figure C.4. Dimensioned drawing of hardened middle shaft section.



## Appendix D - Heating System

### D.1. Introduction

The heating system used to elevate the ambient temperature within the experimental apparatus is detailed in this appendage for the heating system control boxes as well as the heating system plates.

### D.2. Heating System Control Box

The heating system was controlled using components recommend by an application engineer from Omega Engineering Inc. where all of the necessary components required to create a control system are listed below in Table D.1 and were supplied by Omega Engineering Inc.

**Table D.1.** Components from Omega Engineering Inc. used for heating system control box.

Component	Model No.
Controller	CN4316-DC1-R2
Solid State Relay	SSRL240DC25
Finned Heat Sink	FHS-1
High Temp. & Conductive Paste	OT-201-1/2
Power Cord	POWER CORD-SE
K Type Thermocouple	KQXL-18G-6

The components were assembled inside of an electrical box where the width, depth and height were measured as 10 by 10 by 8 inches, respectively. The electrical box contains all of the exposed electrical connections which conform to the province of Manitoba's electrical safety code. A main power switch controls power to box where a pilot light wired after the switch acts as an indicator light. A second illuminated switch that was wired in series in between the solid state relay and the power leaving the box allows for

the box to be powered while not allowing power to exit the box. The digital controller is programmable and allows for the set point (i.e. the desired temperature) to be easily adjusted by simply pressing the arrowed up or down buttons. The controller displays two temperatures; the temperature shown with the red display is the measured value while the temperature shown by the green display is the set point. The controller reads the temperature measured by the thermocouple, if the value is below the set point, then a 5 volt signal is sent to the solid state relay to switch power on. Power travels from the electrical wall outlet, into the box, through the main switch to the solid state relay, from the solid state relay to the illuminated switch, from the illuminated switch to the heating elements.

All of the components were connected using 14 gauge electrical wires in order to handle the required amount of electrical current where the first and second heating plates require 7 and 12.5 amps of current, respectively. The combined power draw of both plates exceeded the power supply from the electrical outlets inside of the laboratory; therefore each heating plate was supplied with its own control box.

### **D.3. Heating Plates**

The heating system plates were designed to fit inside of the 5 inch viewing ports of the spherical chamber while minimizing infringement of the flow field. The required heating elements were determined through consultation with an application engineer from Omega Engineering Inc. to be tubular heating elements due to the necessity of keeping the electrical connections outside of the chamber. The heating elements were bent such that there was at least 1 inch space between the elements and the periphery of the fan blades. The heating elements were bent using the configuration found in figure 4 of [52].

The minimum spacing required between each of the elements was recommended by the same application engineer to be one inch between leading edges of adjacent elements. The circular nature of the chamber opening coupled with the minimum spacing limited the number of elements that could be accommodated inside of one viewing port to just three. The upper and lower elements required additional bending in order to fit within the chamber port opening where the elements were bent with a curvature similar to the 2.5 inch radius of the chamber opening. The individual heating elements bent according to their respective positions in the heating plate can be seen in Figure D.1 where the upper and lower elements were bent identically.



**Figure D.1.** Individual heating elements bent according to position.

The heating elements have both heated and unheated sections where the majority of the element sheath is heated except for a short length of sheath leading up to each free end. The unheated length of each element's free end can be determined by subtracting the

heated length from the sheath length and dividing by two. The each free end of a heating element is an electrical terminal. The specifications for both sizes of heating elements corresponding to the first and second heating plate are shown in Table D.2.

**Table D.2.** Properties of each heating element used for each respective heating plate.

Property	First Heating Plate	Second Heating Plate
Manufacturer	Chromalox Inc.	Chromalox Inc.
Model No.	TRI-1612 120V	TRI-17XX 120V
Power [W]	255	450
Diameter [in]	0.246	0.375
Sheath Length [in]	16	14.5
Heated Length [in]	11.5	11.5
Total Length [in]	18	16.5

The heating elements were secured inside of the heating plate using stainless steel bored through compression fittings from Swagelok. The compression fittings were designed to seal against tubing diameters of 0.250 and 0.375 inches for the first and second heating plate, respectively. The ferrules for these compression fittings were made of Teflon to minimize the possibility of damaging the sheath of the heating element while tightening the fitting. The location of the compression fittings as well as the electrical terminals are shown in Figure D.2.

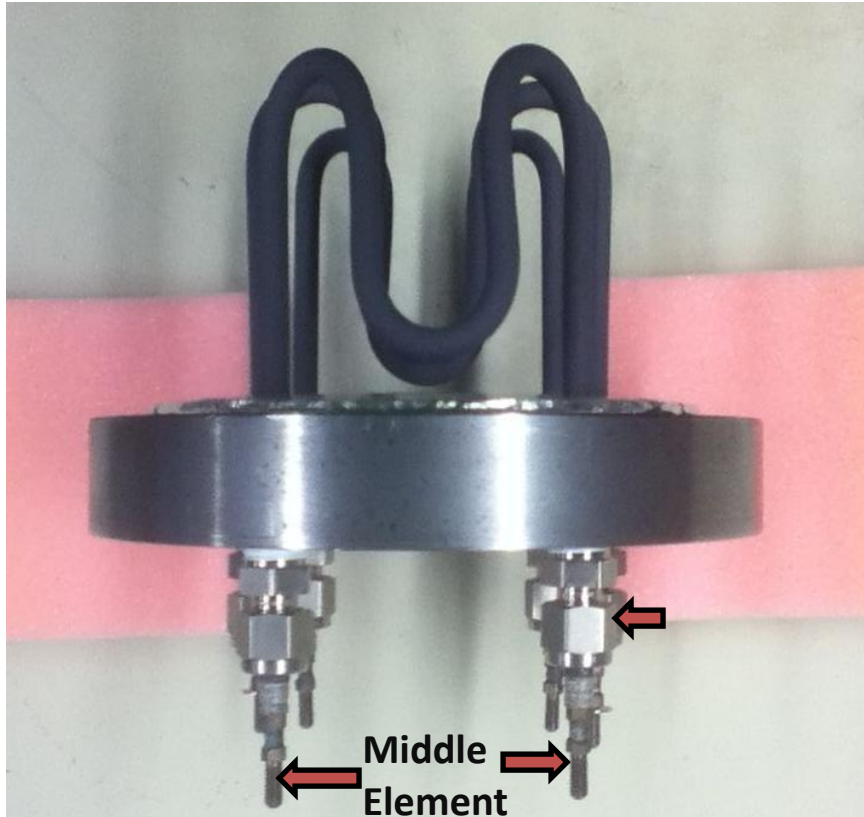


**Figure D.2.** Heating plate view from above.

#### **D.4. Heating Plate Drawings**

The drawings and schematics for the heating system plates are displayed in this section. Figure D.3 shows the dimensions as well as the locations of each heating element in the heating plate. Figure D.4 shows the dimensions of each angled heating element which can be found in the upper and lower locations of the heating element arrangement. Figure D.5 shows the dimensions for the straight heating element which corresponds to the middle of the 3 heating element arrangement. Figure D.6 shows the dimensions of the heating plate without the elements installed.

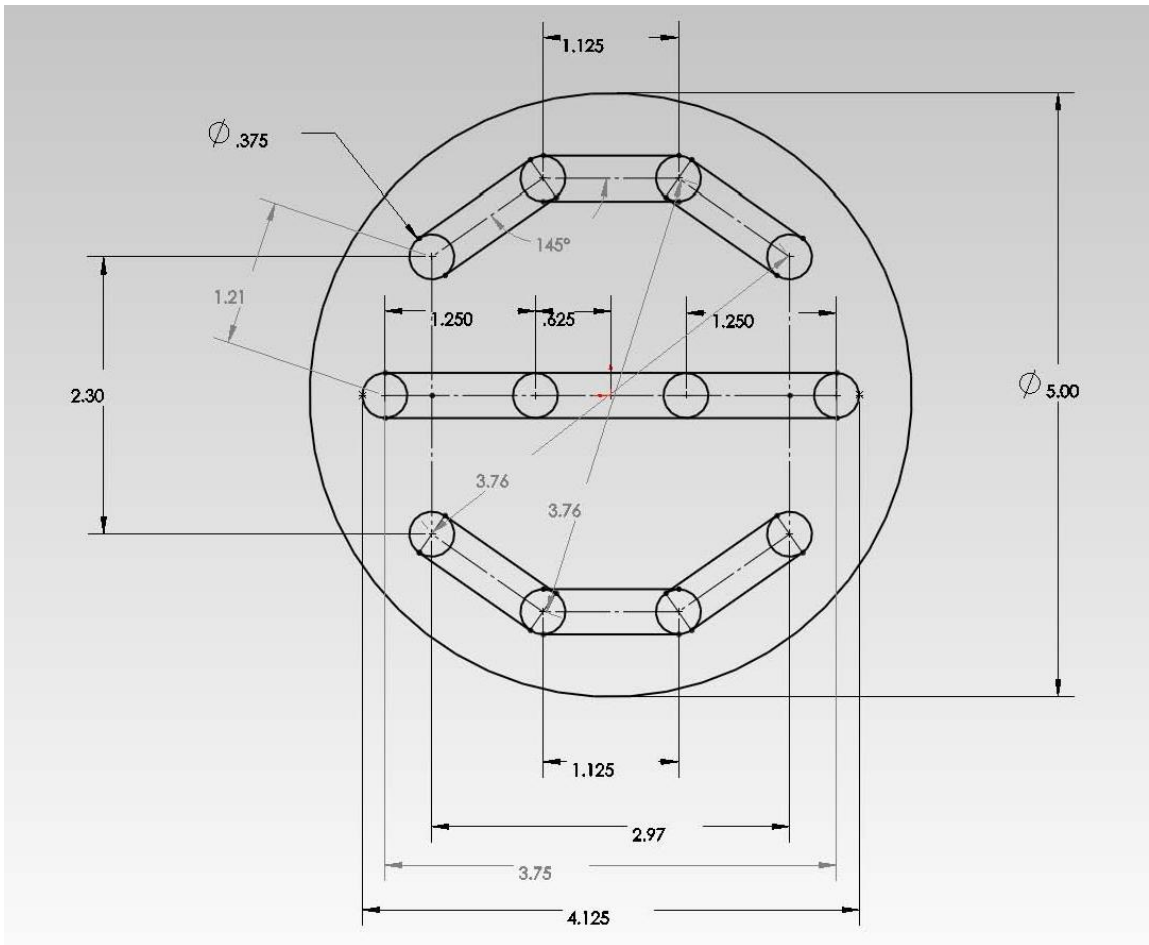


**Figure D.3.** Drawing of heating element arrangement.

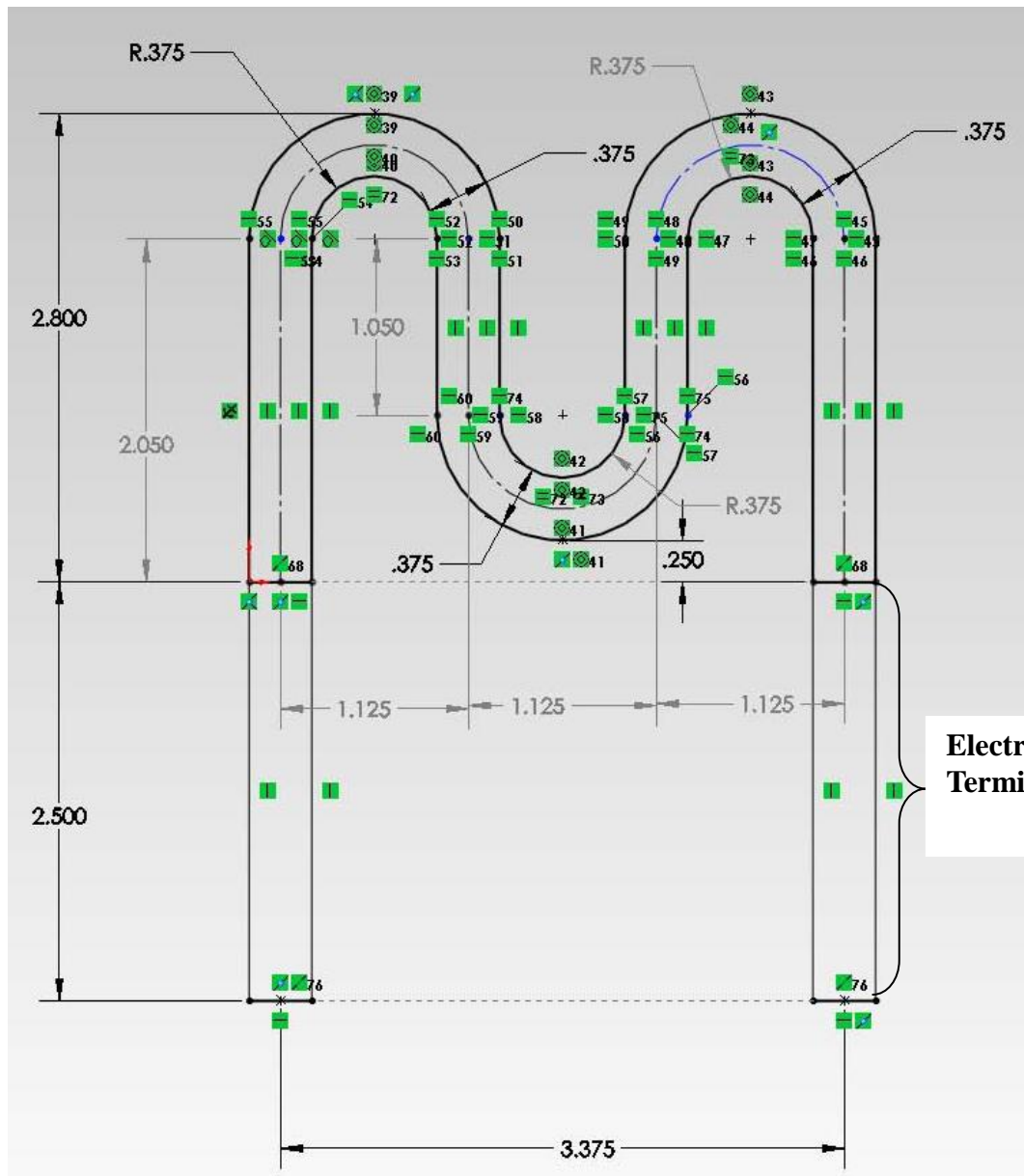


**Figure D.4.** Dimensions of angled elements (two outside elements).

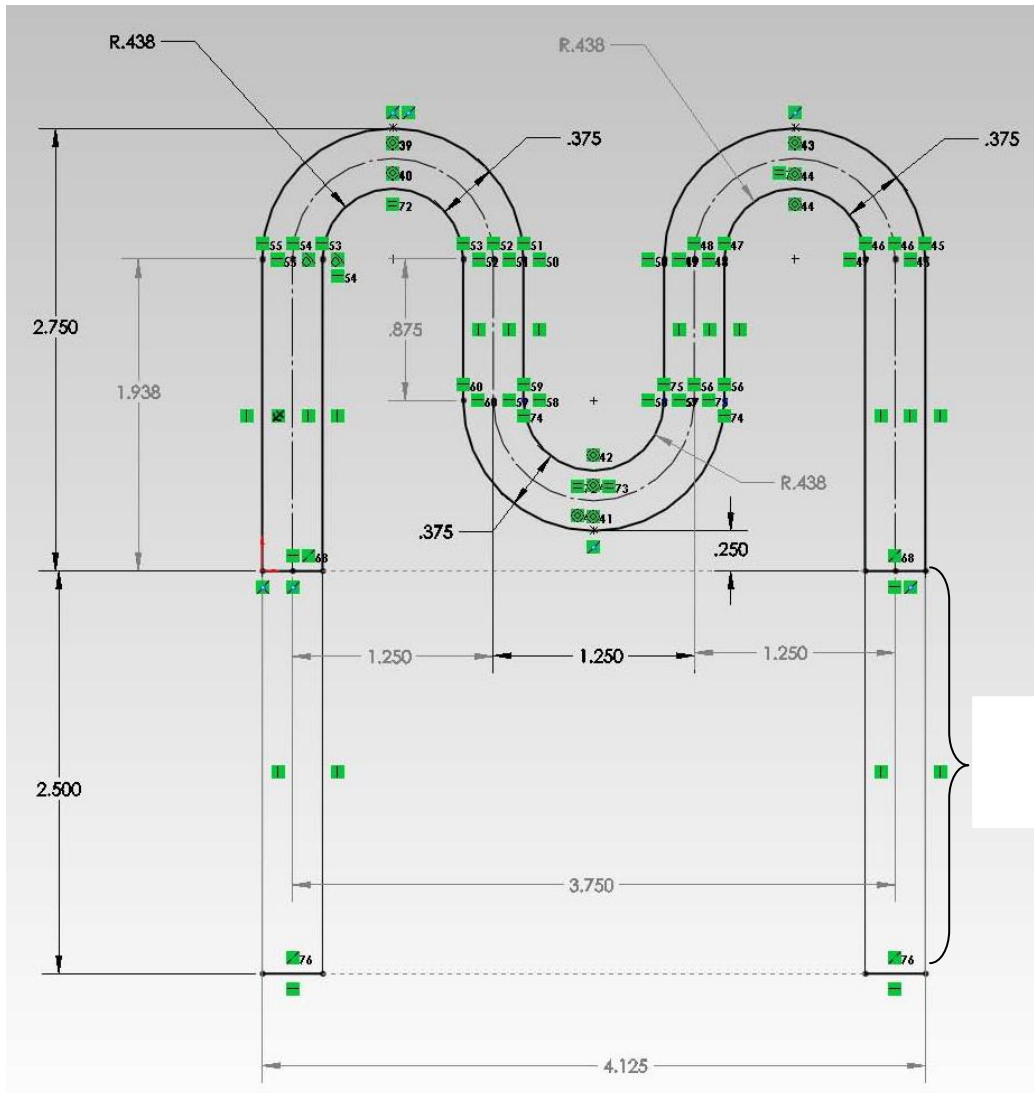


**Figure D.5.** Dimensions of straight heating element.

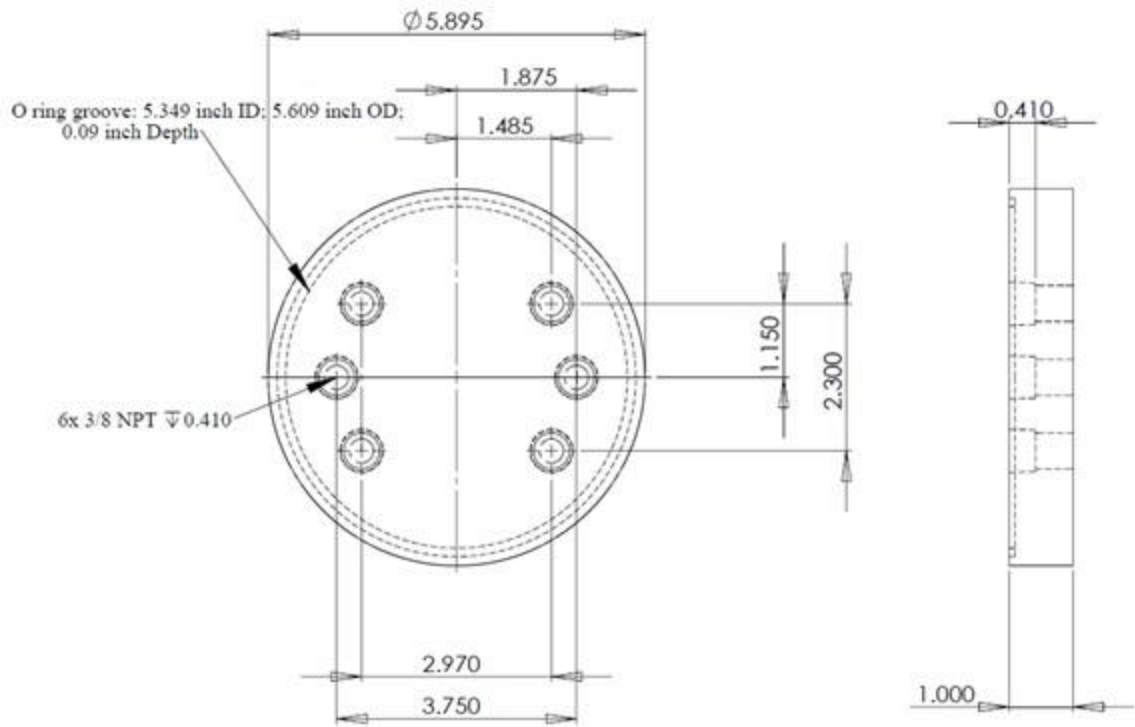


**Figure D.6.** Dimensioned drawing of heating plate.

## **Appendix E - Ignition System**

The droplet ignition system components along with their details as well as the dimensioned drawings are presented in this appendage.

### **E.1. Ignition System Components**

The following is a list of components accompanied by details for each component used to build the droplet ignition system.

- Ignition head
  - Slides over the injector needle, while holding the wire igniters as well as the heating element.
- Wire Igniters
  - Holds the heating element in place while transferring power from the electrical wires to the heating element.
- Electrical Wires
  - 18 gauge stranded wire with a Teflon-glass insulation that can withstand up to 250°C,
  - Supplier: Omega Engineering Inc., Model No.: HTTG-1CU-318S
- Transformer
  - Converts outputs voltage at  $\frac{1}{4}$  of the incoming voltage where the maximum output voltage of 30V corresponds to an input voltage of 120V.
- Variable Autotransformer
  - Input voltage: 120V
  - Adjustable voltage range: 0-140V
  - Max. Current: 7.5 Amps

- Heating Element
  - Short coiled length of 28 gauge resistance wire with a resistance of 4.11 Ohms/ft.

## E.2. Ignition System Drawings

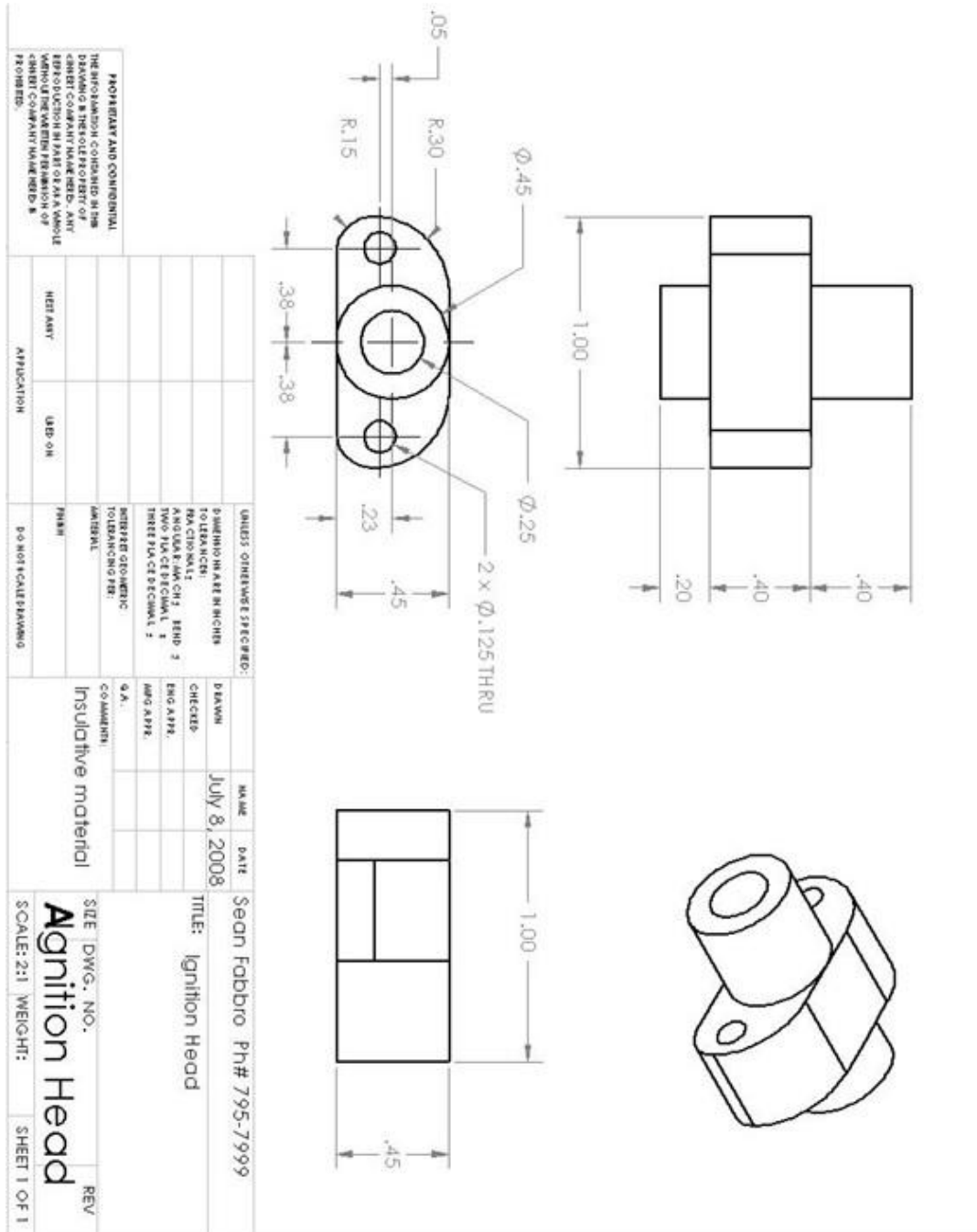
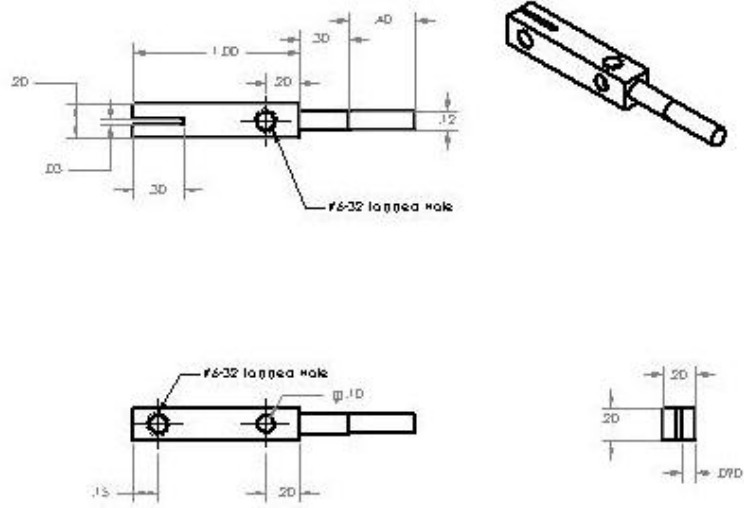


Figure E.1. Dimensioned drawing of ignition head [48].



**Figure E.2.** Dimensioned drawing of wire igniter.

## Appendix F - Matlab Code

### F.1. Introduction

An in-house developed Matlab code was used to determine the project surface area of the droplet from still images was used to determine the temporal progression of the droplet size. This code uses a method of edge detection to determine the outside edge of the droplet by using a threshold to separate dark pixels (such as the droplet and suspension fiber) from the white background as well as the noise caused by a gradual build up of particles on the viewing window. The droplet's attachment to the supporting fiber adds difficulty in determining where the droplet starts and where the fiber stops. In order to address this problem, a series of criteria were developed to distinguish between fiber and droplet is outlined below:

- The average width of the fiber must be exceeded by at least 6 pixels. This was determined by trial and error.
- The width of the fiber/droplet for one row of pixels must exceed the width of the previous row, starting from the top of the image (i.e., the fiber stem) and moving downwards one row at a time.
- The pixel value (based on a grey scale from 0-255 for an 8-bit image) of the center of the fiber/droplet as defined by the left and right edges must be less than a maximum value (i.e., *tdco* in the code) which depends on the image brightness. The maximum value should be determined by visually determining the droplet start point and measuring the highest pixel values near the center of fiber/droplet.

- The pixel located within a specified radius (i.e., defined by *contrastcontin* in the code) below the droplet start point should also have pixel values below the maximum value.

Once the droplet starting point has been found, the code examines the length of the each successive row using the detected left and right edges where the area of the droplet is determined by using trapezoidal integration between adjacent rows. After tabulating the area, the code corrects the area by using calibration sizes for the height and width of the image to determine the actual size of droplet. The droplet area is approximated as a circle where the area is divided by  $4\pi$  to give the squared diameter of the droplet before finally printing the image number as well as the squared diameter to a text file.

## F.2. Matlab Code

```
clear all;
clc;
close all;
dplot= false;

firstpic= 0;
picstep=1;
lastpic= 3000;

mst='ImgA000000'; % Use with MotionPro
% mst = 'ImgA0000'; % Use with PIV trigger
tdco=160;% Threshold for detecting start of drop, default 160
dstartmin=30;
dstartmin_Prime = 15;
fiber_approx_start = 1; %Default setting is 1
fiber_approx_finish = 50; %Depends on image
pixeldif = 6; %original value of 4; usually 6 works
contrastcontin = 6; %original value of 8
Edge_buffer = 10;
Max_contrast = 160;
Fiber_avg_correction = 2;
Threshold = 225;
%%%%%%%%%
```

```

% Change fco for each file
for fco= 1 : 1
%% % Change Next line file location to Process
FileLocation=['G:\Decane Droplet 2013\June 18\',int2str(fco)];
cd(FileLocation);
hf = fopen('test.dat','wt');
tic;
icount=0;
D2=zeros(length(firstpic:picstep:lastpic),1);
Du=zeros(length(firstpic:picstep:lastpic),1);
Dl=zeros(length(firstpic:picstep:lastpic),1);
dstart=zeros(length(firstpic:picstep:lastpic),1);
for mco=firstpic:picstep:lastpic
    fprintf('mco = %d\tfco = %d\n',mco,fco);
    sno=num2str(mco);
    strng=[mst,sno];
    strng(5:(length(strng)-10+5-1))=""; % Use with MotionPro
%     strng(5:(length(strng)-8+5-1))=""; % Use with PIV trigger
    strng=[strng,'.tif'];
%     strng = ['Fiber.tif'];
    if (exist(strng,'file')==0)
        continue;
    end
    [Img, map]= imread(strng);
    image = Img;
    icount=icount+1;
    pos = find(Img<Threshold);
    ima = zeros(size(Img));
    ima(:, :) = 255;
    ima(pos) = Img(pos);
    Img = ima;
    if dplot
        figure,imshow(image);
        figure
        imshow(Img);
        hold on
    end
    le=zeros(size(Img,1),1);
    re=zeros(size(Img,1),1);
    [row column] = size(Img);
    for i=1:1:size(Img,1)
        der=diff(double(Img(i,:)));
        if ~isempty(find(abs(der)>0,1))
            le(i)= find(abs(der)>0,1)+2;
            %Defines left edge in each row, Which was 2 pixels out.
            re(i)= find(abs(der)>0,1,'last')-1;
        end
    end
end
end

```

```

        %Defines right edge in each row, out by 1 pixel.
    end
end
names =zeros(row,column);
maxrow = zeros(row,1);
count = 1;
for j=1:1:row
    dark=find(Img(j,:)<Threshold);
    count = 1;
    for k=1:1:length(dark)-1
        change = dark(k+1)-dark(k);
        if(change == 1)
            names(j,dark(k))= count;
        elseif(change > 1)
            count = count+1;
            names(j,dark(k+1)) = count;
        end
    end
    maxrow(j) = max(names(j,:));
end
pmax = zeros(row,1);
Area = zeros(row,column);
possizematrix = zeros(row,1);
index = zeros(row,1);
r = 381;
for m= 1:1:row
    for n=1:1:maxrow(m)
        pos = find(names(m,')== n);
        possize(n) = length(pos);
    end
    possizematrix(m) = max(max(possize));
    pcheck = find(possize==max(possize));
    if(length(pcheck) > 1)
        pmax(m) = round(mean(pcheck));
    elseif(length(pcheck)==1)
        pmax(m) = pcheck;
    elseif isempty(pcheck))
        pmax(m) =1;
        disp(['Fail Safe']);
    end
    posarea = find(names(m,:) == pmax(m));
    if isempty(posarea))
        continue;
    end
    for q=posarea(1):1:posarea(end)
        Area(m,q) = 1;
    end
end

```

```

    end
end
toc
i=1;
while i<=length(le)
    if le(i)==0&&re(i)==0
        le(i)=[];
        re(i)=[];
    else
        i=i+1;
    end
end
if dplot
    for i=1:1:length(le)
        plot(le(i),i,'k');
    end

    for i=1:1:length(re)
        plot(re(i),i,'k');
    end
end
ic=1;
in=1;
ld=[];
while ic+in<=length(le)
    if abs(le(ic+in)-le(ic))<20
        if dplot
            line([le(ic) le(ic+in)],[ic (ic+in)]);
        end
        ic=ic+in;
        in=1;
    else
        %disp(['Dropping left edge point number ' int2str(ic+in)]);
        ld=[ld;ic+in];
        in=in+1;
    end
end
ic=1;
in=1;
rd=[];
while ic+in<=length(re)
    if abs(re(ic+in)-re(ic))<20
        if dplot
            line([re(ic) re(ic+in)],[ic (ic+in)]);
        end
        ic=ic+in;
    end
end

```

```

        in=1;
    else
        %disp(['Dropping right edge point number ' int2str(ic+in)]);
        rd=[rd;ic+in];
        in=in+1;
    end
end
if dplot
    line([le(end) re(end)],[length(le) length(re)]);
end
fl=length(fiber_approx_start:fiber_approx_finish);
fibre = zeros(fl,1);

%% Centerline for determining droplet start point
centermatrix = zeros(size(fibre));
for k=fiber_approx_start:1:fiber_approx_finish
    fibre(k) = re(k)-le(k)+1;
    centermatrix(k) = round(mean([re(k),le(k)]));
end
centerline = round(mean(centermatrix));
fibreavg = mean(fibre)+Fiber_avg_correction;
i=dstartmin;
notfound=true;
dstart=0;
while i<min([length(le) length(re)])&&notfound
    w = re(i)-le(i)+1;
    oldw = re(i-1)-le(i-1)+1;
    if (Img(i,round(mean([le(i) re(i)])))<=tdco)&&((re(i)-
le(i)+1)>(fibreavg+pixeldif))&&(w>oldw)&&(Img(i+contrastcontin,round(mean([le(i+c
ontrastcontin) re(i+contrastcontin)]))))<tdco)
        dstart=i;
        dstartt(icount)=dstart;
        notfound=false;
    else
        i=i+1;
    end
end
if notfound
    disp('Warning drop start not found...');
else
    if dplot
        line([le(dstart) re(dstart)],[dstart dstart]);
    end
    mv1=round(mean([le(i) re(i)]));
    if dplot
        line([mv1 mv1],[dstart max([length(le) length(re)])]);
    end
end

```

```

end
ic=dstart;
in=1;
lpc=0;
llb=0;
lub=0;
while ic+in<=length(le)
    if abs(le(ic+in)-le(ic))<20
        lpc=lpc+0.5*(2*mvl-le(ic+in)-le(ic))*in;
        llb=llb+0.5*(2*mvl-le(ic+in)-le(ic)+2)*in;
        lub=lub+0.5*(2*mvl-le(ic+in)-le(ic)-2)*in;
        if dplot
            patch([le(ic) mvl mvl le(ic+in)],[ic ic ic+in ic+in],[1 0 0]);
        end
        ic=ic+in;
        in=1;
    else
        in=in+1;
    end
end
llb=llb-(mvl-le(1)+1);
llb=llb-(mvl-le(end)+1);
lub=lub+(mvl-le(1)-1);
lub=lub+(mvl-le(end)-1);
ic=dstart;
in=1;
rpc=0;
rlb=0;
rub=0;
while ic+in<=length(re)
    if abs(re(ic+in)-re(ic))<20
        rpc=rpc+0.5*(-2*mvl+re(ic+in)+re(ic))*in;
        rlb=rlb+0.5*(-2*mvl+re(ic+in)+re(ic)-2)*in;
        rub=rub+0.5*(-2*mvl+re(ic+in)+re(ic)+2)*in;
        if dplot
            patch([re(ic) mvl mvl re(ic+in)],[ic ic ic+in ic+in],[0 1 0]);
        end
        ic=ic+in;
        in=1;
    else
        in=in+1;
    end
end
rlb=rlb-(-mvl+re(1)-1);
rlb=rlb-(-mvl+re(end)-1);
rub=rub+(-mvl+re(1)+1);

```

```

rub=rub+(-mvl+re(end)+1);
tpc=lpc+rpc;
tlb=llb+rlb;
tub=lub+rub;
xscale = size(Img,2)/2.3117;
yscale = size(Img,1)/2.3117;
sf=xscale*yscale; %Scaling Factor [pixel^2/mm^2]
Area=(tpc); %Area of the droplet pixels^2
D2(icount)=Area*(4/pi)*(1/sf);
Du(icount)=tub*(4/pi)*(1/sf);
Dl(icount)=tlb*(4/pi)*(1/sf);
Dsquared = Area*(4/pi)*(1/sf);
end
fprintf(hf,'%d\t%d\n',mco,Dsquared);
end
toc
figure
plot(D2)
hold on
plot(Du,'r')
plot(Dl,'g')
fclose(hf);
cd ..
end

```

## Appendix G - Error Analysis

The measurement uncertainty in determining the droplet size from still images using Matlab based image processing is dependent on the errors associated with magnification and image resolution. The magnification obtained through the use of magnifying lenses and a telephoto lens provided an image that is approximately 2.95 mm by 2.95 mm. Since the pixels on the camera are square and the image resolution used was 600 by 600 pixels, the corresponding pixel size was 4.92  $\mu\text{m}$  in both the horizontal and vertical directions. This gave a spatial resolution of 41311 pixels/ $\text{mm}^2$ . The high contrast ratio between the droplet and the image background makes the edge detection a function of the threshold used in image processing. An assumption of  $\pm 2$  pixels on both the left and right edges was made in Matlab to measure the maximum error for a given droplet size. Two droplet sizes were compared; one having a width of 4 pixels larger than the measured droplet size and the other having 4 pixels fewer. The maximum error for the squared diameter calculation is shown below.

$$r_{max} = \frac{1}{2} \left[ \frac{4}{\pi} \sum_{i=1}^N [(re - le + 4) - (re - le - 4)] \right]$$

Where  $r_{max}$  is the maximum error of the squared diameter,  $N$  is the number of rows of pixels that make up the droplet, whereas  $re$  and  $le$  represent the droplet edges corresponding to right and left, respectively. The summation of the difference in pixels per row between the larger and smaller droplet estimates the maximum error.

Additionally, the calculation of the maximum relative error is shown below.

$$\frac{\Delta r}{r} = \frac{r_{max}}{D^2} * 100\%$$

Where  $\Delta r/r$  is the maximum relative error (expressed as a percentage) and  $D^2$  is the squared diameter of the droplet. A sample calculation using fiber nodule (the smallest diameter possible) should show the maximum relative error of the droplet size. Assuming a perfectly circular nodule with a diameter of 500  $\mu\text{m}$  the following calculations can be made:

$$D = 500 \mu\text{m} * \left( \frac{\text{pixel}}{4.92 \mu\text{m}} \right) = 102 \text{ pixels}$$

The largest and smallest diameters correspond to 102+4 and 102- 4 pixels, respectively.

The difference in the areas and subsequently the squared diameters can be calculated by:

$$\text{Area} = \frac{\pi}{4}(D)^2$$

$$D^2 \text{ Difference} = \frac{1}{2}[(102 + 4)^2 - (102 - 4)^2] = 816 \text{ pixels}$$

$$r_{\text{max}} = D^2 \text{ Difference} = 816 \text{ pixels}$$

$$\frac{\Delta r}{r} = \frac{816 \text{ pixels}}{(102)^2} * 100\% = 7.8\%$$

The maximum relative error for the droplet size was found to be 816 pixel or approximately 7.8%.

### G.1. Diesel Example

Error analysis was conducted for diesel droplet vaporization for ambient temperature and pressure of 473 K and 16 bar, respectively as well as a fan rotational speed of 2000 RPM. Figure G.1 shows the maximum error for the droplet area as a function of time. The general trend shows that the maximum error is generally constant around a value of  $6.40 \times 10^{-3} \text{ mm}^2$  with only a handful of spikes that deviate from the trend. Figure G.2 shows the maximum relative error as a function of time where the general trend shows that as the droplet size decreases, the relative error increases. The spikes that are present in Figure G.1 show that the highest amount of error in the area calculation was approximately 5 percent.

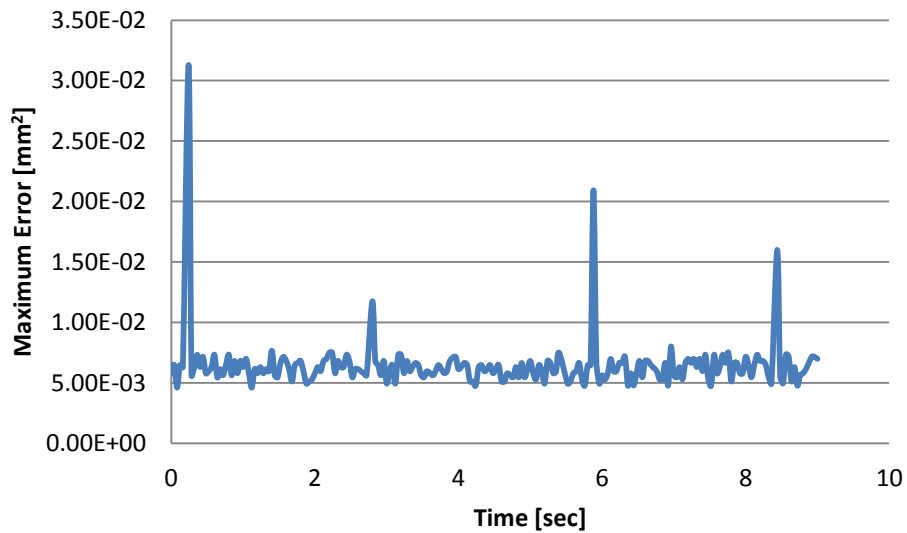


**Figure G.1.** Maximum error for diesel droplet vaporization as a function of time.

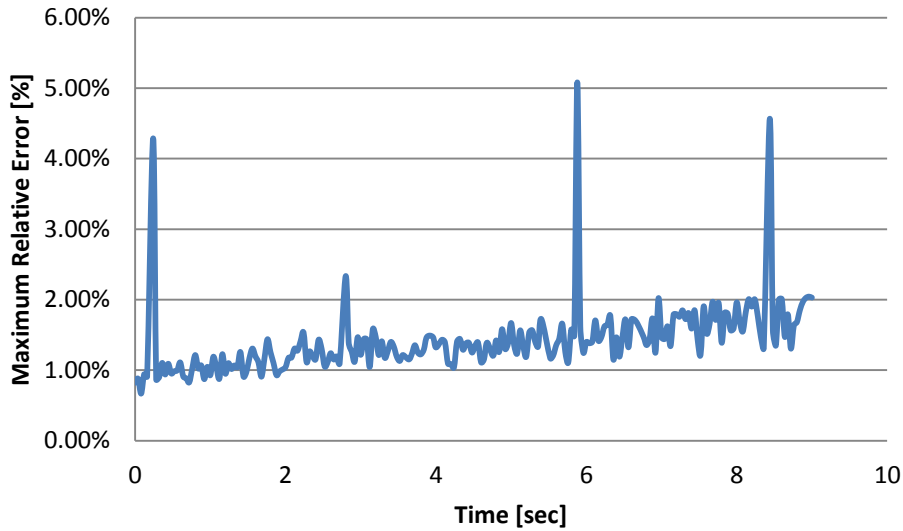


**Figure G.2.** Maximum relative error for diesel droplet vaporization as a function of time.

### **G.2. Biodiesel Example**

Similarly to the diesel example, an error analysis was conducted for biodiesel droplet vaporization under ambient temperature and pressure of 473 K and 16 bar, respectively as well as a fan rotational speed of 1500 RPM. Figure G.3 shows that the maximum error for biodiesel droplet vaporization as a function of time appears to follow a general trend where the maximum error fluctuates around an average value of  $7.08 \cdot 10^{-3} \text{ mm}^2$ . Figure G.4 shows the maximum relative error as a function of time. The relative error increases over time which indicates that the error is inversely proportional to droplet size. The maximum relative error does not exceed 2 percent for this case of biodiesel droplet vaporization.

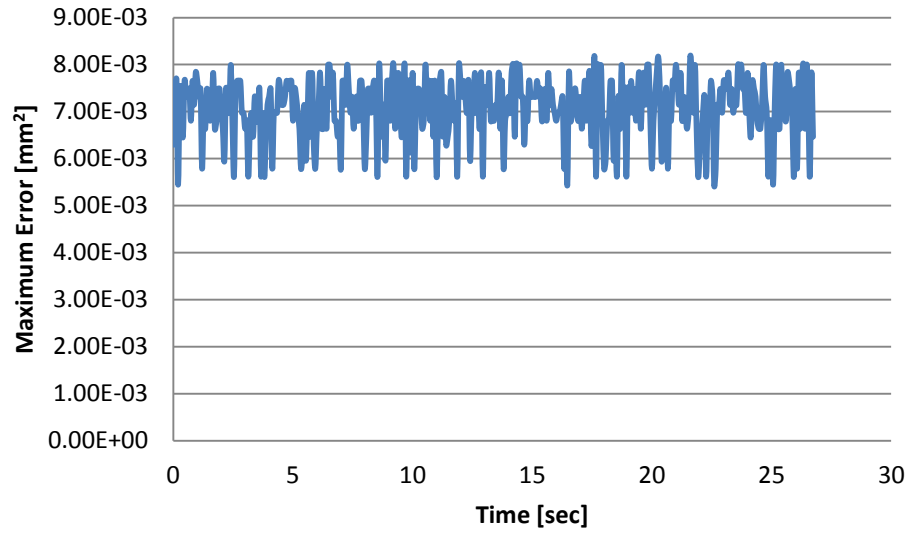


**Figure G.3.** Maximum error for biodiesel droplet vaporization as a function of time.

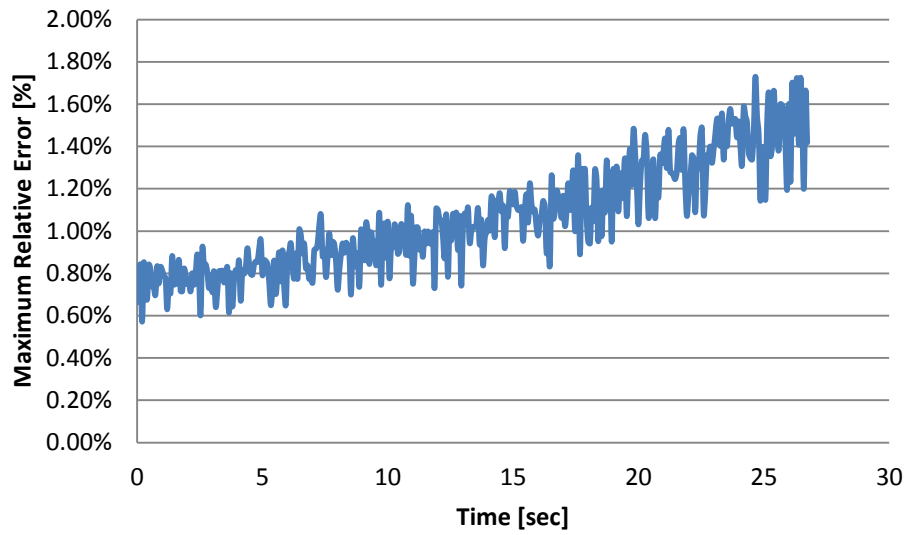


**Figure G.4.** Maximum relative error for biodiesel droplet vaporization as a function of time.